

Deep Borehole Field Test Research Activities at LBNL 2017

Spent Fuel and Waste Disposition

***Prepared for
US Department of Energy
Spent Fuel and Waste Science and
Technology***

***Patrick Dobson¹, Chin-Fu Tsang^{1,3},
Christine Doughty¹, Lasse Ahonen²,
Riikka Kietäväinen², Chris Juhlin³, Jan-
Erik Rosberg⁴, Sharon Borglin¹, Tim
Kneafsey¹, Jonny Rutqvist¹, Liange
Zheng¹, Hao Xu¹, Seiji Nakagawa¹, Kurt
Nihei¹***

***¹Lawrence Berkeley National
Laboratory, ²Geological Survey of
Finland, ³Uppsala University, ⁴Lund
University***

August 25, 2017

SFWD-SFWST-2017- 000046

National Laboratory Report No. LBNL-2001043

SFWD Working Document: External Release

DISCLAIMER

This document was prepared as an account of work sponsored by the United States Government. While this document is believed to contain correct information, neither the United States Government nor any agency thereof, nor the Regents of the University of California, nor any of their employees, makes any warranty, express or implied, or assumes any legal responsibility for the accuracy, completeness, or usefulness of any information, apparatus, product, or process disclosed, or represents that its use would not infringe privately owned rights. Reference herein to any specific commercial product, process, or service by its trade name, trademark, manufacturer, or otherwise, does not necessarily constitute or imply its endorsement, recommendation, or favoring by the United States Government or any agency thereof, or the Regents of the University of California. The views and opinions of authors expressed herein do not necessarily state or reflect those of the United States Government or any agency thereof or the Regents of the University of California.

APPENDIX E

NTRD DOCUMENT COVER SHEET 1

Name/Title of Deliverable/Milestone/Revision No. Deep Borehole Field Test Research Activities at LBNL 2017 - M3SF-17LB010306053

Work Package Title and Number Deep Borehole Field Test – LBNL SF-17LB01030605

Work Package WBS Number 1.08.01.03.06

Responsible Work Package Manager Patrick Dobson (signature on file)
(Name/Signature)

Date Submitted **08/25/2017**

Quality Rigor Level for Deliverable/Milestone ²	<input type="checkbox"/> QRL-1 <input type="checkbox"/> Nuclear Data	<input type="checkbox"/> QRL-2	<input checked="" type="checkbox"/> QRL-3	<input type="checkbox"/> QRL 4 Lab-specific
--	---	--------------------------------	---	--

This deliverable was prepared in accordance with Lawrence Berkeley National Laboratory (LBNL)
(Participant/National Laboratory Name)

QA program which meets the requirements of
 DOE Order 414.1 NQA-1 Other

This Deliverable was subjected to:

Technical Review

Technical Review (TR)

Review Documentation Provided

- Signed TR Report or,
- Signed TR Concurrence Sheet or,
- Signature of TR Reviewer(s) below

Name and Signature of Reviewers

Boris Faybishenko (Sec. 3) (signature on file)

Tim Kneafsey (Sec. 1) (signature on file)

Seiji Nakagawa (Sec. 6) (signature on file)

Kunhwi Kim (Sec. 4) (signature on file)

Patrick Dobson (Sec. 5) (signature on file)

Nicolas Spycher (Sec. 2) (signature on file)

Peer Review

Peer Review (PR)

Review Documentation Provided

- Signed PR Report or,
- Signed PR Concurrence Sheet or,
- Signature of PR Reviewer(s) below

Name and Signature of Reviewers

NOTE 1: Appendix E should be filled out and submitted with each deliverable. Or, if the PICS: NE system permits, completely enter all applicable information in the PICS: NE Deliverable Form. The requirement is to ensure that all applicable information is entered either in the PICS: NE system or by using the NTRD Document Cover Sheet.

- *In some cases there may be a milestone where an item is being fabricated, maintenance is being performed on a facility, or a document is being issued through a formal document control process where it specifically calls out a formal review of the document. In these cases, documentation (e.g., inspection report, maintenance request, work planning package documentation or the documented review of the issued document through the document control process) of the completion of the activity, along with the Document Cover Sheet, is sufficient to demonstrate achieving the milestone.*

NOTE 2: *If QRL 1, 2, or 3 is not assigned, then the QRL 4 box must be checked, and the work is understood to be performed using laboratory specific QA requirements. This includes any deliverable developed in conformance with the respective National Laboratory Participant, DOE or NNSA-approved QA Program.*

This page was intentionally left blank

SUMMARY

The goal of the U.S. Department of Energy's Spent Fuel and Waste Science and Technology's Deep Borehole Field Test was to drill two 5 km large-diameter boreholes: a characterization borehole with a bottom-hole diameter of 8.5 inches and a field test borehole with a bottom-hole diameter of 17 inches. These boreholes were to be used to demonstrate the ability to drill such holes in crystalline rocks, effectively characterize the bedrock repository system using geophysical, geochemical, and hydrological techniques, and emplace and retrieve test waste packages. These studies could be used to test the deep borehole disposal concept, which requires a hydrologically isolated environment characterized by low permeability, stable fluid density, reducing fluid chemistry conditions, and an effective borehole seal. Although U.S. Department of Energy (DOE) recently cancelled the Deep Borehole Field Test project, the research associated with this effort is still relevant to many aspects of geologic radioactive waste disposal.

During FY17, Lawrence Berkeley National Laboratory scientists conducted a number of research studies to support the Deep Borehole Field Test effort. This work included conducting analog studies using an extensive suite of geoscience data and samples from a deep (2.5 km) research borehole in Sweden, conducting laboratory experiments and coupled process modeling related to borehole seals, and developing a potential single borehole fracture imaging technique that could be applied to the characterization and monitoring of the deep borehole environment. The results of these studies are presented in this report.

This research was performed as part of the deep borehole field test (DBFT). Based on revised DOE priorities in mid-2017, the DBFT and other research related to a deep borehole disposal (DBD) option have been discontinued; current work is being closed out and documentation will be completed by the end of fiscal year (FY) 2017. Further DBFT work, for example, implementation of an engineering demonstration (SNL 2016^a), would require resumption of DBD research and development at some future time.

^a SNL (Sandia National Laboratories) 2016. *Deep Borehole Field Test Conceptual Design Report*. FCRD-UFD-2016-000070 Rev. 1. U.S. Department of Energy, Office of Used Nuclear Fuel Disposition.

This page was intentionally left blank

CONTENTS

SUMMARY v

ACRONYMS..... xvii

1. INTRODUCTION..... 1

2. FFEC LOG CONSTRAINTS ON BOREHOLE WATER VARIATIONS AND
EVALUATION OF WATER SAMPLING METHODS IN THE COSC-1 BOREHOLE,
SWEDEN 3

 2.1 Introduction..... 3

 2.2 Downhole water sampling methods 5

 2.2.1 Comparison of two water sampling methods: tube method and wireline
 sampler..... 5

 2.2.2 COSC-1 well sampling and logging runs..... 6

 2.3 Electrical Conductivity Measurements 9

 2.4 Comparison of FFEC and Downhole Water Sample Electrical Conductivity Results 12

 2.5 Acknowledgments..... 14

 2.6 References..... 14

3. SWEDISH BOREHOLE ANALOG STUDY: COMPARISON OF FIELD AND
LABORATORY FRACTURE TRANSMISSIVITY MEASUREMENTS 17

 3.1 Introduction..... 17

 3.2 Methodology..... 17

 3.2.1 Field measurement of transmissivity (FFEC) 17

 3.2.2 Description of fractures..... 18

 3.2.2.1 Depth/diameter/length..... 18

 3.2.2.2 CT scans..... 20

 3.2.3 Experimental apparatus..... 22

 3.2.4 Experimental Procedure..... 26

 3.3 Laboratory Results 26

 3.3.1 Core 188-4, depth 638 m..... 27

 3.3.2 Core 211-2, depth 702 m..... 28

 3.3.3 Core 84Z, depth 340 m 30

 3.3.4 Core 401-1, depth 1241 m..... 31

 3.3.5 Issues with damaged/worn fractures 33

 3.3.5.1 Flow around the core from poor fit/alignment of fractures..... 33

 3.4 Comparison of field and laboratory results 33

 3.4.1 Aligning cores with field measurements..... 33

 3.4.2 Depth resolution differences between cores and field 34

 3.4.3 Assessment..... 34

 3.5 Conclusions..... 35

 3.5.1 Conclusions and lessons for future work 35

 3.5.2 Further Analysis..... 35

 3.6 References..... 35

4.	SEAL MODELING.....	37
4.1	TH modeling of thermal pressurization and upflow through disturbed zone.....	37
4.1.1	Simulation setup.....	37
4.1.2	Simulation results: Thermal Response.....	39
4.1.3	Simulation results: Pressure Response and Fluid Flow	40
4.1.4	TH Modeling Conclusions	43
4.2	THC model for evaluating competitive processes that affect the migration of radionuclides	43
4.2.1	THC simulation setup	43
4.2.2	Simulation results.....	46
4.2.3	THC Modeling Conclusions	51
4.3	THM Modeling	51
4.3.1	General THM modeling approach	51
4.3.2	Estimates of in situ stress.....	53
4.3.3	Stress evolution modeling using TH modeling result	55
4.3.3.1	Approach for stress evolution modeling	55
4.3.3.2	Thermal load case and basic material parameters.....	57
4.3.3.3	Stress evolution for a base-case of $S_{Hmax} = Sv$ and $S_{Hmin} = 0.7Sv$	57
4.3.3.4	Case 1 of critically-stressed crust with $SHmax = Sv$ and $Shmin = 0.58Sv$..	61
4.3.3.5	Case 2 of critically-stressed crust with $SHmax = 1.3Sv$ and $Shmin = 0.68Sv$	65
4.3.3.6	Summary and key findings from stress evolution modeling.....	69
4.3.4	Simple stress-permeability model and its calibration for disturbed zone modeling	70
4.3.4.1	Study of macroscopic failure pattern around mine-by experiment.....	71
4.3.4.2	Study of permeability changes around the TSX tunnel	73
4.3.5	Implementation and testing of a continuum damage model for disturbed zone	75
4.3.5.1	Outline of continuum damage model.....	76
4.3.5.2	Implementation	77
4.3.5.3	Modeling and calibration of near field rock responses against field experiments at URL	78
4.3.5.4	Parametric study.....	88
4.3.6	Summary of THM modeling.....	92
4.3.7	Conclusions of seal modeling	94
4.4	References.....	94
5.	SEAL EXPERIMENTS.....	99
5.1	Introduction.....	99
5.2	Breakout Experiments Using Rectangular Sample	100
5.3	Breakout Experiments Using Shaped Cores/Slabs.....	103
5.4	Conclusion	111
5.5	References.....	111

6.	DESIGN OF SITE CHARACTERIZATION AND MONITORING EFFORTS	113
6.1	Introduction.....	113
6.2	Single well seismic imaging with a full-waveform approach	113
6.2.1	Full-waveform inversion with multi-component sources and receivers	114
6.2.2	Numerical implementation.....	114
6.3	Full-waveform single well seismic imaging of a vertical fracture with scalar and multi-component data	114
6.3.1	Case 1: Fracture imaging with pressure source and pressure receivers	115
6.3.2	Case 2: Fracture imaging with pressure source and particle velocity receivers	116
6.4	Conclusions and Next Steps.....	117
6.5	References.....	117

LIST OF FIGURES

Figure 2-1. Chloride contents vs. depth for a series of borehole waters in Finland (Blomqvist, 1990). 4

Figure 2-2. Schematic illustration of tube sampling method developed by the GTK for the COSC-1 well. On the left, the tube is lowered down to the bottom of the well and the bottom portion of the tube is sealed. The tube was lowered into the borehole slowly with the goal that the stratification of the water column chemistry would be preserved throughout the length of the tube. On the right, as the tube is raised from the hole, individual segments are crimped off, thus isolating that section of the water column. 7

Figure 2-3. Collection of tube samples in the field. Metal clamps were used to crimp the plastic tubing to separate out distinct sampling intervals. 8

Figure 2-4. Comparison of temperature-corrected electrical conductivity values using three different correction equations and a reference temperature of 25°C. The red curve was calculated using the linear correction equation and the temperature coefficient from Tsang et al. (1990), the green curve was using the linear correction equation and the temperature coefficient from Mäntynen (2001), and the blue curve represents a non-linear temperature correction equation for natural waters from the CEN (1993). The temperature data is from the baseline FFEC log. 10

Figure 2-5. Plot of measured vs. calculated electrical conductivity values corrected to the 25°C reference temperature for the tube water samples from the COSC-1 borehole. Note that all but one of the samples falls very close to the 1:1 correlation line. 11

Figure 2-6. Plot of FFEC and measured tube water electrical conductivity values, both corrected to reference temperature of 25°C using the same non-linear temperature correction equation. Also plotted are the depth interval averages of the FFEC log values that correspond to the sampled depth intervals for the tube samples, as well as the calculated EC values for the six wireline downhole water samples. Stratigraphy of COSC-1 well from Wenning et al. (2017). White sections represent undifferentiated felsic lithologies, gray zones are undifferentiated mafic lithologies, lined sections indicate gneiss with mica schists and mylonite bands, and black zones represent mylonites. 13

Figure 3-1. Aperture distribution (in mm) for the Core 211-2 fracture, which ranged from 0 to 1.83 mm when the sample did not have confining pressure applied. The dark sections represent larger voids within the fracture. 20

Figure 3-2. Aperture distribution (in mm) of Core 188-4 fracture which ranged from 1 to 1.86 mm for the unconfined fracture. 21

Figure 3-3. Top down view of Core 401-1 showing the eight flow channels located around the circumference. The flow channels were created with half-round stainless tubing, were held tightly to the rock with a silicone sleeve, and applied confining pressure. Flow was directed through the fracture from paths 1 to 5, 2 to 6, 3 to 7, and 4 to 8. 21

Figure 3-4. Cross section views of the flow paths in tested cores. Note that these scans were taken without any applied external confining pressure. The flow paths below were created by reslicing across the core image between the flow channels as shown in Figure 3-3. 22

Figure 3-5. System schematic. The lower syringe pump controls confining pressure, and the upper syringe pump flows water through the core. Two 5-way ball valves (one shown) control flow to the inlet and outlet tubes. 24

Figure 3-6. Apparatus assembly: (a) Both pieces of the fractured core are placed in between the water inlets and outlets, (b) Thin metal strips wrapped around the region containing the fracture to keep the silicone sleeve from flowing into the aperture at elevated confining pressure (used for 401-1 and 84Z cores), (c) End of core showing the Silicone rubber sleeve, (d) Schematic cutout of sleeve, (e) View with outer sleeve in place, and (f) feed-through ports on the pressure vessel cap. 25

Figure 3-7. Fracture geometries used in the analogy. 27

Figure 3-8. Transmissivity of Core188-4 fracture. The multiple points for each flow path at a given confining pressure represent different applied flow rates. Confining pressure increased monotonically during this experiment. 28

Figure 3-9a. Transmissivity of Core 211-2 fracture during increasing confining pressure. The multiple points for each flow path at a given confining pressure represent different applied flow rates. 29

Figure 3-9b. Transmissivity of Core 211-2 fracture during decreasing confining pressure. Multiple points for each flow path at a given confining pressure represent different applied flow rates. 29

Figure 3-10. Transmissivity of the Core 84-Z fracture, as confining pressure was first increased from 500 to 1200 psi, and then was decreased back to 500 psi. Transmissivity was only determined in path 4 to 8 during the initial pressurization. The multiple points for each flow path at a given confining pressure represent different applied flow rates. 30

Figure 3-11. Core 84-Z fracture transmissivity with initial higher values obtained from initial settling of the fracture removed. For the points shown, confining pressure was monotonically decreased from 1200 to 500 psi. The multiple points for each flow path at a given confining pressure represent different applied flow rates. 31

Figure 3-12. Typical transmissivity values for Core 401-1, where the first set of measurements showed tightening of the fracture with increasing confining pressure. When returning to lower confining pressure the fracture maintained a lower transmissivity. 32

Figure 3-13. Transmissivity of Core 401-1 fracture. For the points shown, confining pressure was monotonically decreased from 3000 to 750 psi. 32

Figure 3-14. Top frame: natural gamma logs from FFEC logging Test 1 with original depths. Bottom frame: same logs with depth shifted by 2 m for the second profile. Blue bars show location of FFEC peaks. 34

Figure 4-1. Spacing of multiple wellbores, showing 100 m simulated zone (wellbore to midpoint) and no-flow boundaries. 37

Figure 4-2. Configuration of the cylindrical simulated region, including wellbore, sealed well, waste disposal zone, and boundaries. 38

Figure 4-3. Temperature evolution at several distances from the waste packages at the midpoint of the waste disposal zone ($z = -4,000$ m) for 580 W (left) and 2,600 W (right) canisters. 40

Figure 4-4. Temperature evolution adjacent to the wellbore at $z = -3,000$ m, $-1,500$ m, and -500 m ($r = 0$ m) for 580 W (left) and 2,600 W (right) canisters. 40

Figure 4-5. Pressure evolution at several distances from the waste packages at the midpoint of the waste disposal zone ($z = -4,000$ m) for 580 W (left) and 2,600 W (right) canisters. 41

Figure 4-6. Pressure evolution adjacent to the wellbore at $z = -3,000$ m, $-1,500$ m, and -500 m ($r = 0$ m) for 580 W (left) and 2,600 W (right) canisters. 41

Figure 4-7. Total water flow in the disturbed rock zone adjacent to the wellbore at $z = -3,000$ m, $-1,500$ m, and -500 m ($r = 0$ m) for 580 W (left) and 2,600 W (right) canisters..... 42

Figure 4-8. Pressure evolution adjacent to the wellbore at $z = -3,000$ m, $-1,500$ m, and -500 m ($r = 0$ m) for 580 W (left) and 2,600 W (right) canisters for the base disturbed-rock permeability and for a 10X increases in permeability. 42

Figure 4-9. Total water flow in the disturbed rock zone adjacent to the wellbore at $z = -3,000$ m, $-1,500$ m, and -500 m ($r = 0$ m) for 580 W (left) and 2,600 W (right) canisters for the base disturbed-rock permeability and for a 10X increases in permeability..... 43

Figure 4-10. Salinity of pore fluid from crystalline rocks in the Canadian Shield (Frape and Fritz, 1987)..... 44

Figure 4-11. Temperature evolution at several radial distances from the waste packages at the midpoint of the waste disposal zone ($Z = -4,000$ m). 47

Figure 4-12. Pressure evolution at several radial distances from the waste packages at the midpoint of the waste disposal zone ($z = -4,000$ m) for 580 W canisters. 48

Figure 4-13. The flux (kg/year) at several radial distances from the waste packages at the midpoint of the waste disposal zone ($z = -4,000$ m). Positive value indicates that the flux is outwards from the waste packages and negative values mean the flux is inwards the waste packages..... 48

Figure 4-14. Uranium concentration at several radial distances from the waste packages at the midpoint of the waste disposal zone ($z = -4,000$ m). 49

Figure 4-15. Temperature evolution in the damaged zone (adjacent to the wellbore) at several depths..... 49

Figure 4-16. Pressure evolution in the damaged zone (adjacent to the wellbore) at several depths..... 50

Figure 4-17. Flux in the damaged zone (adjacent to the wellbore) at several depths. Upwards flux is positive..... 50

Figure 4-18. Uranium concentration in the damaged zone (adjacent to the wellbore) at several depths..... 51

Figure 4-19. Overview of THM modeling approach 52

Figure 4-20. Global compilation of (a) vertical stress and (b, c) lateral stress coefficients, k , down to a depth of 3 km in the Earth’s crust according to Brown and Hoek (1978) (adapted from Zang and Stephansson, 2010) 54

Figure 4-21. Published stress estimates at (a) Gravberg-1 deep borehole in Sweden (Lund and Zoback, 1999), and at (b) KTB borehole Germany (Brudy et al., 1997)..... 55

Figure 4-22. Evolution of (a) total stress and (b) effective stress at 4 km depth. 57

Figure 4-23. Evolution of (a) total stress and (b) effective stress at 3 km depth. 58

Figure 4-24. Evolution of (a) total stress and (b) effective stress at 1.5 km depth. 58

Figure 4-25. Effective stress paths in terms of (a) σ'_{Hmax} vs σ'_{hmin} , (b) σ'_{Hmax} vs σ'_v , and (c) σ'_v vs σ'_{hmin} at 4 km depth..... 59

Figure 4-26. Evolution of maximum and minimum (a) total and (b) effective tangential stresses around the borehole at 4 km depth. 60

Figure 4-27. Evolution of maximum and minimum (a) total and (b) effective tangential stresses around the borehole at 3 km depth. 61

Figure 4-28. Evolution of maximum and minimum (a) total and (b) effective tangential stresses around the borehole at 1.5 km depth. 61

Figure 4-29. Effective stress paths in terms of (a) σ'_{Hmax} vs σ'_{hmin} , (b) σ'_{Hmax} vs σ'_v , and (c) σ'_v vs σ'_{hmin} at 4 km depth for the case of a critically stressed crust. 62

Figure 4-30. Evolution of maximum and minimum effective tangential stresses around the borehole at (a) 4 km, (b) 3 km, and (c) 1.5 km depth. 64

Figure 4-31. Effective stress paths in terms of (a) σ'_{Hmax} vs σ'_{hmin} , (b) σ'_{Hmax} vs σ'_v , and (c) σ'_v vs σ'_{hmin} at 4 km depth for a critically stressed crust. 66

Figure 4-32. Evolution of maximum and minimum effective tangential stresses around the borehole at (a) 4 km, (b) 3 km, and (c) 1.5 km depth. 68

Figure 4-33. Evolution of maximum and minimum effective tangential stresses around the borehole at 3 km depth for the base-case stress field and with consideration of concrete plug poroelastic and thermal expansion with pressure and temperature changes. Enhanced thermal expansion is for a case of a plug having a factor of three higher thermal expansion coefficient. 70

Figure 4.34. Schematic of the failure patten and stress field associated with two underground opening at the Manitoba URL Canada (a) mine-by experiment and (b) TSX tunnel. 71

Figure 4-35. Illustration of the spalling failure criterion developed by Martin et al. (1999). 72

Figure 4-36. Comparison of the shape of the failed zone using conventional Mohr-Coulomb criterion and the alternative spalling criterion without mobilized friction. (a) Mohr-Coulomb criterion $C = 18.7$ MPa, $\phi = 49^\circ$. (b) Spalling Criterion $\sigma_c = 120$ MPa $C = 60$ MPa, $\phi = 0^\circ$ 72

Figure 4-37. Calculated contours of principal stresses (in Pa) at the Mine-by tunnel: (a) Maximum compressive principal stress and (b) minimum compressive principal stress. 73

Figure 4-38. Measured and modeled permeability for a borehole extending vertically from the top of the drift and for a borehole extending horizontally from the springline of the tunnel. Graphs of measured and modeled permeability from Souley et al., (2001). 74

Figure 4-39. Comparison of best-fit simulated and measured results of permeability changes during excavation of the TSX tunnel. Figures of the measured values to the left are taken from Souley et al. (2001). 74

Figure 4-40. Resulting final permeability versus deviatoric stress relation. 75

Figure 4-41. Calculated contours of permeability changes during excavation of the TSX tunnel. (a) Stress induced changes. (b) Stress induced + drill and blast effects. 75

Figure 4-42. The model setup for simulations. a) TSX tunnel at URL. b) Mine-by experiment. 79

Figure 4-43. The distribution of deviatoric stress $\sigma_{11} - \sigma_{33}$ around the TSX tunnel. 80

Figure 4-44. The distribution of damage profiles versus the radial distance from TSX tunnel wall. 80

Figure 4-45. The distribution of mean damage variable in the simulation domain at TSX experiment. 81

Figure 4-46. The distribution of deviatoric stress $\sigma_{11} - \sigma_{33}$ around the tunnel at Mine-by experiment. 82

Figure 4-47. The distribution of damage profiles versus the radial distance from the tunnel wall at Mine-by experiment. 82

Figure 4-48. The distribution of mean damage variable in the simulation domain at Mine-by experiment. 83

Figure 4-49. The distribution of predicted permeability versus the radial distance from the TSX tunnel wall. The field data is from Souley et al.’s work (2001). 84

Figure 4-50. The distribution of predicted permeability in the simulation domain at TSX experiment using Equation (4.24). 85

Figure 4-51. The distribution of predicted permeability variable in the simulation domain at TSX experiment using Equation (4.27). 85

Figure 4-52. The distribution of predicted permeability versus the radial distance from the tunnel wall at Mine-by experiment. 86

Figure 4-53. The distribution of predicted permeability in the simulation domain at Mine-by experiment using Equation (4.24). 87

Figure 4-54. The distribution of predicted permeability in the simulation domain at Mine-by experiment using Equation (4.27). Note: the term $\beta 4\Omega m^2$ in Equation (4.27) is changed to $\beta 4\Omega m^{2.5}$ in this case. 87

Figure 4-55. The distribution of deviatoric stress $\sigma_{11} - \sigma_{33}$ around the TSX tunnel. 88

Figure 4-56. The distribution of damage profiles versus the radial distance from TSX tunnel wall. 89

Figure 4-57. The distribution of mean damage variable in the simulation domain at TSX experiment. 90

Figure 4-58. The distribution of predicted permeability versus the radial distance from the TSX tunnel wall. The field data is from Souley et al.’s work (2001). 91

Figure 4-59. The distribution of predicted permeability in the simulation domain at TSX experiment using Equation (4.24). 92

Figure 4-60. The distribution of predicted permeability variable in the simulation domain at TSX experiment using Equation (4.27). 92

Figure 4-61. 3D TOUGH-FLAC model mesh of the deep borehole disposal for more detailed THM analysis. 94

Figure 5-1. Drilling-induced damage around a waste disposal well, which can result in undesirable fluid leakage pathways along the well. 99

Figure 5-2. Triaxial loading tests on a rectangular slab of novaculite containing an analogue borehole. Acoustic emissions were monitored concurrently with the loading tests. 100

Figure 5-3. Rectangular slab samples (Slab “B”, “C”, and “D”) used for the experiments. 101

Figure 5-4. Loading and acoustic emission histories during true-triaxial loading tests on novaculite slab samples containing an analogue borehole. 102

Figure 5-5. Post-experiment examination of the samples at the locations where borehole breakout was expected. The diameter of the borehole is 9.5 mm. No significant damage was

observed in spite of increased acoustic emission activity and extremely high stress along the borehole wall. 103

Figure 5-6. Shaped core samples of Stripa Granite. From the left, sample #1 through #6. 104

Figure 5-7. Axial stresses computed for the shaped cores in Figure 5-6. Unit axial stress is applied at the top of the sample. Blue regions adjacent to the curved surfaces of the models indicate where the maximum compressive (shown in negative values) stress concentration occurs. 105

Figure 5-8. Laboratory setup for the shaped-core uniaxial compression experiments using Stripa Granite cores. 106

Figure 5-9. Measured axial stress vs deformation curves (left) and axial stress time history (right) for three of the shaped Stripa Granite cores. 106

Figure 5-10. Measured acoustic emissions during the loading tests. The red arrows indicate an onset of increased AE activity. 107

Figure 5-11. Photographs of the cores after the compression experiments. Borehole-breakout like damage can be seen along the curved surface of the cores. 108

Figure 5-12. X-ray CT images of the Stripa cores after the compression experiments. For Core 1, breakout and fractures near the curved surface of the core can be seen clearly. 108

Figure 5-13. Preparation of shaped-slab sample for a large-diameter borehole breakout experiment. 109

Figure 5-14. Distributions of stresses induced in a shaped slab sample resulting from an application of compression stress at the top. 110

Figure 5-15. Comparisons between stresses along the minimum horizontal stress line (along the bottom of the model shown in Figure 5-14) of the shaped slab sample and a borehole within an infinite medium with a far-field compressional maximum stresses ratio of $(\sigma_{xx}^{\infty}, \sigma_{yy}^{\infty}) = (100 \text{ MPa}, 200 \text{ MPa})$. Note that, along the centerline, $\sigma_{xx} = \sigma_{rr}$ and $\sigma_{yy} = \sigma_{\theta\theta}$ 110

Figure 6-1. Case 1 - Single well elastic full-waveform fracture imaging with 3 pressure sources and 50 pressure receivers. Images of P-wave elastic modulus c_{33} in the x-z plane (a), and x-y plane (b) show reduction in the modulus from the background. Because pressure receivers have omni-directional sensitivity, the imaged fracture appears as a vertical cylinder with a radius equal to the well-fracture plane spacing that has been truncated by the absorbing boundaries of the numerical model. Near-source imaging artifacts are also clearly present. 116

Figure 6-2. Case 2 - Single well elastic full-waveform fracture imaging with 3 pressure sources and 50 particle velocity receivers. Image of P-wave elastic modulus c_{33} in: (a) x-z plane, and (b) x-y plane. Directional particle velocity receivers provide azimuthal better focusing of fracture image and less imaging artifacts than pressure receivers. 117

LIST OF TABLES

Table 3-1. Description of cores. Color code: Green - laboratory experiments completed, yellow - future lab experiments may be possible, red – condition of core precludes doing laboratory experiments.	18
Table 3-2. Core pictures.....	19
Table 4-1. Simulated rock properties (from Brady et al., 2009).....	39
Table 4-2. Mineral volume fraction (dimensionless, ratio of the volume for a mineral to the total volume of medium) of sedimentary rock and granite.....	45
Table 4-3. Pore-water composition (mol/kg water, except pH) for sedimentary rock and granite.....	45
Table 4-4. Aqueous complexes for UO_2^{+2}	46
Table 4-5. Parameters in DSID model for TSX and Mine-by experiments.....	79
Table 4-6. Parameters in DSID model for TSX experiment.....	88

ACRONYMS

AE	acoustic emission
COSC	Collisional Orogeny in the Scandinavian Caledonides
DBD	deep borehole disposal
DBFT	deep borehole field test
DOE	U.S. Department of Energy
DSID	deviatoric stress induced damage
EC	electrical conductivity
EDZ	excavation disturbed zone
FFEC	flowing fluid electric conductivity
GTK	Geological Survey of Finland
HMC	hydrological-mechanical-chemical
ID	inner diameter
JIT	just-in-time
LBNL	Lawrence Berkeley National Laboratory
NLCG	nonlinear conjugate gradient
NPT	national pipe thread
PWR	pressurized-water reactor
RTM	reverse time migration
TH	thermal-hydrological
THC	thermal-hydrological-chemical
THM	thermal-hydrological-mechanical
TTI	tilted-transverse isotropy

This page is intentionally left blank.

DEEP BOREHOLE FIELD TEST RESEARCH ACTIVITIES AT LBNL 2017

1. INTRODUCTION

Lawrence Berkeley National Laboratory's research contributions to the deep borehole field test project consist of a broad scope of activities. **Sections 2 and 3** of the report describe our work with members of the science team of the "Collisional Orogeny in the Scandinavian Caledonides" (COSC) project, which drilled and characterized a 2.5 km scientific borehole (COSC-1) in central Sweden, to obtain key insights on deep borehole characterization techniques. **Section 2** compares the electrical conductivity profile of the water column of the well determined using a static baseline electrical conductivity log with electrical conductivity measurements of water samples that were collected using a wireline sampler and a continuous tube method. This comparison demonstrated that the upper 1.5 km of the tube sample has not preserved the fluid stratigraphy, probably due to mixing within the sampling tube. However, there is good agreement between the fluid salinities vs. depth for the electrical conductivity log and the wireline downhole water samples.

Section 3 describes laboratory measurements of transmissivity of fractured core samples as a function of controlled stress. These fractured core samples are spatially correlated with fluid flow zones in the COSC-1 well that were identified by flowing fluid electrical conductivity (FFEC) logs. This work also evaluated the effect of scale between the transmissivity measurements on individual core samples in the laboratory and those obtained for the corresponding field-scale fractures. The laboratory study also included using a unique apparatus to measure multi-directional transmissivity to assess fracture anisotropy.

Section 4 summarizes the FY17 modeling results associated with borehole seals. This work includes thermal-hydrological (TH), thermal-hydrological-chemical (THC) and thermal-hydrological-mechanical (THM) model simulations based on the deep borehole disposal reference design that consists of a vertical, telescoping borehole design with a 43 cm (17 in) diameter borehole in the waste disposal zone from 3,000 m to 5,000 m depth. The TH modeling evaluated the effects of thermal, pressure, and fluid flow on seal performance. The THC simulations evaluated the migration of radionuclides in the damage zone resulting from changes in temperature, pressure, fluid flow, and water-rock interaction over time. THM simulations were conducted using a variety of different scenarios to evaluate the stress evolution of the system, and suggest that the potential for stress-induced damage of the borehole wall (borehole breakout and disturbed zone) is a key issue in deep borehole disposal. This work on seal modeling was conducted for deep borehole disposal applications, but is also directly applicable to other storage concepts in terms of processes and associated model developments.

Section 5 presents the results of laboratory borehole breakout experiments. An initial set of experiments using rectangular pieces of novaculite did not result in generating breakouts, so a second set of experiments were conducted using shaped cores of Stripa granite. These experiments did generate breakout structures, and acoustic emissions measurements conducted during loading appear to indicate the formation of microfractures in the deformed rock samples. Additional experiments are planned using shaped slab samples of Westerly granite.

Section 6 describes the development of a full-waveform single well seismic approach for imaging and characterizing large-scale faults and fractured zones in basement crystalline rock. A two-step approach was used: the first step uses one iteration of full-waveform inversion as an elastic reverse time migration to form a spatial image of the fractures that is used to estimate fracture orientation (azimuth and dip), and the second step performs full-waveform inversion to recover the fracture properties.

This research was performed as part of the deep borehole field test (DBFT). Based on revised DOE priorities in mid-2017, the DBFT and other research related to a deep borehole disposal (DBD) option have been discontinued; current work is being closed out and documentation will be completed by the end of fiscal year (FY) 2017. Further DBFT work, for example, implementation of an engineering demonstration (SNL 2016^b), would require resumption of DBD research and development at some future time.

^b SNL (Sandia National Laboratories) 2016. *Deep Borehole Field Test Conceptual Design Report*. FCRD-UFD-2016-000070 Rev. 1. U.S. Department of Energy, Office of Used Nuclear Fuel Disposition.

2. FFEC LOG CONSTRAINTS ON BOREHOLE WATER VARIATIONS AND EVALUATION OF WATER SAMPLING METHODS IN THE COSC-1 BOREHOLE, SWEDEN

2.1 Introduction

The COSC-1 borehole was drilled as part of the Collisional Orogeny in the Scandinavian Caledonides (COSC) scientific deep drilling project in central Sweden (Lorenz et al., 2015). The well was drilled through the Seve Nappe, which contains high-grade metamorphic rocks indicative of deep (100 km) crustal levels. The main lithologies encountered consist of felsic, amphibolite, and calc-silicate gneisses, amphibolite, migmatites, garnet mica schists, with discrete zones of mylonite and microkarst. The primary objectives of this project were to gain insights into the tectonic evolution of the area, calibrate high quality surface geophysics through deep drilling, characterize present and past deep fluid circulation patterns, determine current heat flow to constrain climate modeling, and characterize the deep biosphere (e.g., Lorenz et al., 2015; Hedin et al., 2016; Wenning et al., 2017). Our deep borehole disposal research team at LBNL has been collaborating with the COSC project to use information from this deep borehole research study as an analog for the deep borehole environment. Our team has previously used flowing fluid electrical conductivity (FFEC) logging as a means of identifying hydrologically transmissive fractures in the deep borehole (e.g., Tsang et al., 2016; Doughty et al., 2017). This particular aspect of the collaborative study involves the evaluation and interpretation of deep borehole water sampling in the COSC-1 well.

The compositions of water in deep crystalline rocks have been characterized in a number of deep borehole environments (e.g., Fritz and Frape, 1982; Frape et al., 1984, 2004; Nurmi et al., 1988; Lahermo and Blomqvist, 1988; Ruskeeniemi et al., 1996; Ahonen et al., 2011; Kietäväinen et al., 2013; Kietäväinen, 2017). Often, waters found in the shallower (upper 500 m) portions of these boreholes are quite dilute, reflecting influx of meteoric fluids. However, at deeper levels, the waters sampled from deep boreholes in crystalline basement often are more saline. These saline fluids have a number of postulated origins, such as water-rock interaction, presence of residual metamorphic, hydrothermal, or magmatic fluids, or incursion of seawater or sedimentary basin brines (e.g., Nurmi et al., 1988; Gascoyne, 2004; Frape et al., 2004; Kietäväinen et al., 2013; Kietäväinen, 2017). Examples of these types of water profile are depicted in Figure 2-1.

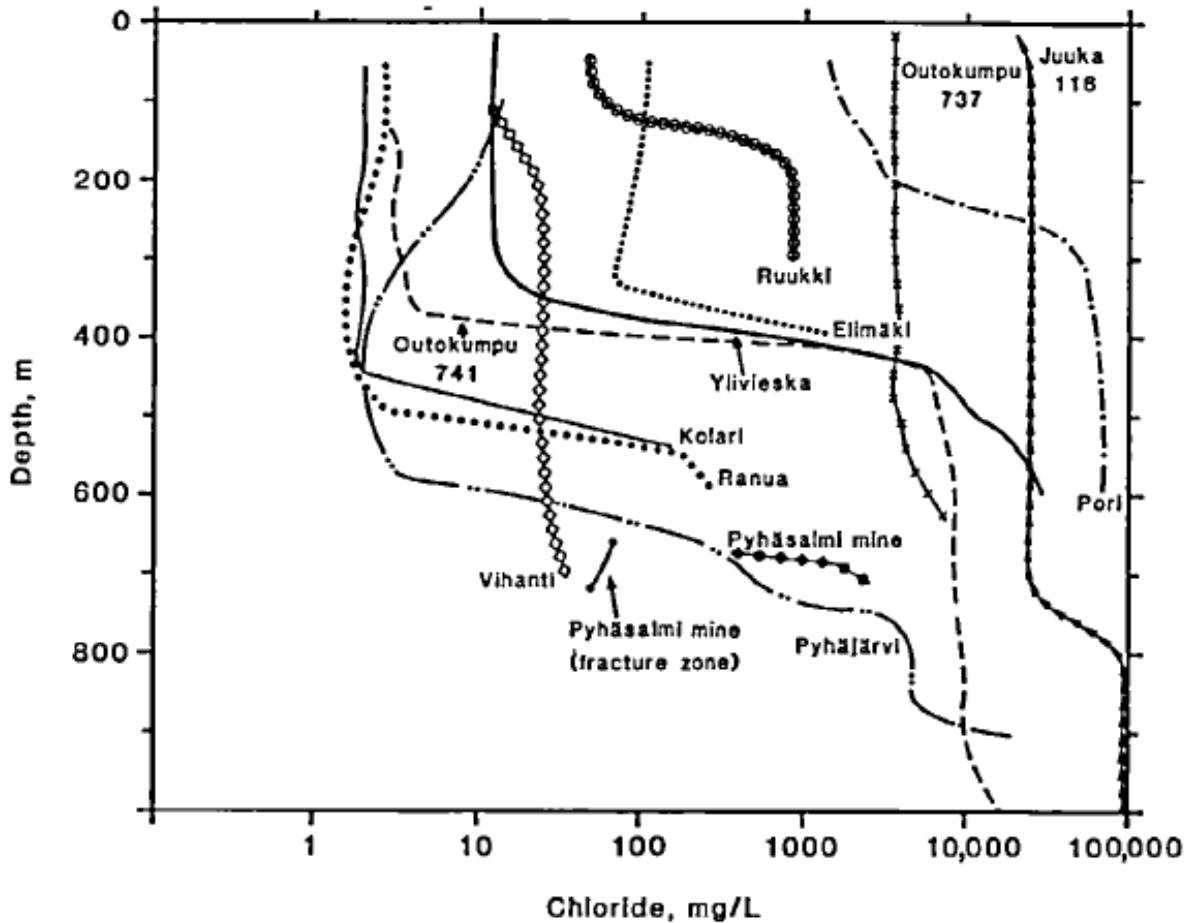


Figure 2-1. Chloride contents vs. depth for a series of borehole waters in Finland (Blomqvist, 1990).

Disposal of high-level radioactive wastes in deep borehole environments has been proposed by a number of studies (e.g., Juhlin and Sandstedt, 1989; Blomqvist, 1990; Hansen et al., 2011; Freeze et al., 2015). Favorable features for long-term geologic disposal in this manner include hydrologically isolated zones in very low permeability bedrock. These deep boreholes often have saline waters in their deeper sections that have been interpreted to represent fluids that have long residence times and are hydrologically isolated from shallow freshwater aquifers. These environments are also reducing in nature, which limits the solubility and enhances the sorption of many radionuclides. Thus, it is important to characterize the water chemistry in these boreholes to verify that the deep waters are chemically distinct and hydrologically isolated from shallower groundwater. Careful hydrologic and geochemical characterization is needed to ensure that a deep borehole can provide a safe and permanent means for disposal of high-level radioactive waste.

One challenge is obtaining representative water samples from deep boreholes that would provide insights into the local hydrology and water-rock interaction. The water that is sampled in a borehole is often a mixed fluid that has been impacted by drilling fluids and mixing of waters between different inflow zones. Thus, it is important to know the drilling history, any subsequent tests that have been run in the well, and the general hydrology of the well to develop a constrained interpretation of the water chemistry. In addition, deep waters are under significant hydrostatic pressure – this pressure is released when samples are brought to the surface, which leads to an exsolution of dissolved gases that can affect the chemistry of the solution. The method(s) used for water sampling can therefore affect the results. In this study, we used a baseline FFEC log that was run under static conditions to document in situ variations in water salinity in the COSC-

1 borehole, and two distinct downhole water-sampling methods to evaluate in situ water chemistry, as described below.

2.2 Downhole water sampling methods

A variety of downhole sampling methods have been developed to obtain representative water samples at different depths in a borehole. A common technique is the wireline downhole sampler. This method uses a sampling chamber with motor-actuated valves at the top and base. While the tool is lowered into the borehole, the valves are held open, allowing well fluid to flow freely through the chamber. At the selected sampling depth, the motor is activated under surface control, closing the valves to seal the contents of chamber, and the sampler is raised with the wireline to the surface. To sample multiple zones, the sampler must be lowered back down the well – this method can be quite time consuming to collect a suite of downhole samples.

A method that has been developed for collecting a more complete suite of samples is the tube sampling method (Nurmi and Kukkonen, 1986). This method uses a long plastic tube on a spool that is fed down to the bottom of the borehole. The premise is that the water column will be relatively undisturbed and that the water contained inside the tube will reflect the water column stratigraphy. This requires that the water flows up into the tube as it is lowered into the well in a laminar fashion. Once the tube has reached the bottom, a check valve on the bottom of the tube is closed, and the tube is progressively raised from the hole. Typically, valves are used to isolate each sampling interval, but in the case of the COSC-1 sampling effort, metal clamps were used to isolate distinct intervals of the tube as the tube was raised to the surface, thus providing a continuous sampling of the entire well.

Another method that is also employed is the use of a downhole pressurized water sampling system. This consists of inflatable rubber packers, a membrane pump, a pressure valve and pressurized sampling vessels. The packers are used to physically isolate a specific zone of the borehole (such as a fracture inflow zone), and the pump is used to fill up the sample vessels (e.g., Nyysönen et al., 2012; Kietäväinen, 2017).

A related method to the packer system described above that has been used to collect representative water and gas samples from depth is the U-tube sampler (Freifeld et al., 2005; Freifeld, 2009). This method involves using a positive fluid displacement pump – the unit has a loop of tubing (the U-tube) that is linked to a downhole packer and sampling assembly that is controlled by a ball check valve. To collect a sample from a specific interval, the packer system is emplaced, the U-tube is vented to atmosphere so that it can fill up with fluid from the underlying zone in the borehole, the check valve is closed, and then an inert gas is used to push the sampled fluid through the U-tube up to the surface. To retain dissolved gases in solution, a complex surface sampling system was developed.

2.2.1 Comparison of two water sampling methods: tube method and wireline sampler

The COSC-1 well provides an ideal test bed for comparing and contrasting water chemistry samples collected using the tube method and the conventional wireline water sampling method. In addition, electrical conductivity data obtained by the FFEC logging tool can provide independent information relating to the variations in water chemistry with depth in a borehole. When this tool is run without pumping (i.e., not in flowing fluid mode), it captures the variations in water salinity in the static water column. Thus, it can be used to provide a continuous measure of electrical conductivity values in a borehole that can be later compared with the electrical conductivity values obtained from downhole water samples from corresponding depths.

The COSC-1 borehole has a number of additional features that make it ideal for this type of comparison.

1. The borehole was drilled using a coring rig, which requires lower volumes of drilling fluid (i.e., water plus drilling additives) than a hole that is drilled with a tri-cone bit. This would result in less contamination of the borehole with external fluids.
2. The drilling water used was from a local stream with very low salinity – thus this water would only serve to dilute any subsurface fluids.
3. The borehole was only cased for the upper 100 m and has no liner, providing maximum contact between the borehole fluids and the surrounding rocks.
4. The borehole was left undisturbed for a year after the well was completed prior to the water sampling operations. This would allow the well to begin to equilibrate with the surrounding rocks, with a recovery of temperature conditions and fluids from hydraulically active fractures to mix with borehole water and establish a wellbore water stratigraphy that was reflective of different hydrologic zones at depth.
5. Two different water-sampling methods were utilized – the tube sampling method (for the entire borehole) and the wireline downhole sampler (for six selected depths). This permits a direct comparison of the two methods.
6. Operational conditions resulted in the borehole not being flushed with fresh water prior to running the FFEC baseline log. This resulted in the baseline FFEC log (where there was no surface pumping) reflecting the actual undisturbed water chemistry variations in the borehole.

2.2.2 COSC-1 well sampling and logging runs

The COSC-1 well was drilled over a period of four months to a depth of 2495.8 m, and was completed in August of 2014 (Lorenz et al., 2015). The well design consists of dual casing emplaced down to a depth of 103 m, with the inner casing having an ID of 101.6 mm, HQ core drilling down to a depth of 1616 m, and NQ core drilling was conducted from 1616 m down to TD at 2495.8 m. Fresh water was used for the first stage of drilling down to 500 m, and a series of polymers were added to the water for deeper stages to reduce friction and assist with removal of cuttings.

In September of 2015, the well was then revisited for a series of measurements and sampling activities, allowing ample time for the well bore fluids to equilibrate with the surrounding host rock and mix with inflowing fluids from surrounding aquifers. These measurements included temperature logs, static and flowing fluid electrical conductivity logs, and two of the distinct methods of water sampling described earlier (tube sampling and conventional wireline downhole fluid sampler).

An initial static FFEC log was run (along with a temperature log) to provide a baseline indication of water chemistry (via electrical conductivity) variations down to 2000 m – the temperature data provided a means to correct the EC values to a fixed temperature. The EC data provides an in situ method to measure variations in fluid salinity (via changes in electrical conductivity) along the length of the borehole that can subsequently be compared with water samples collected at different depths.

Following the EC baseline measurement, a tube sampler was installed over the entire length of the borehole to provide the opportunity to collect water samples at discrete intervals (Figure 2-2). The tubing was lowered slowly into the borehole to allow water rise in a laminar way into the tube, with the objective of minimizing mixing of the water column. After the tube was emplaced to TD, the bottom of the tube was sealed, and then the tubing was withdrawn from the borehole, with selected intervals physically isolated from each other by applying metal clamps to crimp the tubing (Figure 2-3). This sampling method is slightly modified from that described by Nurmi and Kukkonen (1986).

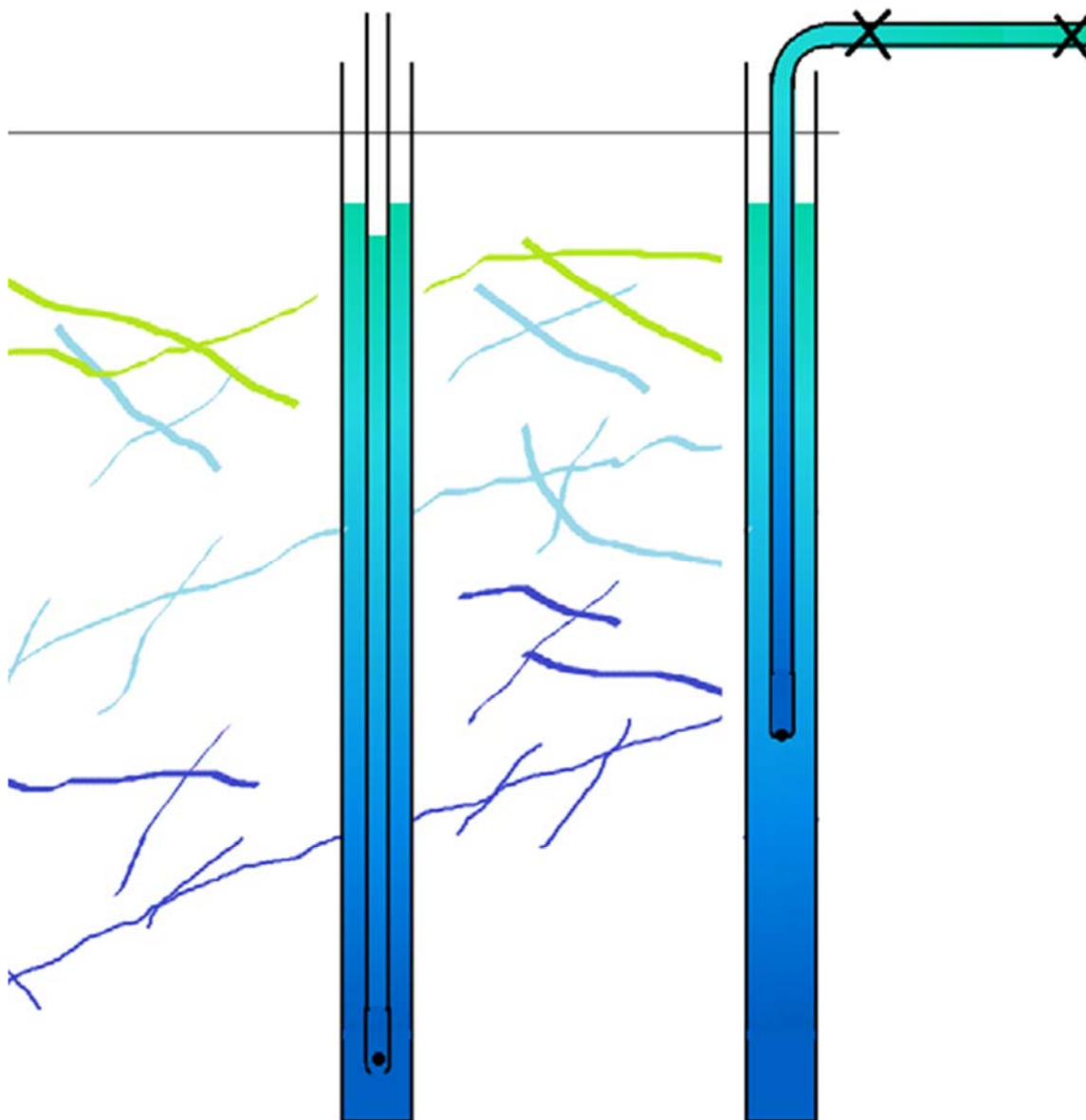


Figure 2-2. Schematic illustration of tube sampling method developed by the GTK for the COSC-1 well. On the left, the tube is lowered down to the bottom of the well and the bottom portion of the tube is sealed. The tube was lowered into the borehole slowly with the goal that the stratification of the water column chemistry would be preserved throughout the length of the tube. On the right, as the tube is raised from the hole, individual segments are crimped off, thus isolating that section of the water column.



Figure 2-3. Collection of tube samples in the field. Metal clamps were used to crimp the plastic tubing to separate out distinct sampling intervals.

The tube sampling was collected by the Geological Survey of Finland (GTK) from September 15-17, 2014, at nominal 100-m depth intervals for the entire borehole using a 1 cm Inner Diameter (ID) plastic tube. Eight sub-samples (each consisting of 6 m of tubing) near the eight inflow zones from 300 to 2500 m that were identified by FFEC logging during drilling, were collected for microbiological analysis. For the non-microbiological samples, gases were extracted from the tubing segments, and water samples were then drained to sampling bottles for analysis. Samples for cation and water stable isotope analysis were filtered ($<0.45\mu\text{m}$) and cation samples were also acidified using ultra-pure HNO_3 . Both electrical conductivity and pH were measured on site. Water chemistry analyses of the tube samples were conducted at the GTK and Labtium Oy in Espoo, Finland.

After the tube sampling was completed, two additional FFEC logging tests were conducted (Doughty et al., 2017). Unlike the tests that were conducted during the drilling operations (Tsang et al., 2016), the borehole was not flushed with fresh water prior to running the logs. For the first FFEC test, the borehole was pumped to draw down the water level in the well to 50 m below the wellhead, and the second test was run with a drawdown of 10 m. The purpose of pumping the well during the logging runs was to lower the hydrologic head in the wellbore, and thus induce water in permeable fractures to flow into the wellbore. Contrasts in fluid salinity between the original borehole fluid (as measured in the baseline FFEC run) and the fluid in the borehole measured during flowing runs when lowering of the hydraulic head of the well by pumping would thus indicate the presence of hydraulically conductive zones, where entry of fluids of distinct salinity would modify the original FFEC borehole profile around these inflow zones. Deconvolution of the FFEC curves yielded both the transmissivity of these zones as well as the electrical conductivity (EC) of the inflowing fluids and the hydraulic head for each zone. The estimated EC values for these influx zones based

on the results of all of the FFEC runs ranged from 390 $\mu\text{S}/\text{cm}$ for the shallowest inflow zone detected at 288 m depth to 2350 $\mu\text{S}/\text{cm}$ for inflow zones at 508 and 553 m (Doughty et al., 2017).

The conventional wireline downhole sampling was conducted at six depths (248, 339, 552, 699, 1216, and 1244 m) in the COSC-1 well by Lund University on October 2 and 5, 2015. The sampling depths were chosen to coincide with identified inflow zones based on the 2014 FFEC logging runs that were conducted during drilling and with examination of the recovered core samples. These samples were shipped to LBNL for microbiological and geochemical analysis. A description of the microbiological studies on these samples is presented in Dobson et al. (2016).

2.3 Electrical Conductivity Measurements

Electrical conductivity (EC) measurements of water reflect changes in salinity and temperature, where increasing temperature and increasing salinity result in higher EC values. Measurements of EC are typically corrected to a reference temperature. Two types of correction methods are generally used: a linear correction or a non-linear correction. The FFEC logging tool measures uncorrected EC values along with corresponding temperatures at each depth of measurement (every 0.1 m). Tsang et al. (2016) and Doughty et al. (2017) applied a linear temperature correction to the EC values using the correction factor (Equation 2.1) reported in Tsang et al. (1990).

$$EC(T_r) = \frac{EC_{T_m}}{1 + \alpha(T_m - T_r)} \quad (2.1)$$

where T_r is the reference temperature, T_m is the measured temperature, and α is the temperature correction coefficient of 0.022. However, a study by Mäntynen (2001) evaluating the effects of water chemistry and salinity on the temperature correction for EC suggests that the temperature coefficient (α) for this linear correction equation should be 0.0194 instead of 0.022 for fairly dilute waters. Both Tsang et al. (2016) and Doughty et al. (2017) use a reference temperature of 20°C; it is straightforward to recalculate these values to a reference temperature of 25°C, which corresponds to the EC reference temperature used for the water samples in this study.

The tube water samples were analyzed in the field using a portable WTW EC instrument. This instrument has a built-in temperature sensor, and used a non-linear function for analysis of natural waters according to the Comité Européen de Normalisation procedure EN 27 888 (DIN 38 404), with a reference temperature of 25°C. This function (CEN, 1993) can be expressed using the following two equations:

$$f_{25} = \left[(1 - a) + a \left(\frac{\eta_\theta}{\eta_{20}} \right)^n \right] \times 1.116 \quad (2.2)$$

$$\frac{\eta_\theta}{\eta_{20}} = A + \exp\left(B + \frac{C}{\theta + D}\right) \quad (2.3)$$

where f_{25} is the correction factor for 25°C, η is the viscosity of the solution, θ is the temperature at which the EC measurement was made, and the constants for the equations are as follows:

a	0.962144
n	0.965078
A	-0.198058
B	-1.992186
C	231.17628
D	86.39123

These equations (2 & 3) are appropriate for natural waters with EC_{25} values that range between 60-1000 μ S/cm, for which the samples from the COSC-1 well fall within.

To have both sets (water and FFEC) of EC measurements corrected in the same manner, the non-linear equation was used to correct the baseline FFEC data to a reference temperature of 25°C. Figure 2-4 depicts the results of using the two linear correction factors along with the nonlinear correction equation for the FFEC data. The linear correction factor curve using the correction coefficient of 0.0194 is much closer to the values obtained using the nonlinear equation. The greatest deviation is observed for the shallower (lower temperature) portion of the profile (upper 700 m), where differences of up to 100 μ S/cm occur between the values determined using the temperature coefficient of Tsang et al. (1990) and the other two curves. In general, there is good agreement between the linear correction using the 0.0194 value and the non-linear correction curve.

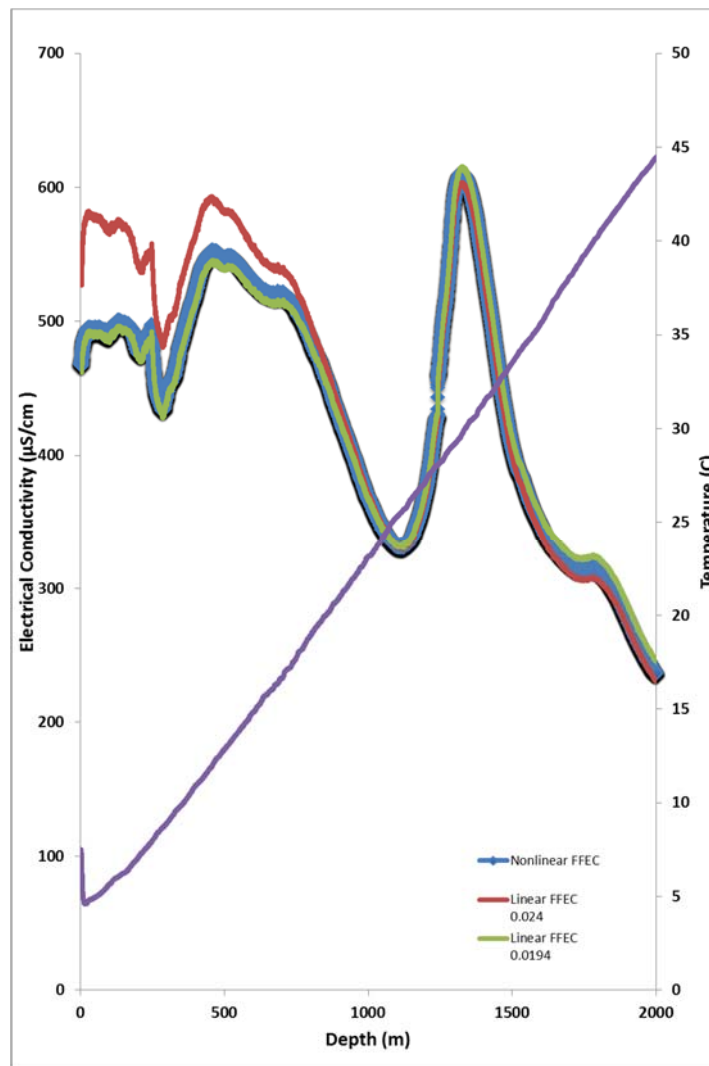


Figure 2-4. Comparison of temperature-corrected electrical conductivity values using three different correction equations and a reference temperature of 25°C. The red curve was calculated using the linear correction equation and the temperature coefficient from Tsang et al. (1990), the green curve was using the linear correction equation and the temperature coefficient from Mäntynen (2001), and

the blue curve represents a non-linear temperature correction equation for natural waters from CEN (1993). The temperature data is from the baseline FFEC log.

We used a different approach to obtain EC values for the wireline downhole sampler waters, for which EC values were not measured in the field. We used the water chemistry analyses for these as well as the tube samples to calculate EC values at the temperatures corresponding to the sampling depths and then estimated the specific conductance at 25°C using PHREEQCI (Parkhurst and Appelo, 1999) with the McCleskey et al. (2012) conductivity calculations. Good agreement was observed for all but the shallowest tube water sample between the measured and calculated EC values at the reference temperature (Figure 2-5), indicating that this approach is appropriate.

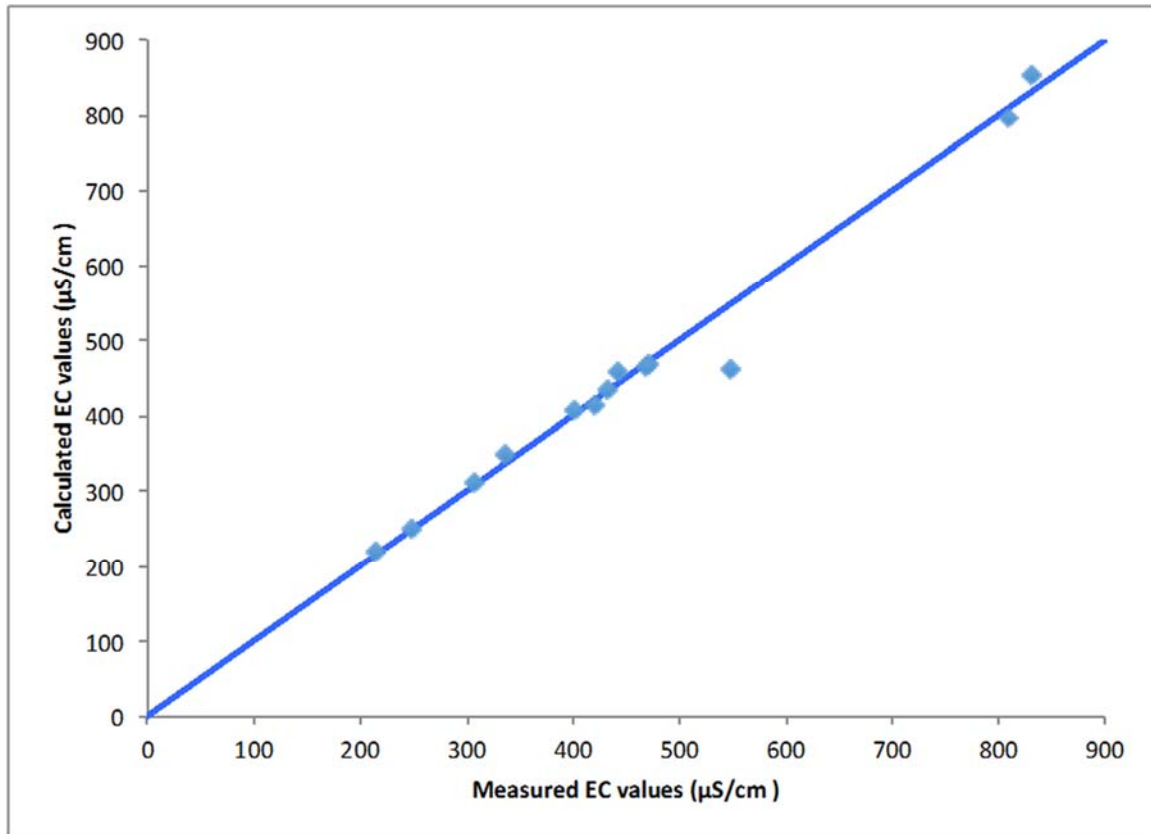


Figure 2-5. Plot of measured vs. calculated electrical conductivity values corrected to the 25°C reference temperature for the tube water samples from the COSC-1 borehole. Note that all but one of the samples falls very close to the 1:1 correlation line.

2.4 Comparison of FFEC and Downhole Water Sample Electrical Conductivity Results

As discussed above, the temperature-corrected EC values from the baseline FFEC log were compared with the EC measurements made on the tube water samples and the EC values calculated from the water chemistry analyses of the wireline downhole samples (Figure 2-6). Four sets of data are plotted on this figure – the non-linear temperature corrected FFEC values, a series of binned and averaged FFEC values to correspond directly with the tube water sample depth intervals, the tube water EC measurements, and the calculated wireline downhole sampler EC values.

The baseline FFEC log indicates several distinct water chemistry zones. From the surface down to ~220 m, the EC values are fairly constant, around 480 $\mu\text{S}/\text{cm}$. There is then a small deviation towards lower EC values, with the minima occurring around 270 m depth. The EC values then rise steadily until around a depth of 450 m. The values then decrease again, with an inflection at around 700 m depth, followed by a sharper decline in EC values down to a depth of around 1100 m. The EC values then climb again until reaching other EC maxima at a depth of around 1310 m. The EC values decline again, with another slope inflection occurring at around 1730 m, with values continuing to decrease down to the maximum depth of the FFEC log run (2000 m). With the exception of the inflections at around 220 and 700 m, these variations do not appear to correlate directly with the fluid entry points (228, 338-339, 507-508, 553-554, 696, 1214, 1243-1245, 2300, and 2380 m) identified by Tsang et al. (2016) and Doughty et al. (2017) with the flowing FFEC logs. However, the general trends of either increasing or decreasing EC values for the baseline FFEC curve do appear to correspond with trends of the calculated EC values for these detected hydraulically transmissive zones (Doughty et al., 2017).

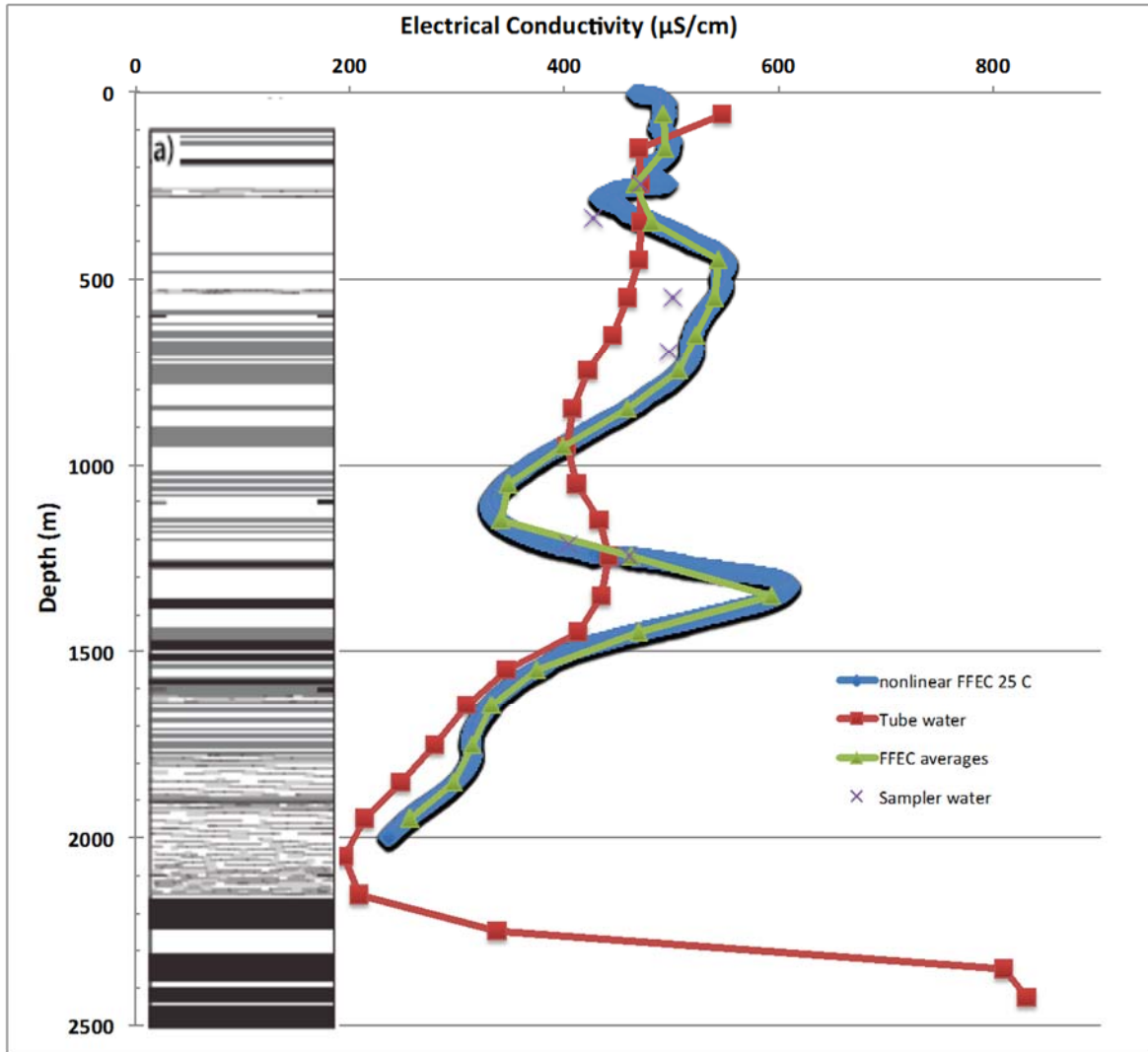


Figure 2-6. Plot of FFEC and measured tube water electrical conductivity values, both corrected to reference temperature of 25°C using the same non-linear temperature correction equation. Also plotted are the depth interval averages of the FFEC log values that correspond to the sampled depth intervals for the tube samples, as well as the calculated EC values for the six wireline downhole water samples. Stratigraphy of COSC-1 well from Wenning et al. (2017). White sections represent undifferentiated felsic lithologies, gray zones are undifferentiated mafic lithologies, lined sections indicate gneiss with mica schists and mylonite bands, and black zones represent mylonites.

The tube water samples cover the entire span of the COSC-1 borehole. There is good correspondence between the tube water EC values and the FFEC measurements at depths of 1500 – 2000 m. The tube water samples also indicate a shift towards much higher salinities in the lower 300 m of the hole, which corresponds with a change in lithology to abundant mylonites. However, above 1500 m depth, the changes in EC values that were detected in situ by the baseline FFEC log appear to have been averaged out by the tube water sample measurements. The tube water samples were collected prior to running the FFEC logs that involved pumping, so this would not be the cause for mixing of the upper tube samples.

In contrast, the calculated EC values obtained for the discrete downhole water sample suite show much better agreement with the FFEC EC values over this shallower depth interval. The downhole water samples do not reflect the composition of the inflowing fluids as determined by Doughty et al. (2017) at their corresponding fracture zones. The EC values as determined from the modeled FFEC results for some of the discrete fluid entry zones are estimated to be as high as 2350 $\mu\text{S}/\text{cm}$ – these values are more than three times greater than the highest baseline FFEC log values and the EC measurements obtained from the downhole water samples. Thus, the borehole fluids represent a mixture of distinct fluid types present in the borehole that dampen out the more saline fluid compositions. However, the wireline water samples do appear to provide an accurate reflection of the borehole fluid stratigraphy.

As noted earlier, the tube sampling method assumes that the water column stratigraphy will not be disturbed by inserting the tube into the well. However, with a deep borehole, there is more opportunity for mixing of fluids to occur during sampling using this method. This is especially likely for the upper section of the tube because the slug of water that initially captured in the tube for the shallower part of the well has to be physically displaced all the way up the length of the tube. This leads for the opportunity for non-laminar flow that would result in mixing of fluid within the tube, which would not be surprising for a body of water that passes (in the case of the upper section of the tube) more than 2000 m within a 1 cm diameter tube. It is interesting to note that this mixing may not be so significant for tube sampling over a 500 to 1000 m depth interval based on the good correlation observed below 1500 m depth. However this needs to be tested and validated.

Because the influx of water from the transmissive fractures is low, in part due to the low hydraulic head for most of these fractures, it will be difficult to collect representative samples of these fluids from an open borehole environment. Thus, the best way to sample these features would be to isolate these zones using a packer assembly and use a pump to extract fluids directly from these features. This approach has been applied successfully to a similar borehole in Finland (Nyyssönen et al., 2012; Kietäväinen, 2017). The FFEC logs collected during pumping (e.g., Tsang et al., 2016; Doughty et al., 2017) also provide insights into salinity variations associated with these zones as well as a continuous EC borehole profile.

2.5 Acknowledgments

We thank the members of the COSC scientific team for generously sharing their data and ideas on the COSC-1 project. The International Continental Scientific Drilling Program (ICDP) and the Swedish Research Council financed the drilling of the COSC-1 borehole (VR: Grant 2013–94). We thank Blaine McCleskey of the US Geological Survey for his assistance in calculating electrical conductivity values from water chemistry analyses using PHREEQCI. We thank Siegfried Forster from Xylem Analytics for providing details on the temperature compensation function of the WTW electrical conductivity instrument, and Michael Golden of LBNL for his assistance in tracking down reference materials. We also thank Nic Spycher for his scientific review of this work, and Carol Valladao and Cynthia Tilton for their editorial reviews. Funding for this work was provided by the Spent Fuel and Waste Disposition Science and Technology Campaign, Office of Nuclear Energy, of the U.S. Department of Energy under Contract Number DE-AC02-05CH11231 with Lawrence Berkeley National Laboratory. The contribution of GTK was funded by the Finnish Research Program on Nuclear Waste Management (KYT2018).

2.6 References

Ahonen, L., Kietäväinen, R., Kortelainen, N., Kukkonen, I.T., Pullinen, A., Toppi, T., Bomberg, M., Itävaara, M., Nousiainen, A., Nyyssönen, M., and Öster, M. (2011) Hydrogeological Characteristics of the Outokumpu Deep Drill Hole. Geological Survey of Finland, Special Paper 51, 151–168.

- Blomqvist, R.G. (1990) Deep Groundwaters in the Crystalline Basement of Finland, With Implications for Nuclear Waste Disposal Studies, *Geologiska Föreningen i Stockholm Förhandlingar* **112(4)**, 369-374.
- Comite European de Normalisation (CEN) (1993) Determination of Electrical Conductivity of Water. English version of DIN EN 27 888, Ref. No. EN 27 888: 1993 E.
- Dobson, P., Tsang, C.F., Kneafsey, T., Borglin, S., Piceno, Y., Andersen, G., Nakagawa, S., Nihei, K., Rutqvist, J., Doughty, C., and Reagan, M. (2016) *Deep Borehole Field Test Research Activities at LBNL*. Prepared for U.S. Department of Energy Used Fuel Disposition Campaign, FCRD-UFD-2016-000438, LBNL Report LBNL-1006044.
- Doughty, C., Tsang, C.F., Rosberg, J.E., Juhlin, C., Dobson, P.F., and Birkholzer, J.T. (2017) Flowing Fluid Electrical Conductivity Logging of a Deep Borehole During and Following Drilling: Estimation Of Transmissivity, Water Salinity And Hydraulic Head Of Conductive Zones. *Hydrogeology Journal* **25**, 501-517.
- Frape, S.K., Fritz, P., and McNutt, R.H. (1984) Water-Rock Interaction and Chemistry of Groundwaters from the Canadian Shield. *Geochimica et Cosmochimica Acta* **48**, 1616-1627.
- Frape, S.K., Blyth, A., Blomqvist, R., McNutt, R.H., and Gascoyne, M. (2004) Deep Fluids In The Continents: II. Crystalline Rocks. In: Drever, J. I. (Ed.), *Surface and Ground Water, Weathering, and Soils*. In: Holland, H.D., Turekian, K.K. (Exec. Eds.), *Treatise on Geochemistry*, vol. 5. Elsevier–Pergamon, Oxford, pp. 541–580.
- Freeze, G.A., Arnold, B.W., Brady, P.V., Sassani, D.C., and Kuhlman, K.L. (2015) Siting Guidelines for a Deep Borehole Disposal Facility. Proceedings, International High Level Radioactive Waste Management Conference 2015, Charleston, SC. 618-623.
- Friefeld, B. (2009) The U-Tube: A New Paradigm for Borehole Fluid Sampling. *Scientific Drilling* **8**, September 2009, 41-45.
- Freifeld, B.M., Trautz, R.C., Yousif, K.K., Phelps, T.J., Myer, L.R., Hovorka, S.D., and Collins, D. (2005) The U-Tube: A Novel System for Acquiring Borehole Fluid Samples From a Deep Geologic CO₂ Sequestration Experiment. *Journal of Geophysical Research* **110**:B10203, doi:10.1029/2005JB003735.
- Fritz, P., and Frape, S.K. (1982) Saline Groundwaters in the Canadian Shield – A First Overview. *Chemical Geology* **36**, 179-190.
- Gascoyne, M. (2004) Hydrogeochemistry, Groundwater Ages and Sources of Salts in A Granitic Batholith on The Canadian Shield, Southeastern Manitoba. *Applied Geochemistry* **19**, 519-560.
- Hansen, F.D., Hardin, E., and Orrell, A. (2011) Geologic Disposal Options in the USA. Proceedings, International High Level Radioactive Waste Management Conference 2011, Albuquerque, NM, 932-940.
- Hedin, P., Almqvist, B., Berthet, T., Juhlin, C., Buske, S., Simon, H., Giese, R., Krauß, F., Rosburg, J.-E., and Alm, P.-G. (2016) 3D Reflection Seismic Imaging at the 2.5 km deep COSC-1 Scientific Borehole, Central Scandinavian Caledonides. *Tectonophysics* **689**, 40-55.
- Juhlin, C., and Sandstedt, M. (1989) Storage of Nuclear Waste in Very Deep Boreholes: Feasibility Study and Assessment of Economic Potential. SKB 89-39, Svensk Kärnbränslehantering AB, Stockholm Sweden.
- Kietäväinen, R. (2017) Deep Groundwater Evolution at Outokumpu, Eastern Finland: From Meteoric Water to Saline Gas-Rich Fluid. Academic Dissertation, University of Helsinki, Geological Survey of Finland, Espoo.

- Kietäväinen, R., Ahonen, L., Kukkonen, I.T., Hendriksson, N., Nyysönen, M., and Itävaara, M. (2013) Characterization and Isotopic Evolution of Saline Waters of the Outokumpu Deep Drill Hole, Finland – Implications for water origin and deep terrestrial biosphere. *Applied Geochemistry* 32, 37-51.
- Lahermo, P., and Blomqvist, R. (1988) Influence of Mineralized Rock on Chemistry of Deep Bedrock Groundwater in Finland – With Reference to Chemistry of Surficial Waters. Geological Survey of Finland Nuclear Waste Disposal Research Report YST-62, 21 p.
- Lorenz, H., Rosberg, J.E., Juhlin, C., Bjelm, L., Almqvist, B.S.G., Berthet, T., Conze, R., Gee, D.G., Klonowska, I., Pascal, C., Pedersen, K., Roberts, N.M.W., and Tsang, C.F. (2015) COSC-1 – Drilling of a Subduction-Related Allochthon in the Palaeozoic Caledonide orogen of Scandinavia. *Scientific Drilling* 19, 1-11.
- Mäntynen, M. (2001) Temperature Correction Coefficients of Electrical Conductivity and of Density Measurements for Saline Groundwater. POSIVA OY Working Report 2001-15
- McCleskey, R.B., Nordstrom, D.K., Ryan, J.N., and Ball, J.W. (2012) A New Method of Calculating Electrical Conductivity With Applications To Natural Waters. *Geochimica et Cosmochimica Acta* 77, 369-382.
- Nurmi, P.A., and Kukkonen, I.T. (1986) A New Technique for Sampling Water and Gas from Deep Drill Holes. *Canadian Journal of Earth Sciences* 23, 1450-1454.
- Nurmi, P.A., Kukkonen, I.T., and Lahermo, P.W. (1988) Geochemistry and origin of saline groundwaters in the Fennoscandian Shield. *Applied Geochemistry* 3, 185-203.
- Nyysönen, M., Bomberg, M., Kapanen, A., Nousiainen, A., Pitkänen, P., and Itävaara, M. (2012) Methanogenic and Sulphate-Reducing Microbial Communities in Deep Groundwater of Crystalline Rock Fractures in Olkiluoto, Finland, *Geomicrobiology Journal* 29(10), 863-878.
- Parkhurst, D.L., and Appelo, C.A.J. (1999) User's guide to PHREEQC (Version 2) – A Computer Program for Speciation, Batch-Reaction, One-Dimensional Transport, and Inverse Geochemical Calculations. U.S. Geol. Surv. Water-Resour. Invest. Rep. 99-4259, p. 312.
- Ruskeenieni, T., Blomqvist, R., Lindberg, A., Ahonen, L., and Frape, S. (1996) Hydrogeochemistry of Deep Groundwaters of Mafic and Ultramafic Rocks in Finland. POSIVA report 96-21, 123 p.
- Tsang, C.F., Hufschmied, P., and Hale, F.V. (1990) Determination of Fracture Inflow Parameters with a Borehole Fluid Conductivity Logging Method. *Water Resources Research* 26, 561–578.
- Tsang, C.F., Rosberg, J.E., Sharma, P., Berthet, T., Juhlin, C., and Niemi, A. (2016) Hydrologic Testing During Drilling: Application of the Flowing Fluid Electrical Conductivity (FFEC) Logging Method to Drilling of a Deep Borehole. *Hydrogeology Journal* 24, 1333–1341.
- Wenning, Q.C., Berthet, T., Ask, M., Zappone, A., Rosberg, J.-E., and Almqvist, B.S.G. (2017) Image Log Analysis of in Situ Stress Orientation, Breakout Growth, And Natural Geologic Structures To 2.5 Km Depth In Central Scandinavian Caledonides: Results from the COSC-1 borehole. *Journal of Geophysical Research Solid Earth* 122, 3999–4019.

3. SWEDISH BOREHOLE ANALOG STUDY: COMPARISON OF FIELD AND LABORATORY FRACTURE TRANSMISSIVITY MEASUREMENTS

3.1 Introduction

This section of the deep borehole report summarizes the work that was conducted at LBNL and our collaborators from the COSC project during FY17. The main activity was hydraulic characterization of fractured core samples. Transmissivity of core samples were measured under conditions that mimicked field conditions and results were compared to field measurements.

Flow in fractured crystalline rock in the deep subsurface takes place through a fracture network, and is dependent on fracture aperture distribution and the hydraulic head field. Measurements of transmissivity in the field have been made in a fractured rock in a deep borehole in Sweden (Collisional Orogeny in the Scandinavian Caledonides - COSC). This is a scientific deep borehole project with geologic, hydrologic, and geophysical measurement goals and is centered on the drilling of two deep boreholes (2.5 km each) into crystalline rock in Sweden. One of the holes (COSC-1) was drilled in 2014 and another (COSC-2) will be drilled in 2017. Cores were collected from the first borehole over almost the entire borehole depth.

The main thrust of the COSC-1 core measurements at LBNL is to determine fracture transmissivities as a function of controlled stress in the laboratory. Cores were taken from the COSC-1 borehole in flowing zones identified from the preliminary flowing fluid electrical conductivity (FFEC) logs and selected by visual inspection for the presence of crosscutting fractures. The flowing zones are found at depths from 340 m to 2380 m, as shown in Table 1 below. The measurements were conducted under controlled stress conditions with fluid delivery and collection customized to directly investigate the effects of stress on fracture hydrologic behavior. A unique apparatus was constructed to measure multi-directional transmissivity, to assess fracture anisotropy. These transmissivity measurements were compared with in-situ fracture transmissivities based on detailed FFEC logging conducted previously.

3.2 Methodology

3.2.1 Field measurement of transmissivity (FFEC)

Flowing Fluid Electric Conductivity (FFEC) logging is a hydrogeological testing method that is conventionally applied when measuring transmissivity in an existing borehole. However, for the COSC-1 borehole, it was done within the drilling period during a scheduled one-day break, thus having a negligible impact on the drilling schedule, yet providing important information on depths of hydraulically conductive zones and their transmissivities and salinities. An additional FFEC logging data set was obtained soon after drilling was completed, also over a period of one day, but with a different pumping rate and water-level drawdown. Two additional FFEC logging tests were done about one year later in 2015. Their joint analysis, reported last year, not only resulted in better estimates of transmissivity and salinity in the conducting fractures intercepted by the borehole, but also yielded the hydraulic head values in these fractures, an important piece of information for the understanding of hydraulic structure of the subsurface. Results show that from 250 m to 2000 m depths, there are seven distinct hydraulically conductive zones with different hydraulic heads and low transmissivity values. It is of interest to compare the fracture transmissivities measured in laboratory experiments to the values inferred from FFEC logging.

3.2.2 Description of fractures

3.2.2.1 Depth/diameter/length

The cores received at LBNL are shown in Table 1. All the cores were inspected, photographed, measured, and evaluated for usability in the experiment, all cores appear to be very tight crystalline rock, although containing at least one crosscutting fracture, and some have secondary mineralization near the fractures. As the apparatus was built in FY15 to fit the geometry of Cores 188-4 and 211-2, other cores were evaluated as to whether they would work in the current system. Some of the cores were later determined unusable because of fracture condition.


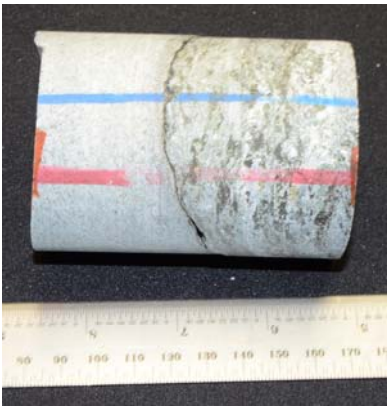
During discussion and comparison of the FY15 laboratory results with FFEC logging results from the field, it was determined that the depths from which Cores 211-2 and 188-4 did not have large signals during the field tests, so direct comparisons between field and laboratory results were difficult. In FY16, Cores 84-Z and 401-1 were selected because they corresponded to locations where a strong signal was observed during FFEC logging.

Core diameter ranged from 45 to 60 mm (1.8 to 2.4 in), and length ranged from 27 to 252 mm (1.1 to 10 in). Cores used in the FY15 and FY16 experiments are highlighted green in Table 1, and include Cores 84-Z, 188-4, 211-2, and 401-1. Pictures of the cores are shown in Table 2.

Table 3-1. Description of cores. Color code: Green - laboratory experiments completed, yellow - future lab experiments may be possible, red – condition of core precludes doing laboratory experiments.

Core ID	short name	depth (m)	Diameter (mm)	Length (mm)	Comments
5054_1_A 84-Z 3 66	84-Z	340	60	102	Transmissivity measurement in FY 2016, re-design of apparatus due to longer length
5054_1-A 116-1 20-30	116-1	434	60	100	some gaps to be filled, but would work
5054_1-A 144-2 22-32	144-2	507	60	109	significant gap on side of fracture, minor re-design of apparatus due to longer length (better than 144-1)
5054_1-A 144-1 5-11	144-1	507	60	62	large gaps in side of fracture, minor re-design of apparatus due to shorter length
5054_1-A 157-2 30-57	157-2	546	60	252	major redesign of system due to fracture geometry
5054_1_A 188-4 56-64	188-4	638	60	85	Transmissivity measurement in FY 2015
5054_1_A 209-3 19-29	209-3	696	60	100	significant gaps on side of fracture, minor re-design of apparatus due to longer length
5054_1_A 211-2 18-36	211-2	702	60	85	Transmissivity measurement in FY 2015
5054_1_A 277-4 9-15	277-4	887	60	60	minor re-design of apparatus due to longer length
5054_1_A 393-3 59-74	393-3	1219	60	135-156	not usable due to geometry and condition
5054_1-A 401-3 13-17	401-3	1241	60	33	no fracture - piece missing?
5054_1-A 401-1 56-67	401-1	1241	60	82	Transmissivity measurement in FY 2016, good fit to current system
5054_1-A 559-3 0-29	559-3	1702	45	290	not usable due to geometry and condition
5054_1_A 662-5 40-48	662-5	2290	46	80	requires re-design of apparatus due to smaller diameter and longer length
5054_1-A 662-7 27-34	662-7	2290	50	27	small diameter and shorter length would require major re-design
5054_1-A 676-6 7-17	676-6	2374	47	102	fracture has a 'Y' configuration (3 pieces); requires re-design of apparatus due to smaller diameter
5054_1-A 679-2 33-43	679-2	2389	47	100	requires re-design of apparatus due to smaller diameter and longer length

Table 3-2. Core pictures

<p>Core 188-4</p>	 A photograph of a cylindrical core sample, Core 188-4. The core is light gray with a fibrous texture. It has two horizontal blue lines and two horizontal red lines. A ruler is placed below the core, showing a scale from 40 to 150.
<p>Core 211-2</p>	 A photograph of a cylindrical core sample, Core 211-2. The core is light gray with a fibrous texture. A ruler is placed below the core, showing a scale from 30 to 140.
<p>Core 84Z</p>	 A photograph of a cylindrical core sample, Core 84Z. The core is light gray with a fibrous texture. A ruler is placed below the core, showing a scale from 30 to 150.
<p>Core 401-1</p>	 A photograph of a cylindrical core sample, Core 401-1. The core is light gray with a fibrous texture. It has two horizontal blue lines and two horizontal red lines. A ruler is placed below the core, showing a scale from 90 to 170.

3.2.2.2 CT scans

The fractured cores were CT scanned using a modified GE Lightspeed medical X-ray CT scanner to get a better understanding of fracture geometry and to estimate aperture distribution. Because the cores had to be removed from the pressure vessel to complete the scans, they were performed without applied confining pressure.

Fracture apertures were computed from the X-ray CT data. Because of the heterogeneity of the rock, the standard Missing Mass Method could not be used because its fundamental assumption is the rock is uniform. In addition, the confining pressure applied in the experiment would close the fracture, which makes the non-pressurized calculation an over-estimation. Therefore, to assess the aperture, X-ray CT values corresponding to the aperture were segmented out before the Missing Mass Method was applied to the resulting data. This approach results in a more stair-step aperture than actually exists, however does provide an understanding of the potential flow paths. Estimates of fracture aperture distribution for Cores 211-2 and 188-4 are shown in Figures 3-1 and 3-2, respectively. Similar calculations for Core 401-1 yielded an average aperture value of 0.58 mm (range 0 to 1.1 mm) and for the other cores values range from zero to almost 2 mm. Figure 3-3 is a top down view of a core showing the flow channels located around the circumference. These flow channels are numbered from 1 to 8, and flow between pairs of opposite channels is identified by flow path, e.g. Paths 1 to 5. Figure 3-4 shows CT cross sections of the cores along each flow path.

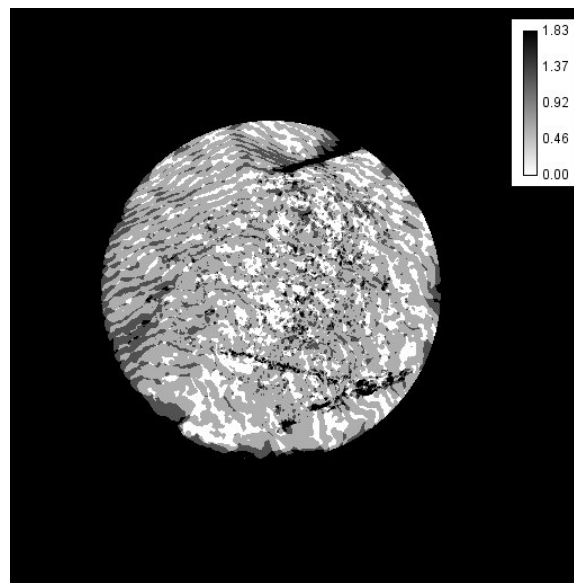


Figure 3-1. Aperture distribution (in mm) for the Core 211-2 fracture, which ranged from 0 to 1.83 mm when the sample did not have confining pressure applied. The dark sections represent larger voids within the fracture.

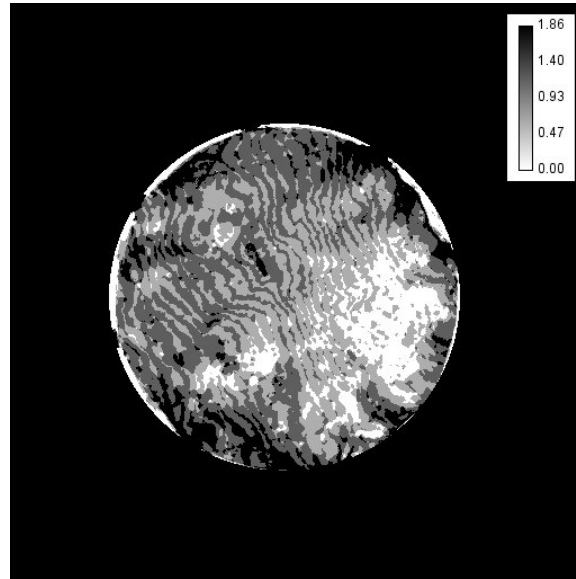


Figure 3-2. Aperture distribution (in mm) of Core 188-4 fracture, which ranged from 1 to 1.86 mm for the unconfined fracture.

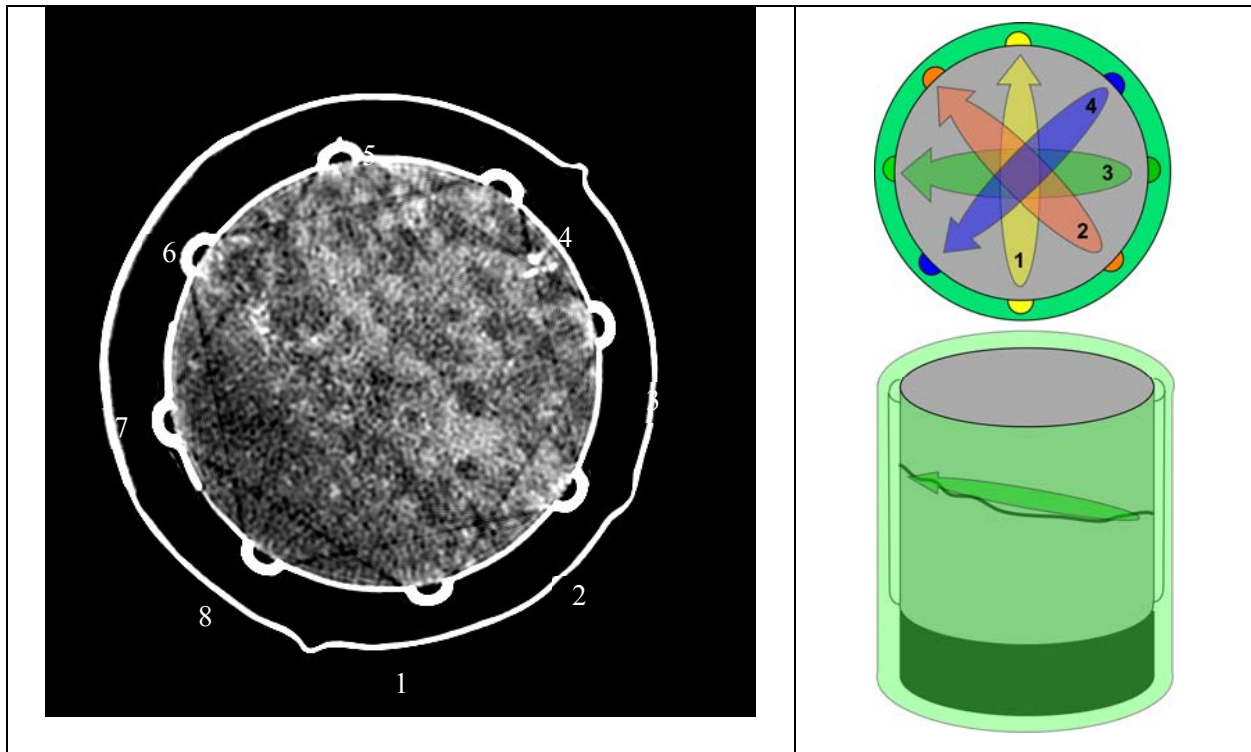


Figure 3-3. Top down view of Core 401-1 showing the eight flow channels located around the circumference. The flow channels were created with half-round stainless tubing, were held tightly to the rock with a silicone sleeve, and applied confining pressure. Flow was directed through the fracture from paths 1 to 5, 2 to 6, 3 to 7, and 4 to 8.

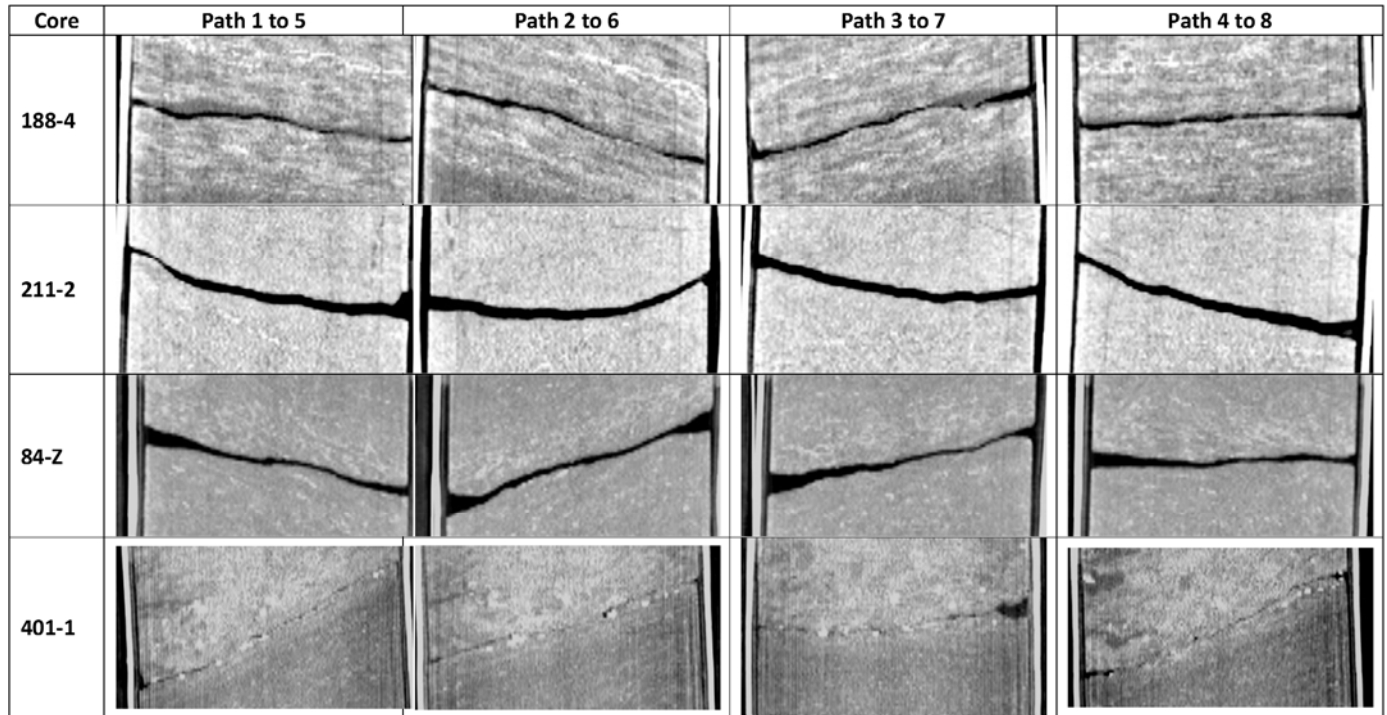


Figure 3-4. Cross section views of the flow paths in tested cores. Note that these scans were taken without any applied external confining pressure. The flow paths below were created by reslicing across the core image between the flow channels as shown in Figure 3-3.

3.2.3 Experimental apparatus

Core samples obtained from COSC were not modified during our tests with the exception of Core 211-2 where some of the gaps in the fracture edge were filled. The transmissivities were measured over a range of effective stresses (500 to 4500 psi). For the measurements a custom apparatus was constructed (Figure 3-5) allowing us to deliver water to any of four inlets distributed at 45 degree increments along the surface, and to extract water from an outlet opposite to the inlet (see Figure 3-3). The inlets and outlets are half-tubes that run along the length of the core insuring contact with the fracture.

A custom silicone rubber sleeve (Figure 3-6) was manufactured to fit around the core and inlet and outlet tubes to inhibit flow around the core. This sleeve was cast over a mockup of the setup to provide the proper fit. The top inlet and outlet support is a solid Delrin (a hard plastic) puck with holes to hold the inlet and outlet tubes on one side, and national pipe thread (NPT) fittings on the other. One-quarter inch stainless steel tubes were connected to the NPT fittings, and these were run through feed-through ports on the pressure vessel cap (Figure 3-6). Outside the pressure vessel, each tube was connected to a pressure relief valve, and then to a five-way ball valve. A solid hockey puck-shaped Delrin disk was placed at the bottom of the core and sleeve, and a thin Latex sleeve followed by a Viton sleeve was placed over the entire assembly to inhibit leaks into the assembly from the confining fluid. The assembly shown in Figure 3-5 and 3-6 was placed in a pressure vessel (High Pressure Equipment Company TOC-31-20) with an inside diameter of about 4 inches, an inside length of 20 inches and a rating of 5000 psi. Effective stresses exceeding 5000 psi would require use of a different vessel. A high-pressure precision syringe pump (Quizix Q6000) connected to a pressure port on the bottom of the pressure vessel was used to provide controlled confining pressure. Modifications were made to the silicone sleeve in FY16, mainly removing the silicone end that interfaced between the solid Delrin puck and the rock. This was done to insure that the confining

pressure was directly applied to the core, and did not cause bowing out of the sleeve. In addition, a strip of copper was placed around the core, under the silicone sleeve to help support the silicone sleeve and to keep the silicone from deforming into the fracture when confining pressure was applied. Water penetration or adsorption into the matrix is not a factor in this experiment because the rocks are tight granitic rock and flow occurs for such a short period.

Flow through the fracture was driven using another precision high-pressure syringe pump (Quizix Q6000), although flow pressures were kept below 30 psi. Flow was regulated through two 5-way ball valves (inlet tube and 4 outlets), and the pressure difference between the inlet and outlet was measured using a Rosemount 3051 differential pressure transducer and the signal recorded with a Keithley 2701 digital multimeter using Excelinx software.

To test the apparatus, a Delrin core was manufactured that was the same size as the rock cores and solid except for one 1/16 in diameter hole through the center. This dummy core was placed in the system and tested with the same range of confining pressures used for the natural cores. For the channel in line with the through-hole, very low to no differential pressure was observed indicating that flow was not restricted. For the other three paths, no flow was observed and the differential pressure steadily climbed until reaching near the limit of the system (30 psi), indicating that no flow was occurring.

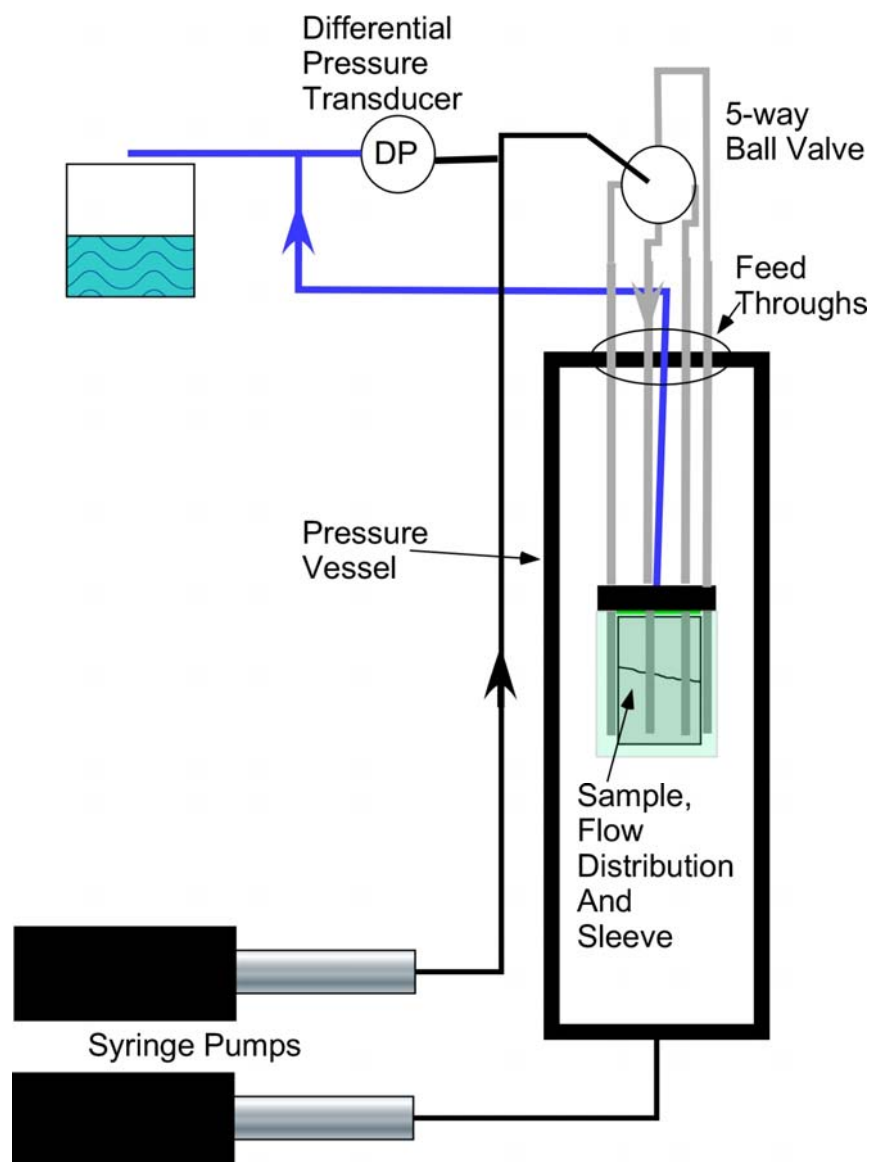


Figure 3-5. System schematic. The lower syringe pump controls confining pressure, and the upper syringe pump flows water through the core. Two 5-way ball valves (one shown) control flow to the inlet and outlet tubes.

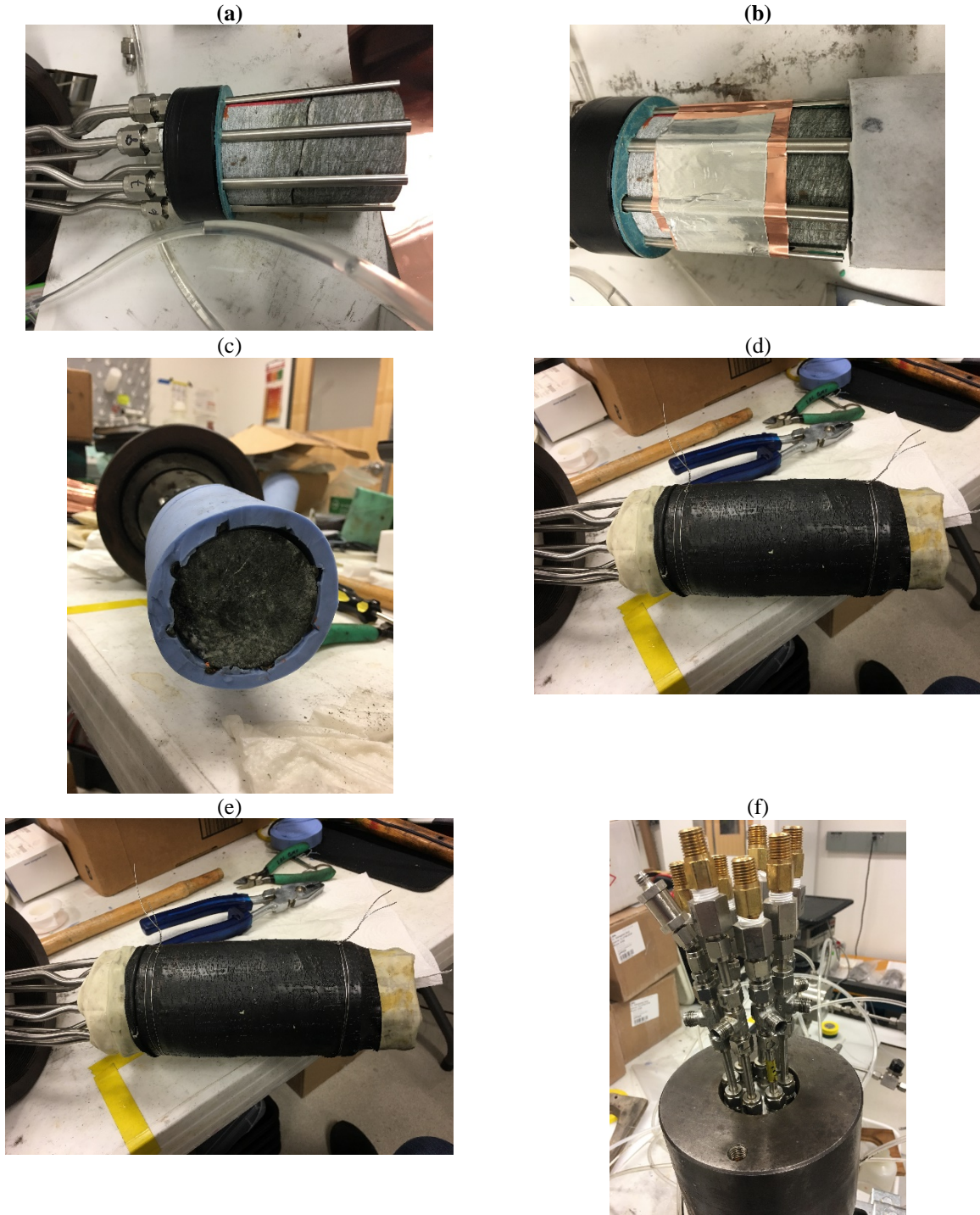


Figure 3-6. Apparatus assembly: (a) Both pieces of the fractured core are placed in between the water inlets and outlets, (b) Thin metal strips wrapped around the region containing the fracture to keep the silicone sleeve from flowing into the aperture at elevated confining pressure (used for 401-1 and 84Z cores), (c) End of core showing the silicone rubber sleeve, (d) Schematic cutout of sleeve, (e) View with outer sleeve in place, and (f) feed-through ports on the pressure vessel cap.

3.2.4 Experimental Procedure

After preparing the core as described above, the core sample was placed in the pressure vessel. The vessel was filled with water and 100 psi of confining pressure was applied to the core. It was very important at this stage that any air bubbles in the flow tubing were removed. Air bubbles in the tubing caused noise in the data and artificially increased the measured differential pressure. Confining pressure was increased to a starting value of either 500 psi (for Cores 188-4, 84Z, and 401-1) or 200 psi for Core 211-2. At this initial value, differential pressure measurements were made across each of the four pathways (1-5, 2-6, 3-7, and 4-8) for at least three different flow rates. The flow rates ranged from 0.05 to 2 mL/min depending on the transmissivity of the core. Confining pressure was then increased by a set amount and another set of differential pressure measurements was taken for multiple flow rates. This procedure was repeated over a range of confining pressures from 200 psi up to 4,500 psi. These confining pressures correspond to depths from about 61 meters to about 1370 meters to represent the in situ pressure experienced by the cores before extraction. Since the applied flow rates resulted in low differential pressures, the confining pressure can be assumed to be the effective stress on the core and no correction was needed for the pore pressure.

In some experimental runs, as part of the testing procedure the confining pressure increased to the maximum value while measuring the differential pressures for each flow path. Once a maximum was reached, the confining pressure was lowered to the original starting value.

3.3 Laboratory Results

Differential pressure/flow rate measurements were completed on crosscutting fractures through four core samples - Cores 211-2, 188-4, 84-Z, and 401-1.

To determine fracture transmissivity we begin with the following relationship.

$$\text{Transmissivity (m}^2/\text{s)} = \frac{Q\rho g l}{h\Delta P} \quad (3.1)$$

where Q = volumetric flow rate, ρ = fluid density, g = gravity, l = fracture length, h = fracture width, ΔP = differential pressure across the fracture. Equation (1) assumes a planar rectangular fracture with fluid distributed across the inlet and outlet (Figure 3-7 top). Our geometry (Figure 3-7 bottom) is different, in that water is applied over a finite length on opposite sides of a natural fracture having an approximately circular area. We corrected the relationship using the solution to a similar electrical resistance problem across a disk with finite sized electrodes (McDonald, 2000).

For the rectangular case (Figure 3-7 top), the resistance R_s across the volume is

$$R_s = \frac{1}{\sigma * t * h} \quad (3.2)$$

Therefore, the conductance C_s is the reciprocal

$$C_s = \frac{\sigma * t * h}{1} \quad (3.3)$$

where σ is conductivity, t is thickness, h is height, and l is length. For the circular case, (Figure 3-7 bottom)

$$R_c = \frac{2}{\pi * \sigma * t} \ln \frac{2D}{d} \quad (3.4)$$

and the conductance is

$$C_c = \frac{\pi \cdot \sigma \cdot t}{2 \cdot \ln \frac{2D}{d}} \quad (3.5)$$

where d is inlet/outlet length and D is fracture diameter. Letting $l = h$ and dividing Equation (3.5) by Equation (3.3) yields

$$\frac{C_c}{C_s} = \frac{\pi}{2 \ln \frac{2D}{d}} \quad (3.6)$$

which will be used as a factor to account for the geometric difference between the circular and rectangular geometry for all cores and paths. Therefore, Equation 3.1 is modified to

$$\text{Transmissivity (m}^2/\text{s)} = \frac{C_c Q \rho g}{C_s \Delta P} \quad (3.7)$$

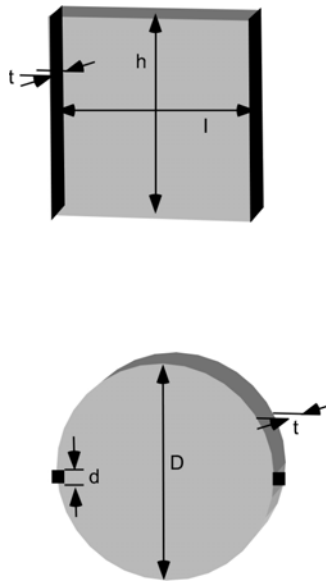


Figure 3-7. Fracture geometries used in the analogy.

3.3.1 Core 188-4, depth 638 m

Figure 3-8 shows the calculated transmissivities for Core 188-4 over the range of effective stresses. When this fracture was placed into the pressure vessel, the confining pressure was only able to reach 2000 psi before the sleeve failed. This was due to gaps in the rock along the fracture line. There was some variability in the measured transmissivity with flow path but no strong trend with confining pressure or flow path. The observed transmissivities were very high, probably due to poor fracture condition or problems due to the gaps along the fracture which possibly were allowing flow around the fracture.

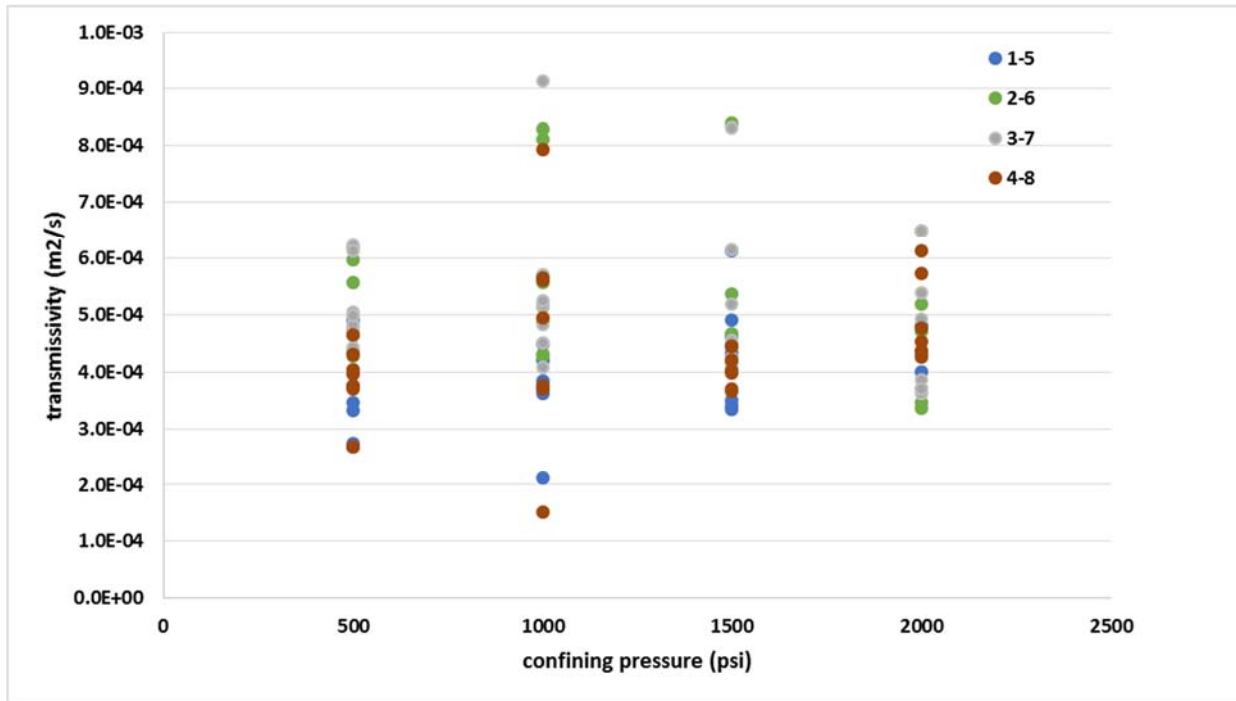


Figure 3-8. Transmissivity of Core188-4 fracture. The multiple points for each flow path at a given confining pressure represent different applied flow rates. Confining pressure increased monotonically during this experiment.

3.3.2 Core 211-2, depth 702 m

For Core 211-2 (Figures 3-9a and 3-9b), a new sleeve was made and gaps along the fracture line were carefully filled in with a non-destructive epoxy cement. For this core the confining pressure was able to reach a maximum of 4500 psi – the maximum intended pressure for the tests. Core 211-2 showed decreasing transmissivity as the confining pressure was increased to 2000 psi, when the transmissivity values appeared to stabilize (Figure 3-9a). However, as confining pressure was decreased subsequently (Figure 3-9b) the core did not reopen and the transmissivities remained low, even at reduced confining pressure. There appeared to be some consistent differences in the transmissivity of the flow paths, with the 4 to 8 path showing the highest values, and the 2 to 6 path demonstrating lower values.

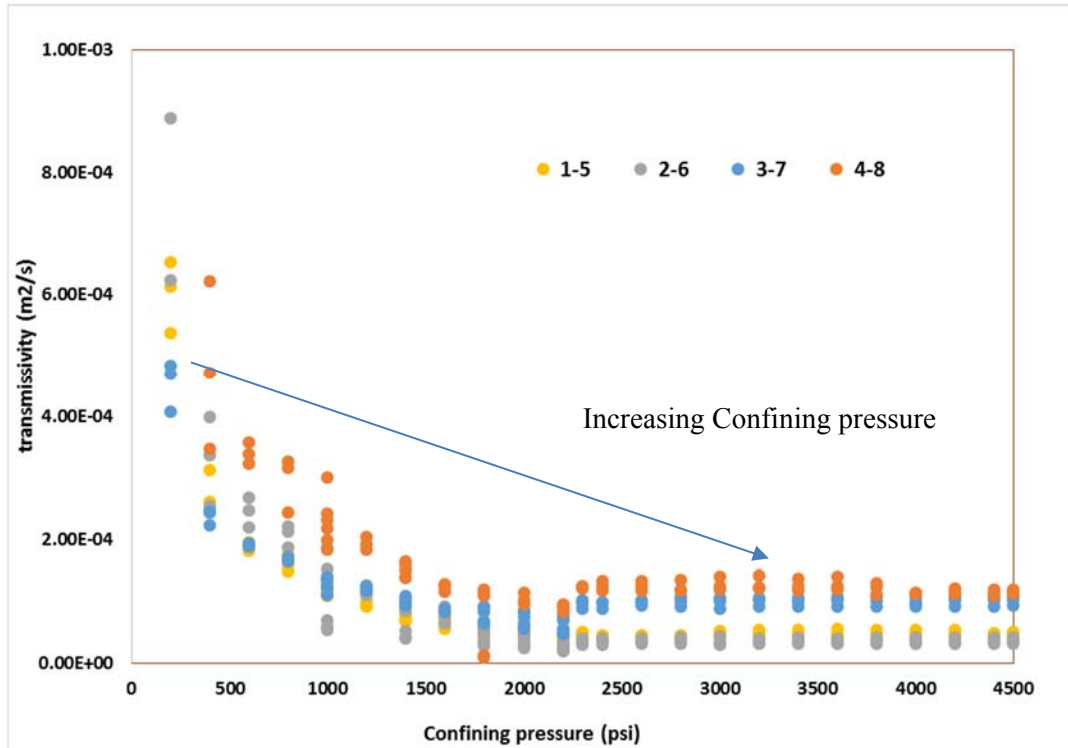


Figure 3-9a. Transmissivity of Core 211-2 fracture during increasing confining pressure. The multiple points for each flow path at a given confining pressure represent different applied flow rates.

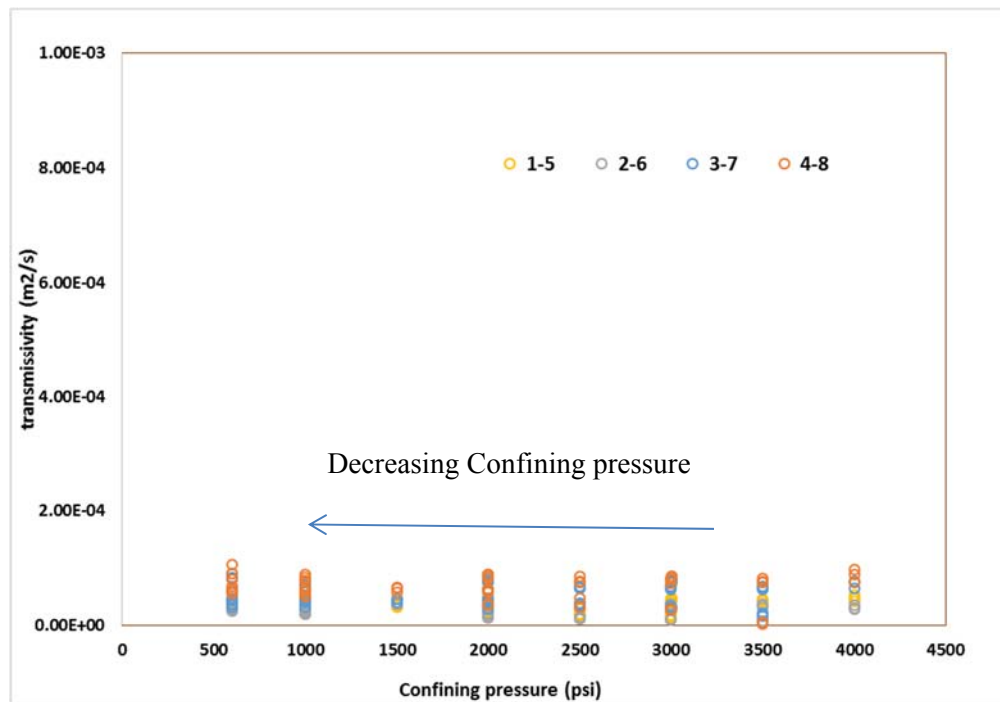


Figure 3-9b. Transmissivity of Core 211-2 fracture during decreasing confining pressure. Multiple points for each flow path at a given confining pressure represent different applied flow rates.

3.3.3 Core 84Z, depth 340 m

This shallower fracture was chosen in FY16 because its depth seemed to match field data from the FFEC. This fracture was slightly longer than the previous fractures studied, so a new sleeve was fabricated. In addition, due to wear on the edge of the fracture small pieces of compressible foam were placed on the edge of the fracture between each channel so that spurious flow around the perimeter of the core would be reduced. Maximum confining pressure was only 1200 psi because the core was recovered from a shallower depth. Figure 3-10 below shows the data from all the channels and all confining pressures. As was also seen in Core 211-2, an initial decline in transmissivity was observed with increasing confining pressure, but as the pressure was released the fracture maintained lower transmissivity. During the first pressurization, only path 4 to 8 was measured. The subsequent decreasing and increasing of the confining pressure included all the paths. Final transmissivities averaged around $1.5 \times 10^{-6} \text{ m}^2/\text{s}$ for all paths, with path 3 to 7 having the lowest average T ($1.2 \times 10^{-6} \text{ m}^2/\text{s}$), 4 to 8 having the highest average value of $2.5 \times 10^{-6} \text{ m}^2/\text{s}$ (after removing the values from the initial settling of the fracture). Paths 1 to 5 and 2 to 6 were similar, with values of $1.6 \times 10^{-6} \text{ m}^2/\text{s}$ and $1.7 \times 10^{-6} \text{ m}^2/\text{s}$, respectively. Figure 3-11 shows the data used to obtain these averages with a linear fit line through each data set. All except path 4 to 8 showed a net decrease in T with increasing confining pressure, which was mostly due to a few outliers in data. However, there is some spread in all the data and it is not clear if the observed differences in T with confining pressure and flow direction are significant.

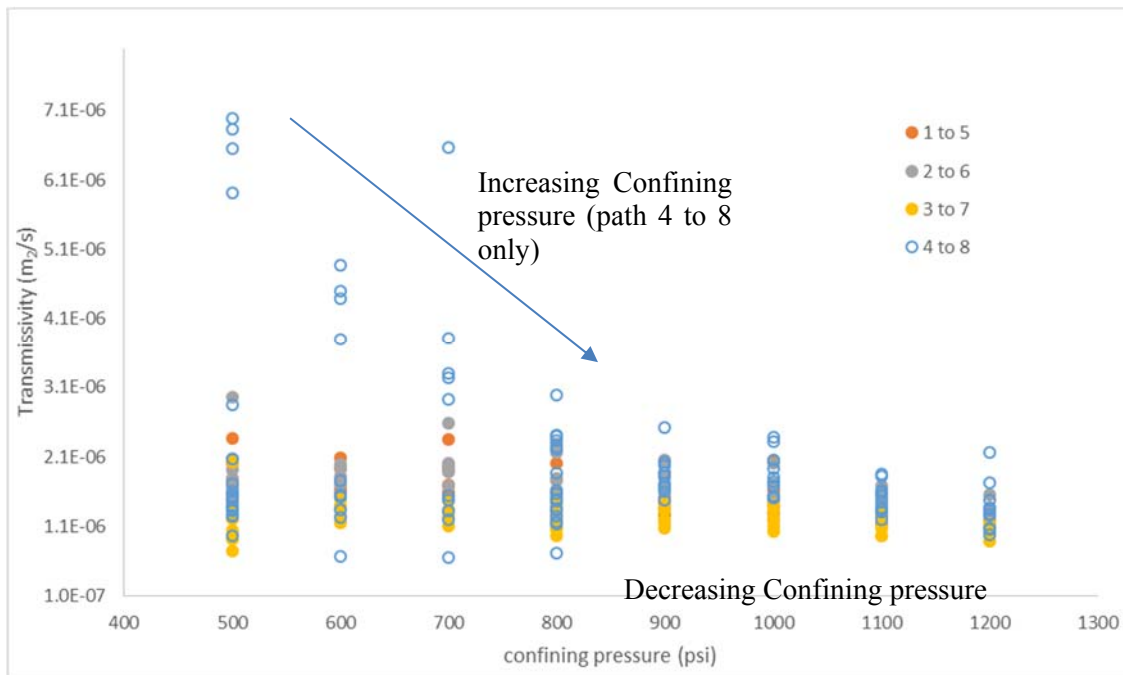


Figure 3-10. Transmissivity of the Core 84-Z fracture, as confining pressure was first increased from 500 to 1200 psi, and then was decreased back to 500 psi. Transmissivity was only determined in path 4 to 8 during the initial pressurization. The multiple points for each flow path at a given confining pressure represent different applied flow rates.

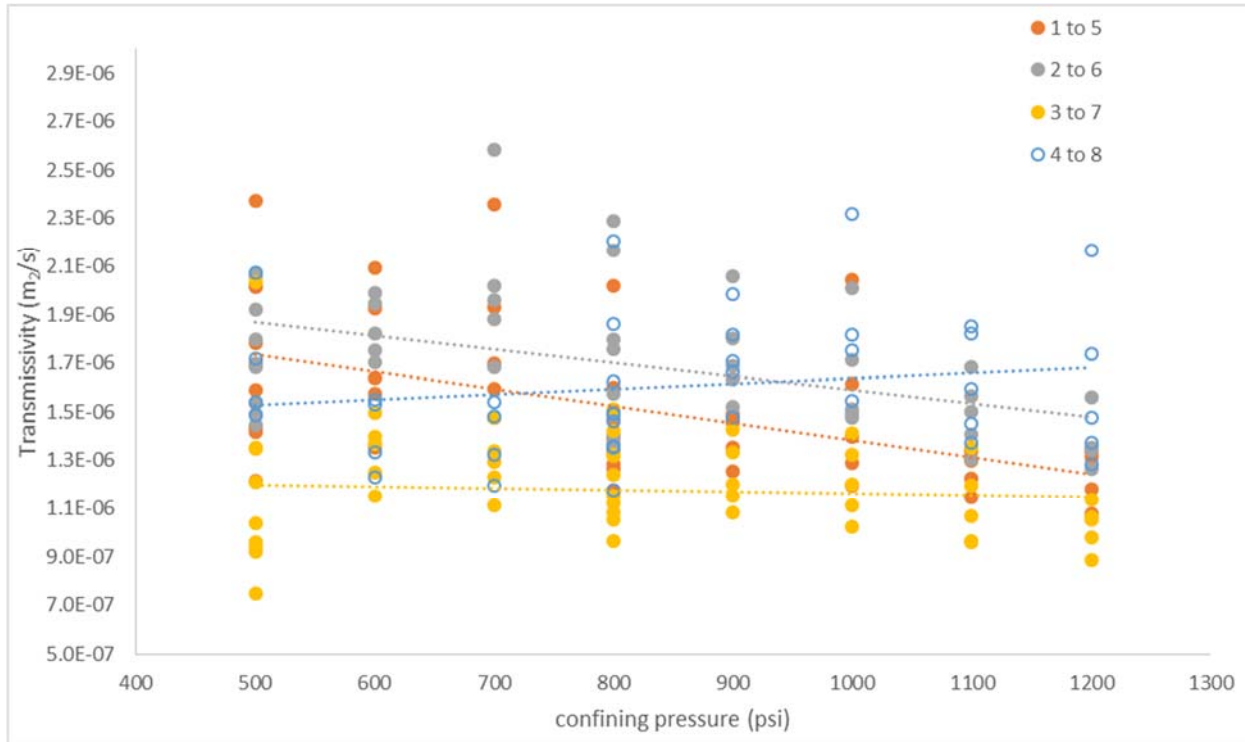


Figure 3-11. Core 84-Z fracture transmissivity with initial higher values obtained from initial settling of the fracture removed. For the points shown, confining pressure was monotonically decreased from 1200 to 500 psi. The multiple points for each flow path at a given confining pressure represent different applied flow rates.

3.3.4 Core 401-1, depth 1241 m

Core 401-1 was the deepest core sample measured in the system. Maximum confining pressure used was 3000 psi. On one portion of the fracture, near the exit of path 3 to 7, there was a missing piece of the rock, which caused problems with the sleeve at higher confining pressures. For this fracture, transmissivities on the order of 10^{-8} m²/s matched well with field values. As observed with the other cores, a tightening of the fracture was observed when confining pressure was initially increased – but after a maximum was reached and confining pressure was decreased, the transmissivity did not return to the original low values. A typical cycle of pressurization and depressurization is shown for one path in Figure 3-12 below. In Figure 3-13, the data for the initial pressurization is removed, and T was averaged over the multiple applied flow rates for each confining pressure and each flow path. Each of the flow paths showed a slight increase in T with decreasing confining pressure.

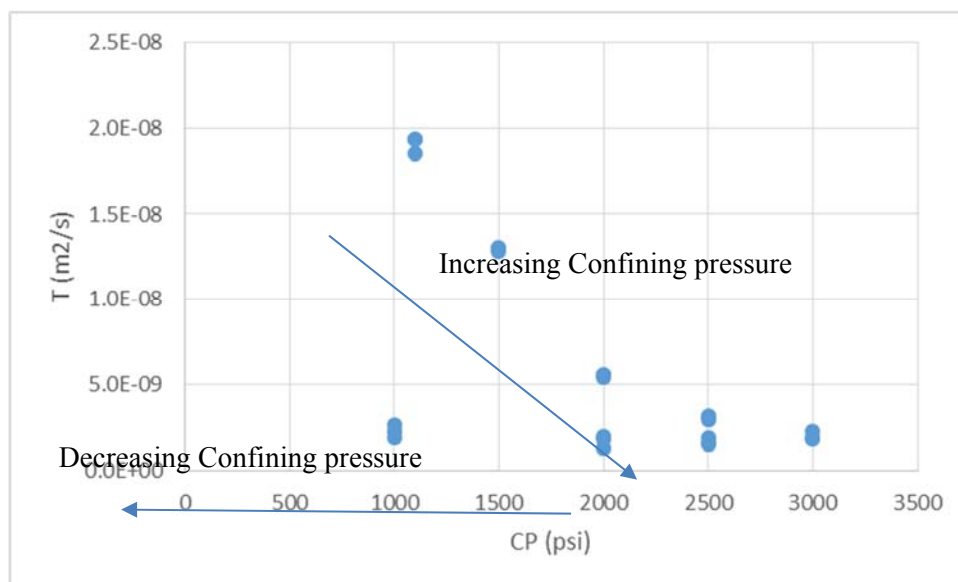


Figure 3-12. Typical transmissivity values for Core 401-1, where the first set of measurements showed tightening of the fracture with increasing confining pressure. When returning to lower confining pressure the fracture maintained a lower transmissivity.

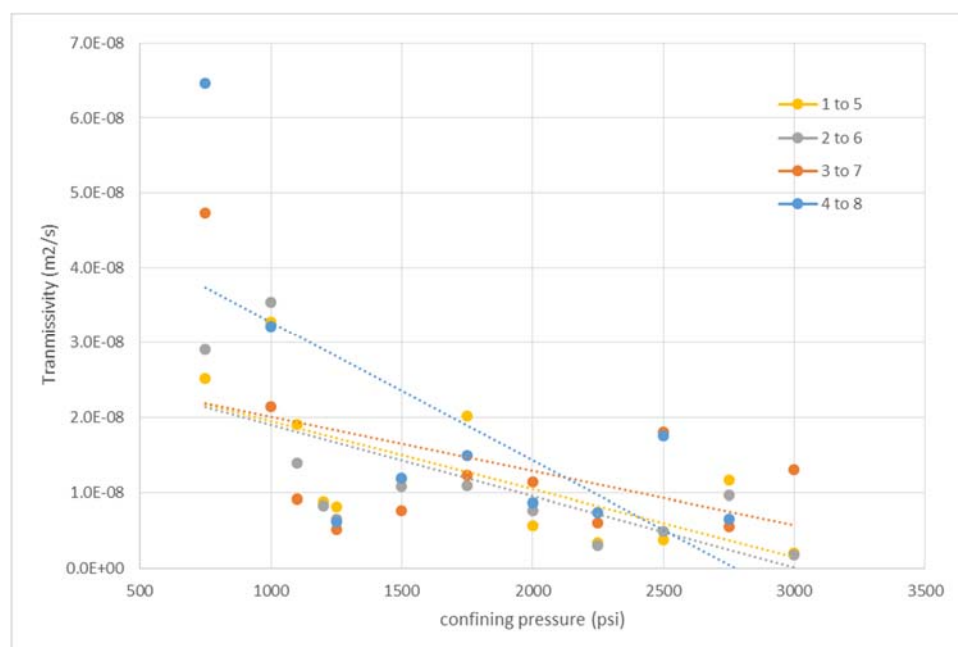


Figure 3-13. Transmissivity of Core 401-1 fracture. For the points shown, confining pressure was monotonically decreased from 3000 to 750 psi.

3.3.5 Issues with damaged/worn fractures

3.3.5.1 Flow around the core from poor fit/alignment of fractures

For the FY15 cores, the transmissivity that was measured in the laboratory appeared to be much higher than was inferred from the FFEC logs, but there were no direct comparisons between these fracture depths and observed FFEC peaks. In FY16 cores were chosen to correspond to clear peaks in the FFEC logs from the field (Doughty et al., 2017), which identify flowing fractures, so that comparison of transmissivity magnitude could be made more directly.

For Core 84-Z, the transmissivities inferred from the FFEC logs were on the order of 10^{-9} m²/s. The laboratory observations were about three orders of magnitude higher (see Figure 3-11). We believe higher transmissivities were observed in this core and in Cores 188-4 and 211-2- due to problems with the fracture condition. Specifically, for these fractures the fit was not tight, indicating that there was some wearing of the fracture surface. This was compounded in fracture 84-Z where a significant gap along the outer circumference of the fracture created a flow path for the water, circumventing the fracture. For the data shown, some packing was added to limit that flow, but even with that modification, there was not close enough surface area contact between the two halves to create a geometry for flow that was representative of the flow observed in the field.

Coe 401-1 was received in good condition and the fracture fit together nicely, with no large flow paths along the outer rim of the fracture. The transmissivity measurements from this core were comparable to those found in the field.

3.4 Comparison of field and laboratory results

Examination of core images shows many more fractures than the seven distinct hydraulically conductive zones observed as individual peaks in the FFEC logging profiles (Doughty et al., 2017). This finding is common for fractured rock, in keeping with the notion that the vast majority of observed fractures are non-conductive in situ. Thus, the issue of identifying which core sample corresponds to each FFEC peak is non-trivial. There are two key issues: aligning the cores with field measurements and the difference in depth resolution between cores and field.

3.4.1 Aligning cores with field measurements

FFEC logging requires repeated trips down a 2000 m long borehole, with the goal of measuring depths with an accuracy of about 30 cm. For an individual logging test, trips down the borehole are only hours apart, but repeated logging tests may be separated by days to months, during which wellhead conditions or tool design may change. Obtaining this accuracy is challenging and in the previous analysis of the COSC-1 FFEC logs (Doughty et al., 2017) discrepancies of 1-2 m were noticed for peak depths in different profiles, including between profiles measured only hours apart.

Recently a method of adjusting FFEC depths from different trips has been developed whereby natural gamma logs (collected concurrently with FFEC logging) are matched and the shift in depths required to get a match is applied to FFEC profiles (personal communication, Benoît Dessirier, August 2017). Signatures in the natural gamma logs over profile sections of 50 - 100 m are easy to identify and do not change in time. Depth shifts from -1 m to +2 m are required to match natural gamma profiles for the six FFEC profiles (1 baseline and 2 pumping profiles for each of two tests) collected during logging runs conducted in 2014. Figure 3-14 illustrates the shifting procedure between the two profiles of Test 1, conducted only a few hours apart, and illustrates that a shift of 2 m produces a good match between the natural gamma profiles. Doing this shifting prior to conducting the FFEC log analysis is highly recommended. If it had been done last year, it would have made the analysis procedure easier, but careful review of last year's FFEC analysis indicates that it is not likely to have had an effect on the results.

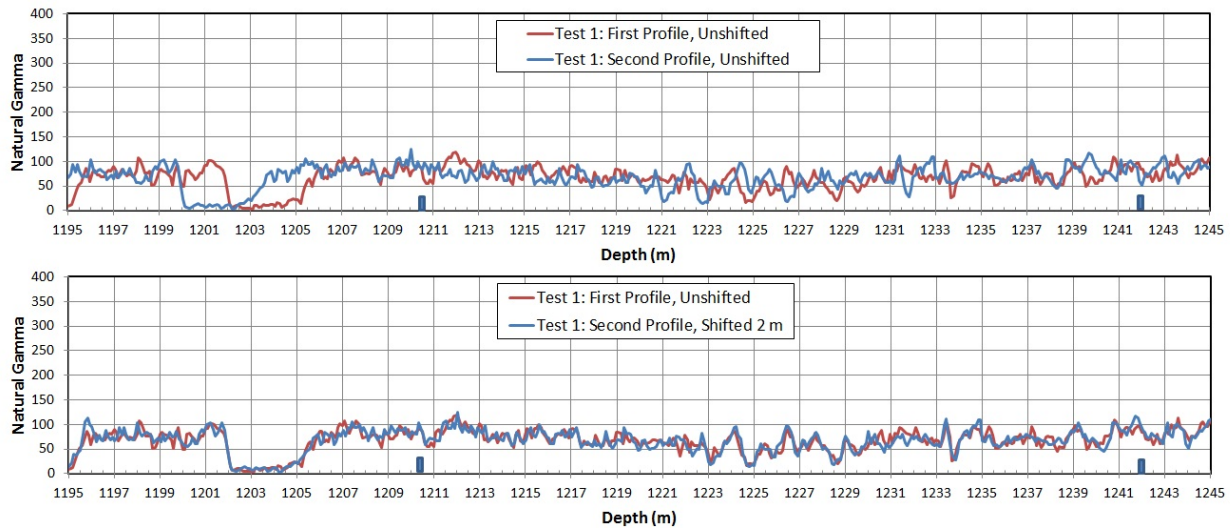


Figure 3-14. Top frame: natural gamma logs from FFEC logging Test 1 with original depths. Bottom frame: same logs with depth shifted by 2 m for the second profile. Blue bars show location of FFEC peaks.

A procedure for calibrating depths of core sample to FFEC depths using natural gamma logs has also been developed (personal communication, Benoît Dessirier, August 2017) making use of the facts that distinctive features in the acoustic televiewer can be matched to core images. The acoustic televiewer log also has a natural gamma track, which can be matched to that on the FFEC logs. This analysis confirms that none of the four core samples examined in FY15 or FY16 laboratory experiments are from a depth that corresponds to the depth of a peak in the FFEC profiles.

3.4.2 Depth resolution differences between cores and field

Theoretically, FFEC peak depth can be identified with a resolution of one to three times the borehole diameter, or within 10 – 30 cm for the COSC-1 borehole, which is 9.6 cm in diameter. However, examining the earliest time peaks shows greater spreading – about 2 m – making actual depth resolution somewhat coarser, probably in the 50 cm range. With individual core samples only 13 cm long, and many containing one or more visible fractures, unequivocally identifying the fracture that corresponds to a given FFEC peak would not necessarily be possible, even if they both had the same depth label.

3.4.3 Assessment

Because we cannot make a one-to-one comparison between the transmissivity obtained for any of the core samples and the FFEC peaks, we need to look at overall trends. The range of transmissivity obtained for various fractures using the FFEC logging covered two orders of magnitude: from $2 \times 10^{-10} \text{ m}^2/\text{s}$ to $3 \times 10^{-8} \text{ m}^2/\text{s}$. Hence, any lab results in this range should be considered a plausible reproduction of field conditions. The results of cores with several order of magnitude larger transmissivities, may be the result of damage done to the cores in the process of extracting them from the well, and should be viewed with caution.

3.5 Conclusions

3.5.1 Conclusions and lessons for future work

In this work, a novel technique was developed to investigate the effect of effective stress on transmissivity. Because the cores we received were to be returned relatively unchanged, we designed a permeability measurement system that allowed for measurements in four directions at 45 degrees from one another using one setup. Tests were performed on four fractured cores of COSC rock, at effective stresses from 200 psi to 4,500 psi. All cores had crosscutting fractures with roughly circular cross sections (perpendicular to the borehole).

We expected that transmissivity would decrease with increasing effective stress. Our measurements show that in general this is true, and significantly that this decrease is largely irreversible when stress is subsequently decreased, indicating that the fracture settles into a well mated position. The measurements also show that fracture transmissivity appears slightly anisotropic (different flow paths show different T values), and that the magnitude of transmissivity change with confining pressure depends on the flow path.

Except for Core 401-1, our laboratory transmissivity values are much higher than those inferred from field measurements are. Possible reasons for this can include the wearing of asperity contacts over long times in the field resulting in smoother local surfaces and fine particles that can reduce the available aperture for flow. In general, wear of the fracture, which can occur during extraction, shipping or handling, can have a significant influence on the ability to reproduce field results in the laboratory.

3.5.2 Further Analysis

Further analysis of the laboratory transmissivity values using numerical modeling would greatly benefit our understanding of fracture flow at the core scale, and provide a basis for scaling up to the field scale. We could confirm the validity of assumptions such as the neglect of water adsorption onto the fracture surface and penetration into the matrix. CT scans of the aperture distribution could be used to create realistic numerical models with variable aperture, which could be used to examine the actual flow geometry in the core. This would identify situations where flow is circumventing the fracture, and test the accuracy of Equation (6) for correcting from a rectangular flow geometry to the actual flow geometry for flow paths between pairs of opposite channels (Figure 3). Additionally, seeing actual flow paths would greatly aid in the interpretation of fracture anisotropy studies. Finally, different assumptions about aperture change with confining pressure could be tested. In general, developing detailed conceptual and numerical models at the core scale, where imaging and flow experiments under controlled conditions are available, will provide a strong basis for understanding fracture flow in situ.

3.6 References

- Doughty, C. Tsang, C-F., Rosberg, J-E., Juhlin, C., Dobson, P.F. and Birkholzer, J.T., (2017) Flowing Fluid Electrical Conductivity Logging Of A Deep Borehole During And Following Drilling: Estimation of Transmissivity, Water Salinity And Hydraulic Head Of Conductive Zones, *Hydrogeol J* 25:501–517 DOI 10.1007/s10040-016-1497-5
- McDonald, K.T. (2016) Resistance of a Disk, Joseph Henry Laboratories, Princeton University, Princeton, NJ, www.physics.princeton.edu/~mcdonald/examples/resistivedisk.pdf, accessed June 30, 2016)

This page intentionally left blank

4. SEAL MODELING

In this section, we present LBNL's activities related to seal modeling. We first introduce and review simulation results of the TH model simulations that were initiated in FY16 as this sets the stage for the subsequent thermal-hydrological-chemical (THC) and thermal-hydrological-mechanical (THM) model simulations. All the simulation are based on the deep borehole disposal reference design (Arnold and Hagdu, 2013) that consists of a vertical, telescoping borehole design with a 43 cm (17 inch) diameter borehole in the waste disposal zone from 3,000 m to 5,000 m depth. Waste canisters would be emplaced in strings of approximately 200 m length, separated by borehole bridge plugs to support the weight of each canister string. Following waste canister emplacement, the borehole casing would be removed from the upper 3,000 m of the borehole and a series of seals would be emplaced. Multiple boreholes would be constructed in an orthogonal array with 200 m spacing between the boreholes. In all the following simulations, we assume that the waste canisters have been emplaced and that the spacing between the boreholes is 200 m. In the thermal-hydrological (TH) modeling that were initiated in FY16, an axisymmetric model geometry was used with a radius of 100 m. Our initial approach for both the THC and THM modeling is to base them on the TH modeling, for a consistent treatment.

4.1 TH modeling of thermal pressurization and upflow through disturbed zone

In this section, we present the basic TH modeling of the deep borehole disposal that was initiated in FY16 (Dobson et al., 2016), and form the basis for our initial THC and THM modeling efforts in the following sections 4.2 and 4.3. The based TH model was developed and run in a cylindrical system within the framework of the TOUGH2 family of code, compatible with TOUGHREACT (for coupling geochemistry) and TOUGH-FLAC (for coupling geomechanics).

4.1.1 Simulation setup

The simulated zone corresponds to a single wellbore that is part of a larger field, arranged in a rectangular pattern with 200 m spacing between wellbores (Figure 4-1). The cylindrical simulated zone extends from the surface to -7,000 m, has a radius of 100 m, with no-flow boundaries at $r = 100$ m consistent with uniform 200 m wellbore spacing (Figure 4-2). The mesh contains 20,505 elements with variable refinement, including high resolution in r and z near the wellbore and near boundaries between zones of differing permeability and thermal conductivity. The wellbore, waste disposal zone, a distinct disturbed-rock zone next to the wellbore (Brady et al., 2009), and sedimentary and crystalline rock zones are all explicitly defined within the mesh to allow localized parametric variations. Rock properties for the simulated system are listed in Table 4-1.

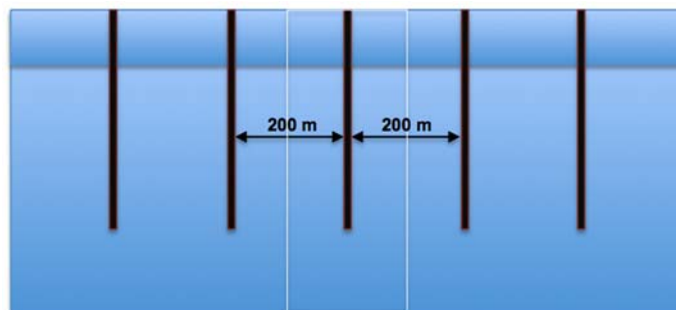


Figure 4-1. Spacing of multiple wellbores, showing 100 m simulated zone (wellbore to midpoint) and no-flow boundaries.

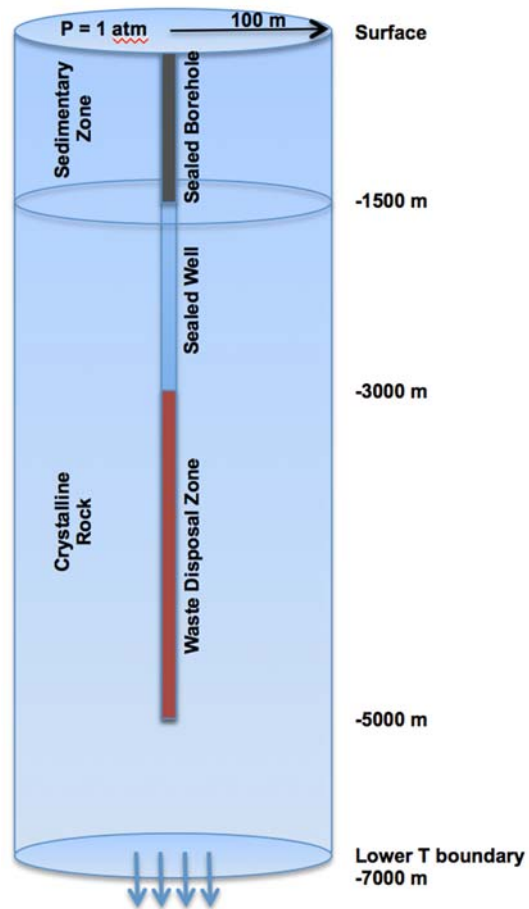


Figure 4-2. Configuration of the cylindrical simulated region, including wellbore, sealed well, waste disposal zone, and boundaries.

Table 4-1. Simulated rock properties (from Brady et al., 2009).

From: Brady et al. (SAND2009- 4401)	k (mD)	ϕ	ρ (kg/m ³)	Spec. Heat (J/kg/K)	Thermal Cond. (W/mK)
Sedimentary Rock	10/1.0	0.30	2750.0	1000.0	3.3
Crystalline Bedrock	0.0001	0.01	2750.0	790.0	3.0
Damaged Bedrock	0.2 (2.0,20.0)	0.01	2750.0	790.0	3.0
Sealed Borehole	0.1 (1.0)	0.35	2750.0	760.0	0.8
Waste/Sealed Well Casing	0.00001	0.0001	2750.0	760.0	46.0

The simulations were performed using EOS4 (Pruess et al., 1999) under fully saturated, non-isothermal conditions. The system was first equilibrated to hydrostatic conditions and a linear temperature profile of 25 °C/km (Brady et al., 2009) with constant pressure at the surface (1 atm). The waste packages were represented by a series of time-variable heat sources. The base heat curve assumes a single average pressurized-water reactor (PWR) fuel assembly aged for 25 years before emplacement (Brady et al., 2009) with an initial output of 580 W/canister. Heat output vs. time is represented by the curves designed by Greenberg et al. (2013). A second heat source is considered, with a higher initial heat output of 2,600W/canister, representative of reprocessed high-level waste aged 10 years before emplacement. The heat sources are arranged uniformly within the wellbore at depths from $z = -5,000\text{m}$ to $z = -3,000\text{m}$ (the waste disposal zone). Fully coupled, non-isothermal simulation of flow and heat transport was performed for up to 100,000 years of simulation time to assess temperature, pressure, and flow-field changes in the system. Temperatures and pressures were monitored at various radii from the midpoint of the waste disposal zone (from the package wall to the far boundary) as well as at the top of the crystalline rock zone and near the surface. Water flow was monitored in the disturbed-rock zone at multiple locations from the waste disposal zone to the surface. In addition to the base parametric cases (Table 4-1), the simulations were also run using the same initial conditions but with increased permeability of the damaged-rock zone and sealed borehole.

4.1.2 Simulation results: Thermal Response

The thermal response of the system for the 580W canister configuration resembles the behavior seen in earlier thermo-hydrological modeling (Brady et al., 2009; Arnold and Hagdu, 2013) at early times. Figure 4-3 presents temperature vs. time for monitoring points at 0 m, 1 m, 10 m, 50 m, and 100 m from the waste packages at the midpoint of the waste disposal zone ($z = -4,000\text{m}$) for both 580 W (left) and 2,600 W (right) waste canisters. For the first 100 years, we see temperatures rise steadily, reach an initial maximum and begin to decrease. The temperature increases near the borehole 580 W packages are not large and initially drop off with increasing distance from the borehole. For 2,600 W waste canisters, the temperature change is much greater, with initial temperature increases exceeding 80 °C near the wellbore.

The effect of interacting adjacent wellbores becomes apparent after 100 years of simulation. In the single-wellbore T-H study of Brady et al. (2009), temperatures drop quickly and return to near-ambient levels by $t = 10,000$ years. With multiple wellbores, temperatures begin increasing again at $t = 200$ years and climb steadily until $t = 20,000$ years as thermal disturbances from the adjacent emplacements reach the monitored elements. The second temperature peak at $t = 20,000$ years is of similar magnitude to the first peak at $t = 100$ years, but the increased temperatures persist for tens of thousands of years. Temperatures drop slowly and do not approach ambient/initial conditions until after 100,000 years.

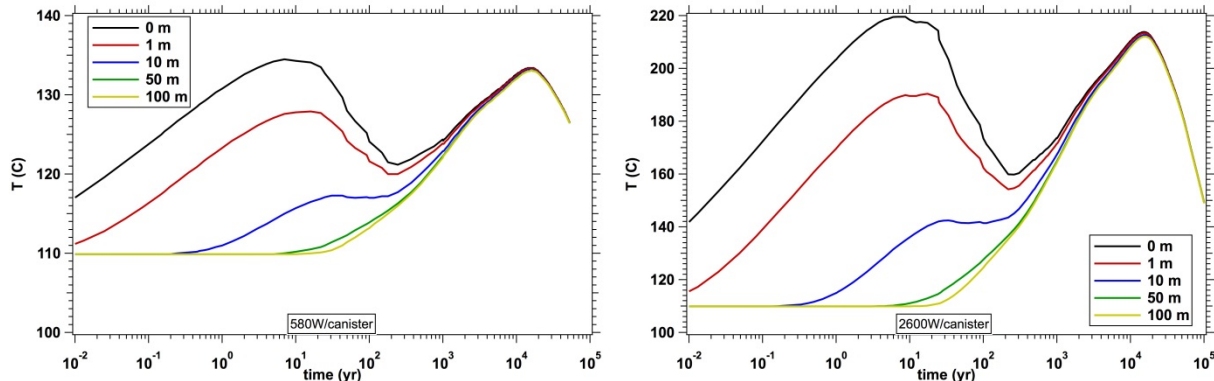


Figure 4-3. Temperature evolution at several distances from the waste packages at the midpoint of the waste disposal zone ($z = -4,000$ m) for 580 W (left) and 2,600 W (right) canisters.

Figure 4-4 presents the temperature evolution adjacent to the wellbore at varying depths: $-3,000$ m (top of waste disposal zone), $-1,500$ m (top of crystalline rock), and -500 m. We see significant temperature increases only near the top of the waste canister, with only minimal temperature effects higher in the sediment column away from the emplacement zone for the case of 580 W canisters. However, some warming is apparent within the sedimentary zone for the case of 2,600 W canisters after $t = 10,000$ yr.

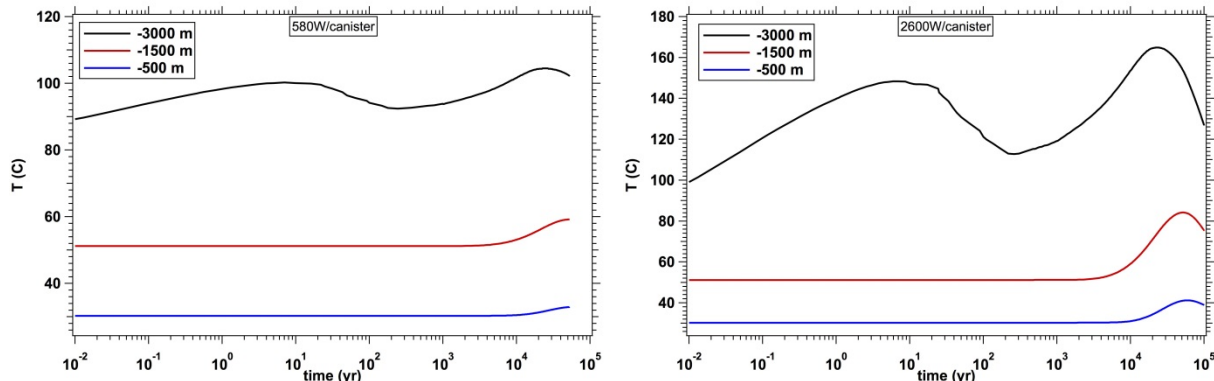


Figure 4-4. Temperature evolution adjacent to the wellbore at $z = -3,000$ m, $-1,500$ m, and -500 m ($r = 0$ m) for 580 W (left) and 2,600 W (right) canisters.

4.1.3 Simulation results: Pressure Response and Fluid Flow

The pressure response of the system to thermal changes, and the resulting fluid flow, are expected to deviate from previous single-well studies due to the lack of open/distant boundaries, the secondary thermal peak from multiple interacting wellbores, and well as differences in the assumed permeability and porosity of the near-wellbore region (including mesh geometry). Figure 4-5 presents the evolution of pressures at various distances from the waste canisters at the midpoint of the waste disposal zone ($z = -4,000$ m). For the 580 W waste canisters, pressure changes peak at +10 MPa at $t = 2,000$ years, at all monitored radii as

the thermally driven pressure changes propagate rapidly (compared to simulation time) through the low-permeability but still permeable crystalline rock. Emplacement of 2,600 W canisters results in a much larger surge in pressure, reaching +42 MPa by $t = 1,500$ years. Note that the peak in pressures corresponds to the period where temperatures at all radii begin to rise again due to thermal interaction between wellbores.

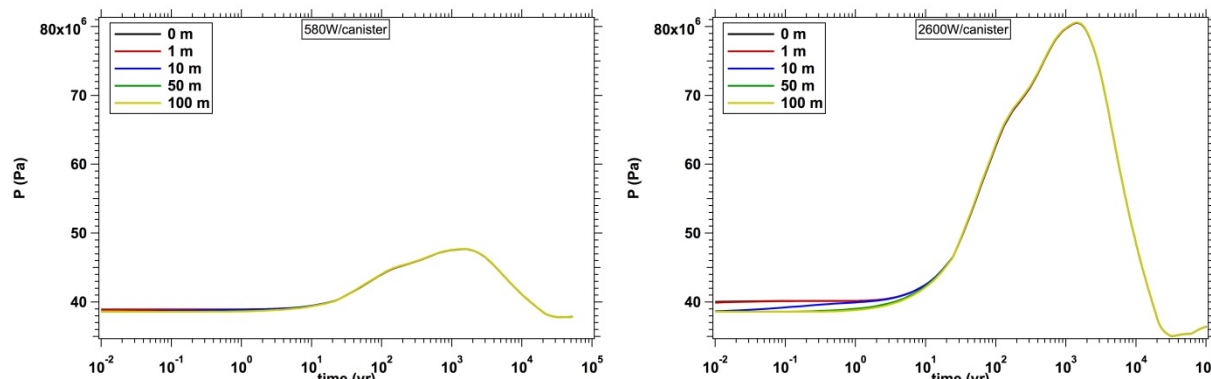


Figure 4-5. Pressure evolution at several distances from the waste packages at the midpoint of the waste disposal zone ($z = -4,000$ m) for 580 W (left) and 2,600 W (right) canisters.

Pressure changes do not propagate higher into the region around the sealed wellbore, however. Figure 4-6 presents pressure evolution in the disturbed-rock zone adjacent to the wellbore at $z = -3,000$ m (top of waste disposal zone), $-1,500$ m (top of crystalline rock zone), and -500 m. Only within the crystalline rock immediately above the heated waste disposal zone do we see large pressure increases.

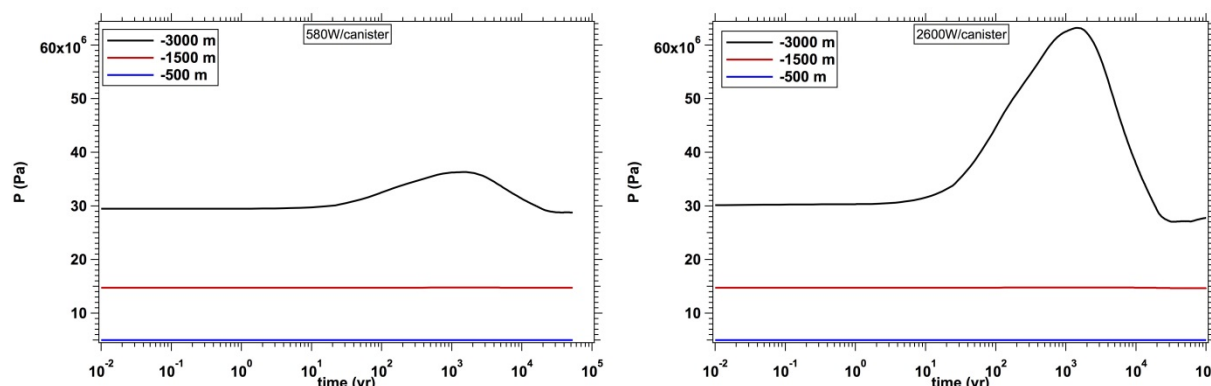


Figure 4-6. Pressure evolution adjacent to the wellbore at $z = -3,000$ m, $-1,500$ m, and -500 m ($r = 0$ m) for 580 W (left) and 2,600 W (right) canisters.

The water flows resulting from these induced pressure gradients are shown in Figure 4-7, as recorded in the disturbed-rock zone at varying depths. At the top of the waste disposal zone ($z = -3,000$ m) and at the top of the low-permeability crystalline rock ($z = -1,500$ m), we see significant upward flows of water on the order of 100s (580 W canisters) to 1,000s (2600 W canisters) of kg per year. However, once into the higher-permeability sedimentary layer, the water flows (small in magnitude compared to the volume of the permeable, saturated sedimentary layers) are not detectable at the surface. However, a significant quantity of water from within the waste disposal zone is seen to migrate above and beyond the crystalline rock layers over 100 – 10,000 yr timescales. These values are significantly higher than the upflows simulated in previous studies (Brady et al., 2009; Arnold and Hagdu, 2013), most likely due to variations in the mesh geometry and refinement (previous studies used coarser meshes, and thus will represent different cross-sectional areas for the disturbed-rock zone than stated in the well-design specifications) as well as the

increased pressure in the waste disposal zone due to increased heating from interacting wellbores. Note also that after $t = 20,000$ yr, the cooling system is now subject to downward water flows (negative Q_w) as thermal expansion of deep fluids is replaced by contraction due to cooling.

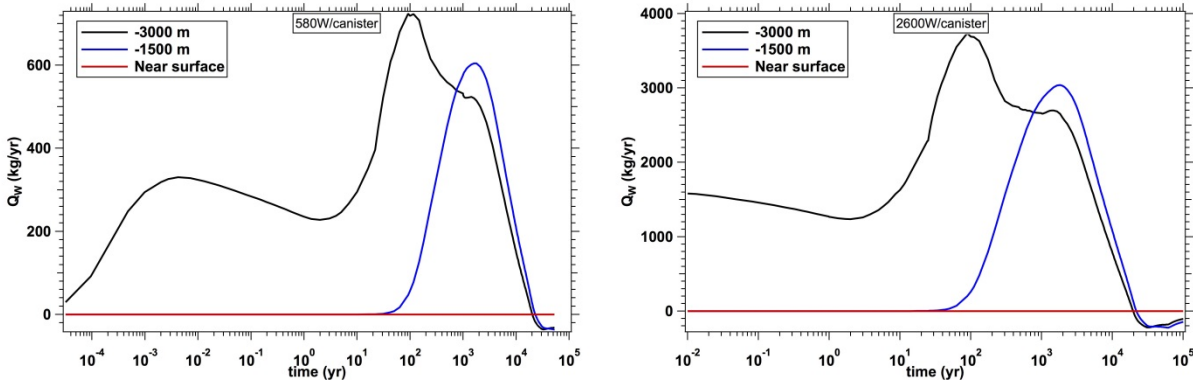


Figure 4-7. Total water flow in the disturbed rock zone adjacent to the wellbore at $z = -3,000$ m, $-1,500$ m, and -500 m ($r = 0$ m) for 580 W (left) and 2,600 W (right) canisters.

To assess sensitivity of the pressure changes and resulting flow rates, the permeability of the disturbed-rock zone was increased by a factor of 10 ($k_{DR} = 2.0$ mD) and the permeability of the sealed borehole was increased by factors of 10 and 100 ($k_{SW} = 1.0$ mD, 10.0 mD). The pressure evolution of the system with increased disturbed-rock permeability compared to the base case is shown in Figure 4-8. Increased permeability in the pathway surrounding the wellbore decreases the pressure changes by approximately 50%. This is the result, seen in Figure 4-9, of significantly increased upward fluid flow in the disturbed-rock zone despite the nearly identical thermal evolution of the system. However, the system shows no sensitivity to increased permeability within the sealed wellbore zone—increasing k_{SW} by factors of 10 and 100 gives pressure and fluid-flow values roughly identical to the base case for both 580 W and 2,600 W waste packages.

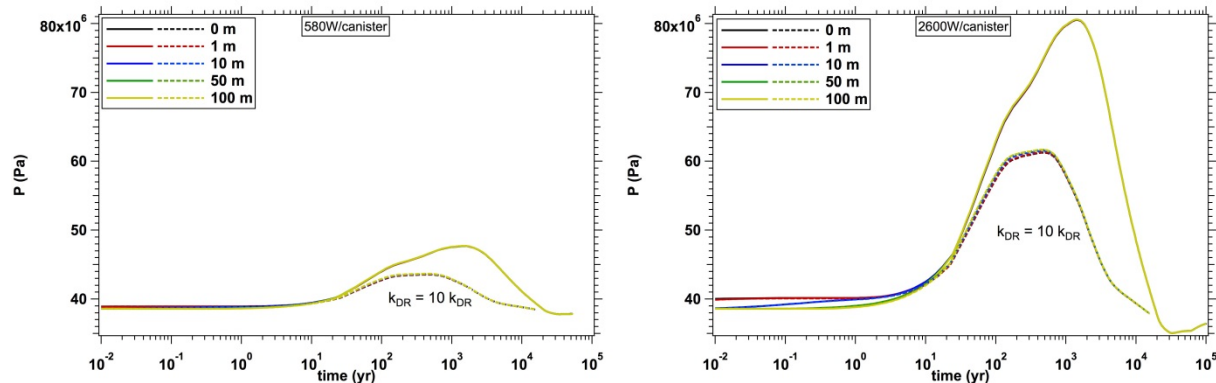


Figure 4-8. Pressure evolution adjacent to the wellbore at $z = -3,000$ m, $-1,500$ m, and -500 m ($r = 0$ m) for 580 W (left) and 2,600 W (right) canisters for the base disturbed-rock permeability and for a 10X increases in permeability.

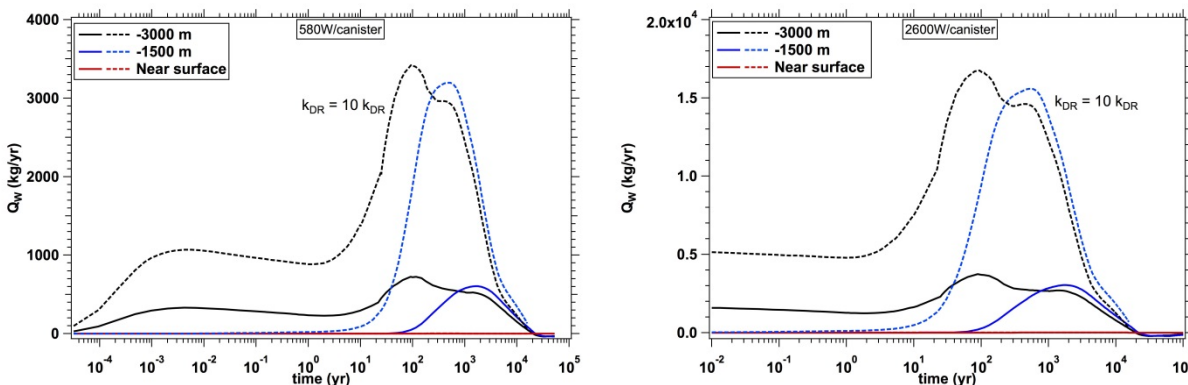


Figure 4-9. Total water flow in the disturbed rock zone adjacent to the wellbore at $z = -3,000$ m, $-1,500$ m, and -500 m ($r = 0$ m) for 580 W (left) and 2,600 W (right) canisters for the base disturbed-rock permeability and for a 10X increases in permeability.

4.1.4 TH Modeling Conclusions

The presence of a large field of wellbores and the resulting interactions between them are expected to result in greater maximum temperature and pressure changes than seen for isolated boreholes, and also create a second peak in temperature and pressure as boreholes interact at later times. This results in greater upflows of water at later times than seen in earlier studies. These results are likely different from previous work due to variations in permeabilities (especially crystalline rock) and variations in the porosity/volume of the wellbore/disturbed-rock regions (a function of mesh discretization near the borehole). Modification of the disturbed-rock radius (possibly through simple relabeling of near-wellbore mesh elements to alter the radius of higher permeability) will be used to evaluate this.

4.2 THC model for evaluating competitive processes that affect the migration of radionuclides

In this section, we discuss efforts to develop a coupled THC model for the cylindrical system using TOUGHREACT based on a TH model presented in Section 4.1 above.

4.2.1 THC simulation setup

We extended the TH model to THC model by adding chemistry using TOUGHREACT (Xu et al., 2011). The THC model therefore has the same mesh, hydrological parameters as the TH model in in Section 4.1. Because current THC model is exploratory and hypothetical, we take quite arbitrary selections of the chemical conditions of each material zone. For the top sedimentary rock, we use chemical conditions of Opalinus Clay (Lauber et al., 2000), the mineral composition is listed in Table 4-2 and the pore water composition is listed in Table 4-3.

In the current model, granite locates from depth $Z = -1500$ m to $Z = -6000$ m. Because it is unusual to see significant variation of mineralogical composition between different granite, we assumed that granite is composed of quartz, K-feldspar, plagioclase (assuming 20% albite and 80% anorthite) and muscovite (a common mica mineral) and the volume fractions of these minerals does not vary with depth (see Table 4-2). Because the salinity of the porewater for granite varies with depth, as shown in Figure 4-10, in current model, we divide the granite formation into 4 layers and salinity increases from top to bottom layer. Based on the salinity reported in Frappe and Fritz (1987), it seems that salinity increase exponentially with depth. An extrapolation based on a regression curve of data in Figure 4-10 give an salinity of 1000 g/L at 6000 m deep, equivalent to about 17 molal of NaCl, which is not possible. The granite water at the Grimsel underground laboratory in Switzerland (ENRESA, 2000) which locates at 500 depth is very dilute, with a salinity of ~ 0.002 mol/L. Huenges et al. (1997) reported that the salinity is only 60 g/L (~ 1 mol/L) at a

depth of 4000 m and a salinity of 3 mol/L at 9101 m is derived to explain the pressure profile. In this model, we create four layers of granite with fictitious initial water composition. Their compositions were created by the following method. First, assuming a linear relationship between salinity and depth determined by a salinity of ~ 0.002 mol/L at 500 m depth and a salinity of 1.5 mol/L at 6000 m, we obtained the salinity for each layer. By assuming the water is dominated by NaCl, we obtained the concentration of Na and Cl. Second, for the chemical species other than Na and Cl, we took the concentration measured at the Grimsel Underground Laboratory. Table 4-3 lists the pore-water composition of each layer.

To simplify the calculation, we assume the seal of the well is only composed of bentonite and has chemical properties of FEBEX bentonite (ENRESA, 2000).

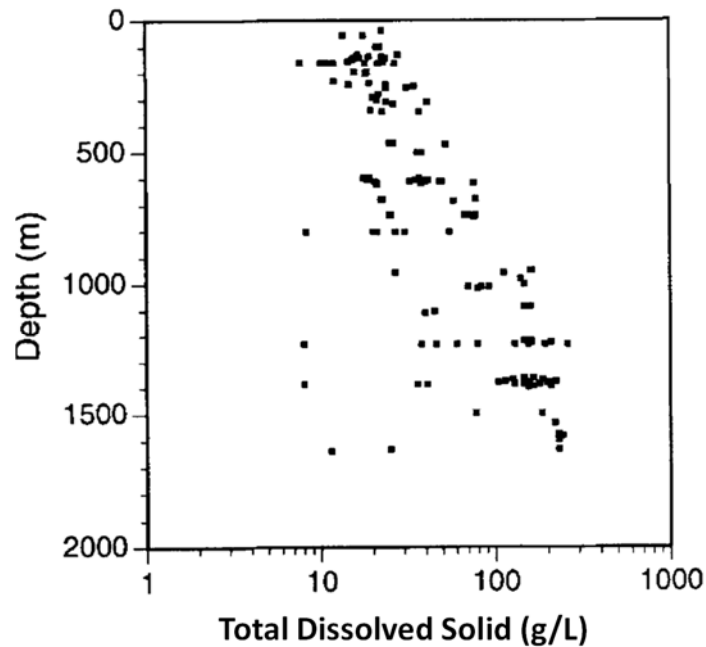


Figure 4-10. Salinity of pore fluid from crystalline rocks in the Canadian Shield (Frape and Fritz, 1987).

Table 4-2. Mineral volume fraction (dimensionless, ratio of the volume for a mineral to the total volume of medium) of sedimentary rock and granite.

Mineral	Sedimentary rock	Granite	Bentonite seal
Calcite	0.093	0.00	0.00472
Dolomite	0.050	0.000	0.546
Illite	0.273	0.000	0.0024
Kaolinite	0.186	0.000	0.012
Smectite	0.035	0.000	0.0059
Chlorite	0.076	0.000	0
Quartz	0.111	0.37	0.0
K-Feldspar	0.015	0.35	0.0
Siderite	0.020	0.000	0.0
Ankerite	0.045	0.000	0.0
Plagioclase (Ab20An80)	0	0.20	0.0
Muscovite	0	0.08	0.0

Table 4-3. Pore-water composition (mol/kg water, except pH) for sedimentary rock and granite.

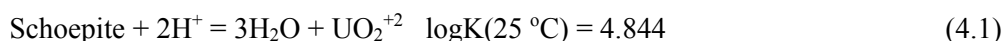
	Sedimentary rock	Granite layer 1 (1500–2500 m)	Granite layer 2 (2500–3500 m)	Granite layer 3 (3500–4500 m)	Granite layer 4 (4500–6000 m)	Bentonite seal
pH	7.40	8.35	8.35	8.35	8.35	7.72
Cl	3.32E-01	4.1E-01	6.8E-01	9.5E-01	1.5	1.60E-01
SO ₄ ⁻²	1.86E-02	7.86E-05	7.86E-05	7.86E-05	7.86E-05	3.20E-02
HCO ₃ ⁻	5.18E-03	3.97E-04	3.97E-04	3.97E-04	3.97E-04	4.1E-04
Ca ⁺²	2.26E-02	1.81E-04	1.81E-04	1.81E-04	1.81E-04	2.2E-02
Mg ⁺²	2.09E-02	1.32E-06	1.32E-06	1.32E-06	1.32E-06	2.3E-02
Na ⁺	2.76E-01	4.1E-01	6.8E-01	9.5E-01	1.5	1.3E-01
K ⁺	2.16E-03	7.80E-06	7.80E-06	7.80E-06	7.80E-06	1.7E-03
Fe ⁺²	3.46E-06	2.06E-08	2.06E-08	2.06E-08	2.06E-08	2.06E-08
SiO ₂ (aq)	1.10E-04	6.07E-04	6.07E-04	6.07E-04	6.07E-04	1.1E-04
AlO ₂ ⁻	3.89E-08	3.89E-08	3.89E-08	3.89E-08	3.89E-08	1.91E-09
UO ₂ ⁺²	1.0E-10	1.0E-10	1.0E-10	1.0E-10	1.0E-10	1.0E-10

Current chemical model considers aqueous complexation and mineral dissolution/precipitation. In addition to aqueous complexes for rock-forming elements, we also consider several aqueous complexes for radionuclides, which are supposed to be UO₂⁺², see Table 4-4. Regarding mineral dissolution/precipitation, in addition to the minerals listed in Table 4-2, schoepite is included in the model at the waste disposal zone as a source of radionuclides.

Table 4-4. Aqueous complexes for UO₂⁺².

Aqueous complexes	Reactions								Logk (25 °C)
	Stoi.	Species	Stoi.	Species	Stoi.	Species	Stoi.	Species	
UO ₂ OH ⁺	-1	H ⁺	1	H ₂ O	1	UO ₂ ⁺²			5.218
UO ₂ (OH) ₂ (aq)	-2	H ⁺	2	H ₂ O	1	UO ₂ ⁺²			12.152
UO ₂ (OH) ₄ ⁻²	-4	H ⁺	1	UO ₂ ⁺²	4	H ₂ O			32.393
UO ₂ CO ₃ (aq)	-1	H ⁺	1	HCO ₃ ⁻	1	UO ₂ ⁺²			0.396
UO ₂ (CO ₃) ₂ ⁻²	-2	H ⁺	2	HCO ₃ ⁻	1	UO ₂ ⁺²			4.048
UO ₂ (CO ₃) ₃ ⁻⁴	-3	H ⁺	3	HCO ₃ ⁻	1	UO ₂ ⁺²			9.141
CaUO ₂ (CO ₃) ₃ ⁻²	-3	H ⁺	1	Ca ⁺²	3	HCO ₃ ⁻	1	UO ₂ ⁺²	3.806
Ca ₂ UO ₂ (CO ₃) ₃	-3	H ⁺	2	Ca ⁺²	3	HCO ₃ ⁻	1	UO ₂ ⁺²	0.286

The release of radionuclides from canister and their migration in the surrounding environment is a very complex process and is very challenging, if possible, to be realistically reproduced with one model. In current modeling exercise, as the first step to study the migration of radionuclides in the deep borehole repository, we solely focus on two processes: advection and diffusion of radionuclides from the waste disposal zone. With this in mind, we greatly simplify the process of radionuclides release and migration with the following assumptions. First, it is assumed that UO₂⁺² is released by the dissolution of schoepite. As the waste packages degrade, the U concentration is controlled by the least soluble uranium phase that is stable under the given geochemical conditions. To be conservative, and for reasons of simplicity, the source concentration of uranium is usually determined by the solubility of the U(VI) phase that is possibly present in the given performance assessment environment. After an evaluation of the possible U(VI) minerals, Bernot (2005) selected schoepite as the controlling phase, because laboratory studies of Wronkiewicz et al. (1996) showed it to be the dominant early-formed phase in UO₂(s) degradation. In this report, we take the same strategy and assume that the waste package is composed only of schoepite; the concentration of U(VI) is then controlled by the following reaction:



Second, we assumed that schoepite start dissolving from time zero. This assumption is at best representing worst scenario, and is taken mostly for pragmatic reason. Despite all the uncertainties associated with the corrosion rate of canister, it is expected that canister is not fully corroded after at least a given time, maybe ranging from 1000 to 100,000 years. However, if we start the dissolution of schoepite years later, like the model in Zheng et al. (2012), or 10,000 years later like the model in De Windt et al. (2008), then heat releasing phase is well passed and upwards advection due to the thermal pressurization does not exist anymore, we cannot study the advection of radionuclide. In order to evaluate the advective transport of radionuclide versus diffusive transport, we assumed that schoepite starts dissolving from time zero.

Third, in the reference design of deep borehole disposal (Arnold and Hagdu, 2013), a thin layer of bentonite buffer surrounds the canister. As a result, even after the canister is fully corroded, the bentonite buffer will delay the time that the radionuclide arrives at the damaged zone in granite. In the current model, we assume that radionuclide is transported to a damaged zone in granite immediately after schoepite starts dissolving. In other word, the adsorption of radionuclide in the bentonite buffer is neglected.

4.2.2 Simulation results

In the TH modeling in Section 4.1, several scenarios with different heat release and permeability of damaged zone were modeled. For the THC model, we pick the case with an initial output of 580 W/canister and 20 mD for the permeability of damaged zone. Thermal and pressure response, fluid flux at couple observatory points are briefly recapped here to facilitate the discussion of radionuclide transport later.

Figure 4-11 presents temperature vs. time for monitoring points at 0 m, 0.3 m (located in the damaged zone), 1 m, 10 m, 50 m, and 100 m from the waste packages at the midpoint of the waste disposal zone ($Z = -4,000$ m) for 580 W waste canisters. For the first 100 years, we see temperatures rise steadily, reach an initial maximum and begin to decrease. The effect of interacting adjacent wellbores becomes apparent after 100 years of simulation, as the temperatures begin increasing again at $t =$ two hundred years and climb steadily until $t = 20,000$ years as thermal disturbances from the adjacent emplacements reach the monitored elements. Then temperatures drop slowly and do not approach ambient/initial conditions until the end of simulation.

Figure 4-12 shows the evolution of pressures at several radial distances from the waste canisters at the midpoint of the waste disposal zone ($z = -4,000$ m). Initially at all these distances pressures are the same because all these points locate at the same depth. Shortly after the temperature increase, the pressures at these locations differ and create a flux outwards from the waste canister toward surrounding granite (see Figure 4-13). When temperature at locations far away from the waste package increase, for example the temperature at radial distance of 50 m and 100 m (Figure 4-11), pressure at these locations start increasing, and as a result, outwards flux decrease and eventually an inwards flux is created (Figure 4-13). Pressure changes peak at 200 years with about 30 bars increase from initial value, at all monitored radii. However, because there is almost no pressure difference at these locations (Figure 4-12) after 200 years, there is minimal flux from about 200 years until the end of simulations (Figure 4-13). The temperature, pressure and flux at several radial distances evolve almost concurrently, which shows the pressure and flux is thermally driven.

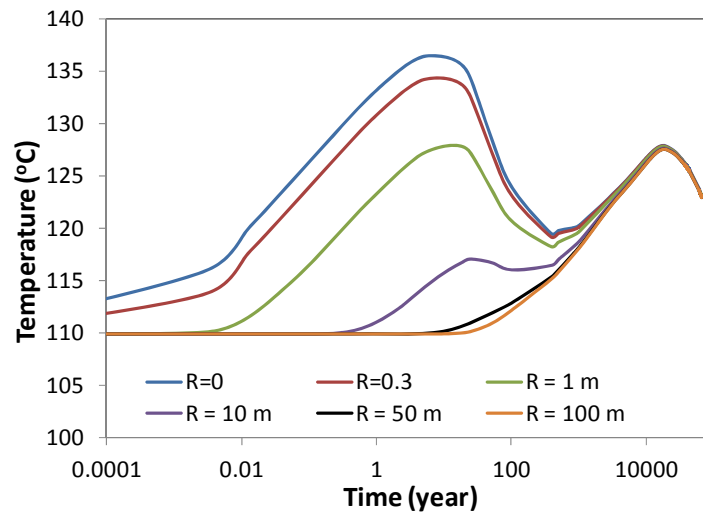


Figure 4-11. Temperature evolution at several radial distances from the waste packages at the midpoint of the waste disposal zone ($Z = -4,000$ m).

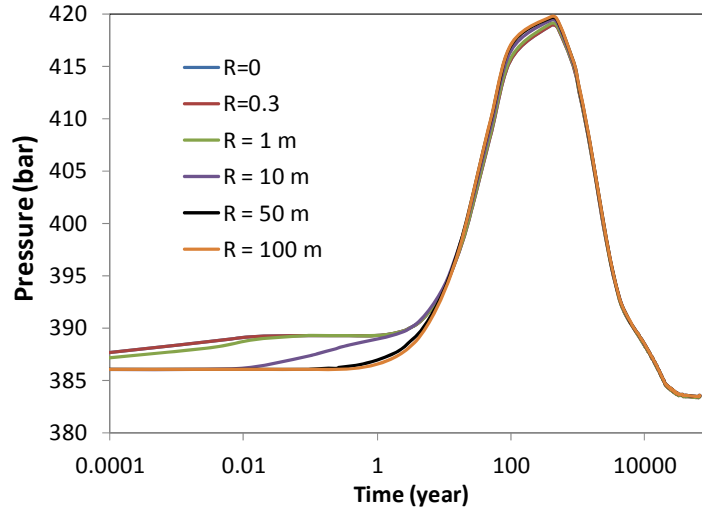


Figure 4-12. Pressure evolution at several radial distances from the waste packages at the midpoint of the waste disposal zone ($z = -4,000$ m) for 580 W canisters.

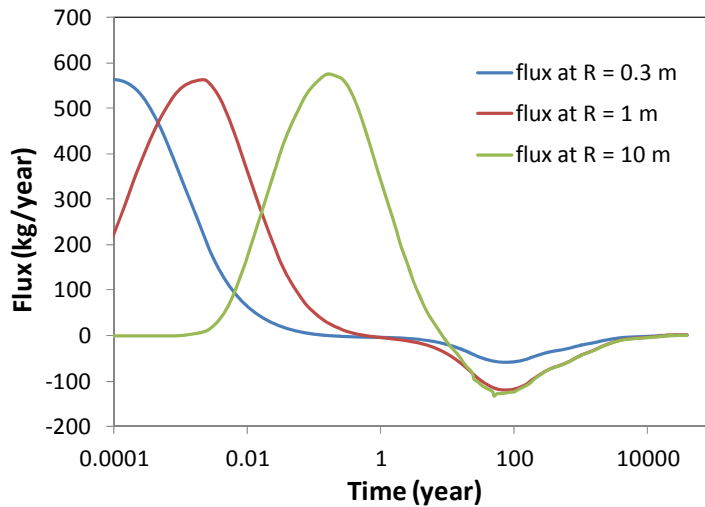


Figure 4-13. The flux (kg/year) at several radial distances from the waste packages at the midpoint of the waste disposal zone ($z = -4,000$ m). Positive value indicates that the flux is outwards from the waste packages and negative values mean the flux is inwards the waste packages.

As mentioned above, schoepite, a uranium bearing mineral is assumed to dissolve at beginning, as a result, uranium concentration quickly increase to 3.7×10^{-7} mol/L at waste package ($R = 0$) and remains at this level until the end of simulation (Figure 4-14). The outwards flux from waste package to the granite in the early time (see Figure 4-13 for the water flux) carries the uranium to surrounding granite and causes increase in uranium concentration, as shown by the concentration of uranium at radial distance 0.3 m, 1 m, 10 m, 50 m and 100 m before 100 years in Figure 4-14. After that, when flux becomes inwards (see the negative flux in Figure 4-13), the concentrations of uranium at these locations become stagnant around 200 years. After this stagnant phase, the diffusive flux carries uranium outwards and leads to increase in concentration of uranium until the end of simulation.

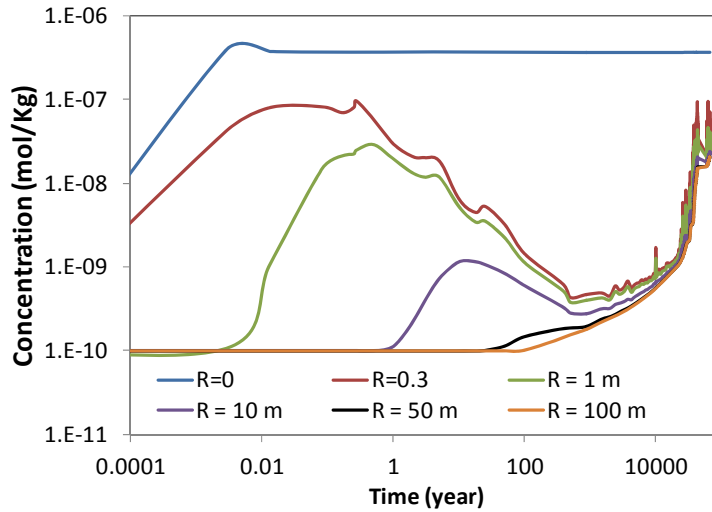


Figure 4-14. Uranium concentration at several radial distances from the waste packages at the midpoint of the waste disposal zone ($z = -4,000$ m).

Figure 4-15 presents the temperature evolution in the damaged zone (adjacent to the wellbore) at several depths including $Z = -3,000$ m (top of waste disposal zone), $Z = -2,950$ m (50 m above the waste disposal zone), and $Z = -1,500$ m (top of granite). We see significant temperature increases only near the top of the waste canister, with only minimal temperature effects higher in the sediment column away from the emplacement zone for the case of 580 W canisters, even just 50 m higher at $Z = -2,950$ m. However, the second temperature pulse due to the interaction with the adjacent boreholes start taking effect and cause the increase in temperature starting roughly from 200 years. The early increase in temperature in the first 100 years near the waste package at $Z = -3,000$ m (see Figure 4-15) leads to an increase in pressure (Figure 4-16) and an upwards flux at $Z = -3,000$ m (Figure 4-17). When interaction between boreholes drives the temperature increase at locations far above the waste package after 200 years (Figure 4-15), pressures rise at these locations (Figure 4-16) and an upwards flux is produced (Figure 4-17).

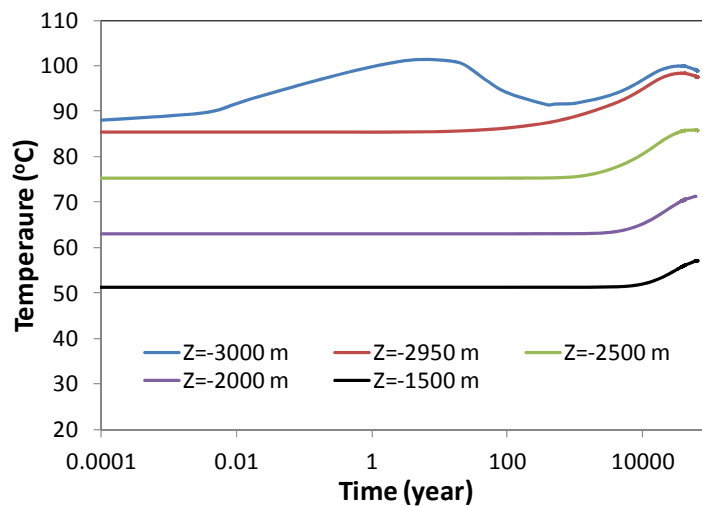


Figure 4-15. Temperature evolution in the damaged zone (adjacent to the wellbore) at several depths.

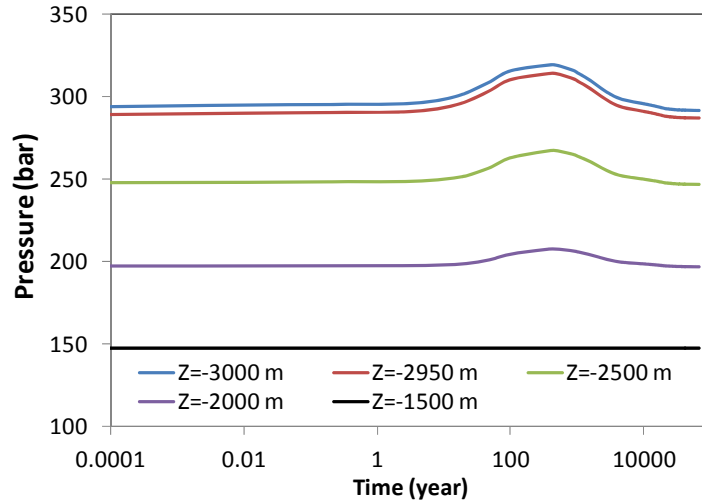


Figure 4-16. Pressure evolution in the damaged zone (adjacent to the wellbore) at several depths.

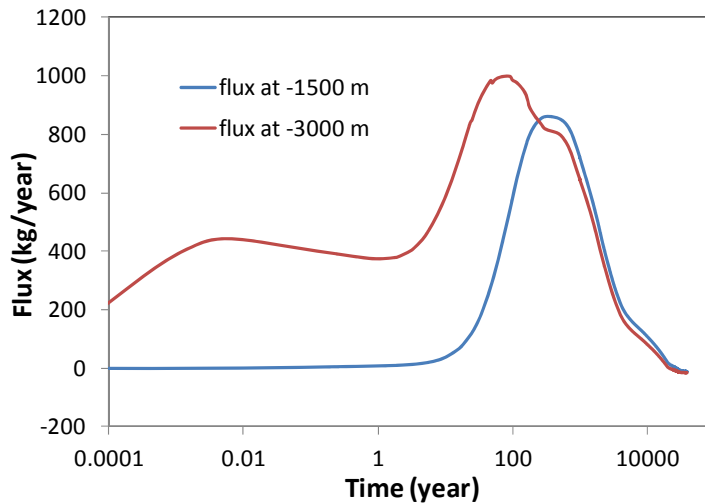


Figure 4-17. Flux in the damaged zone (adjacent to the wellbore) at several depths. Upwards flux is positive.

Figure 4-18 shows the uranium concentration along the damaged zone at different depth. Because thermal propagation is limited to the close vicinity of waste package, up to 50 m away from the waste package, thermal pressurization at the early time (roughly the first 100 years) induces an upwards flux above the waste package, which leads to increase in uranium concentration at $Z = -3,000$ m and $Z = -2,950$ m. No noticeable uranium concentration increase was observed (Figure 4-18) in the first 100 years at $Z = -2,500$ m, which indicates that the migration of radionuclides by advective flux is very limited in vertical direction. However, the migration of uranium by the diffusive flux becomes important at later times, and eventually we observed increase in uranium concentration at depth of $Z = -2,000$ m after 20,000 years.

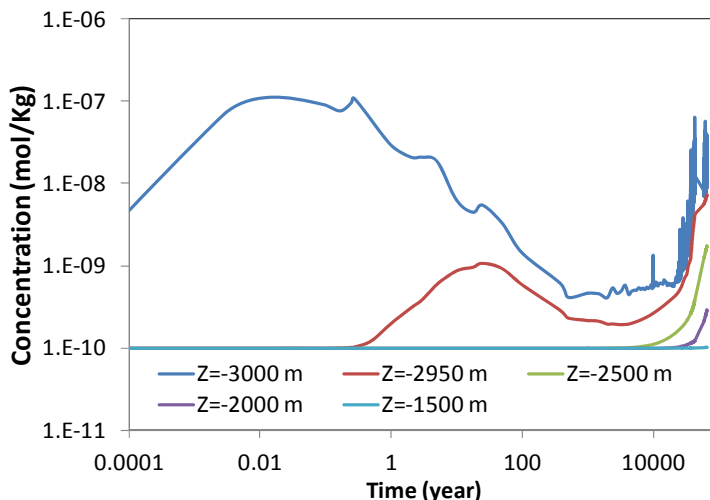


Figure 4-18. Uranium concentration in the damaged zone (adjacent to the wellbore) at several depths.

4.2.3 THC Modeling Conclusions

THC model was developed to simulate a hypothetical case for a deep borehole repository, with radionuclide release at the very beginning and hypothetical chemical conditions. The chemical part in THC model is simplified such that we can focus on evaluating advective versus diffusive fluxes over the course of heat releasing in a deep borehole repository. Because of the thermal pressurization, pressure buildup around the waste package drives fluid upward along the damaged zone, which might carry the radionuclide upwards and jeopardize the safety of deep borehole repository. The THC model showed that migration of radionuclide by advective flux is limited to early time (< 100 years) and an area of 50 m around waste package in both vertical and horizontal direction. Migration of radionuclide by diffusive flux becomes important at the later time and carries radionuclide in both vertical and horizontal direction. With current diffusion coefficient, it takes about 20,000 for the radionuclide to reach 1,000 m above the waste package. While current model sheds some light on the transport of radionuclide in a deep borehole repository, further study is needed to investigate how geochemically reducing conditions at depth affect the solubility of radionuclide bearing minerals and the migration of radionuclides.

4.3 THM Modeling

In this section, we described the THM and disturbed zone modeling. The plan was to conduct the THM modeling at multiple scales to be able to model both the large-scale stress evolution and the detailed evolution of the disturbed zone. We first conduct an initial modeling to understand the potential impact of heat releasing waste on the stress evolution and the potential impact on the disturbed zone. This modeling is based on the TH model simulations presented in Section 4.1. An axisymmetric grid that in the THM analysis is extended to anisotropic stress conditions through superposition of thermally induced stress changes on the initial anisotropic stress field. For the disturbed zone modeling, we have developed and implemented both a simple stress-permeability model and a more complex damage model into the TOUGH-FLAC software and tested those against field data from an underground research laboratory. Finally, we are developing full 3D, which enable us to include more detailed representation of some borehole components and steps of construction and post-closure.

4.3.1 General THM modeling approach

The general THM modeling approach adopted is to conduct numerical simulations of THM-induced stress evolution using a large scale model and then based disturbed zone models on previous field observation of disturbed zone and borehole breakouts for estimating the potential disturbed zone permeability changes. A large-scale THM model will be used to calculate temperature, pressure and stress evolution (Figure 4-19).

The ultimate goal is to model steps (shown as steps 1 to 8 in Figure 4-19) from drilling to the long-term behavior and return to ambient conditions.

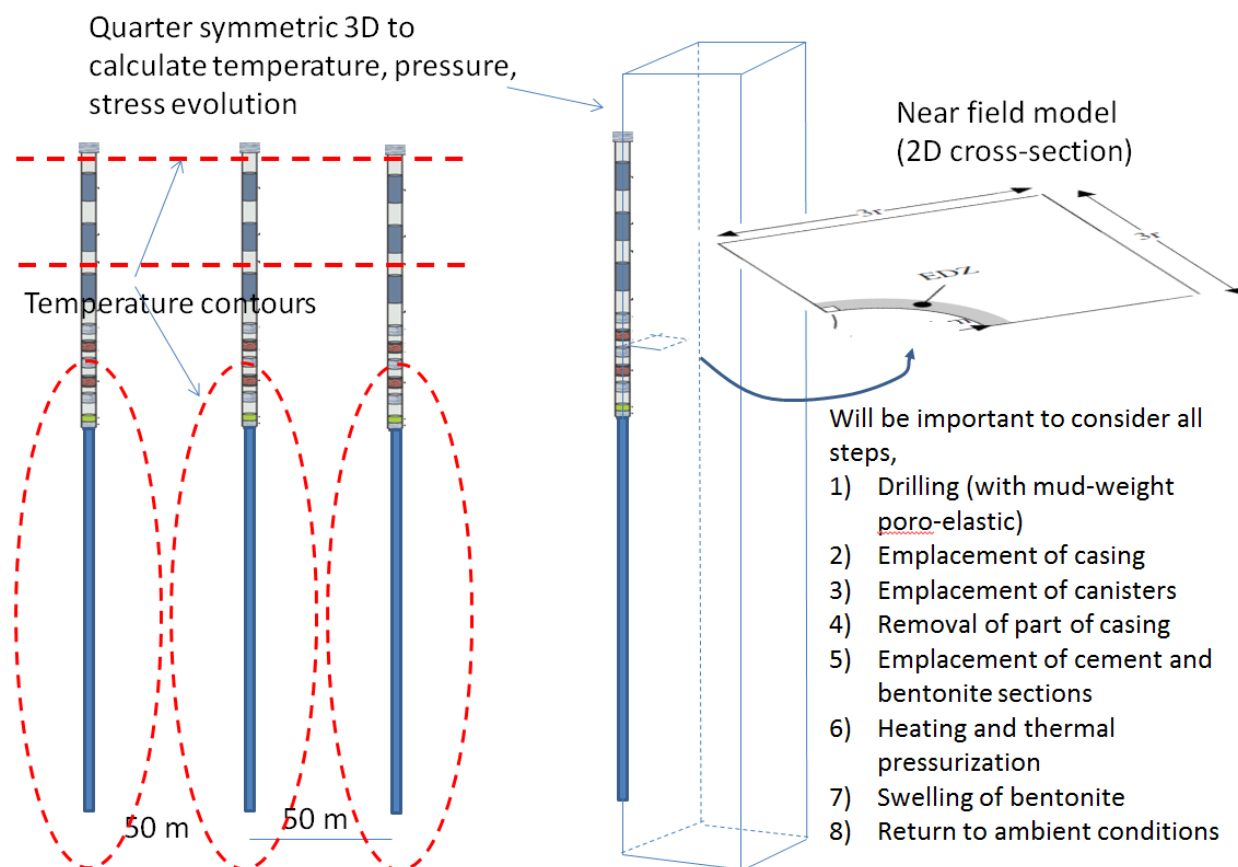


Figure 4-19. Overview of THM modeling approach

The disturbed zone modeling will include calculation of the evolution of the damage and permeability changes over time. A few approaches may be applied with increasing complexity as follows:

- 1) Simple stress-permeability model (mean and deviatoric stress vs. permeability) with in situ calibrated parameters at the Manitoba URL Canada (tight granite)
- 2) Anisotropic damage model with anisotropic crack propagation under tensile and shear stress
- 3) Discrete fracture propagation model (TOUGH-RBSN) 2D cross-section model

The first alternative case involved in situ calibration of simple models for permeability changes with deviatoric (shear) and mean effective stress for competent (intact) granite. Permeability increases of up to four orders of magnitude were measured during excavation tunnels at the Manitoba URL, some of which were stress induced and some of which were induced by excavation operation. The second alternative would include a constitutive model for anisotropic damage, which involves a mechanistic coupling between stress-induced anisotropic damage and anisotropic permeability changes. The third alternative involves modeling of discrete propagation and damage using TOUGH-RBSN in a 2D cross-section. Using this model, we will be able to study and address issues related to the size of the hole, in relation to observations of spalling strength at tunnels and laboratory experiments.

One idea is to extract stress, temperature and pressure evolutions from the large-scale 3D model, and apply it as apply time-dependent stress boundaries an internal temperature and pressure conditions on the 2D disturbed zone model. To date we have focused our work on alternatives 1 and 2 for disturbed zone modeling, as these can be implemented and used directly in the continuum modeling with TOUGH-FLAC.

4.3.2 Estimates of in situ stress

The three dimensional in situ stress field is a critical input for modeling the stress evolution and impact on the disturbed zone. At a real deep borehole disposal site, estimation of the stress field will be a very important site characterization activity. Here, for this study of a generic deep borehole repository, we estimate a reasonable stress range based on literature data. For example, Figure 4-20 shows vertical profiles of vertical stress (S_v) and lateral stress coefficient $k = S_h/S_v$ where S_h is horizontal stress. Figure 4-20a shows that stress would be around 80 MPa at 3 km depth, and if extrapolating to 5 km, stress would be around 100 MPa. It is also shown that at 3 km the horizontal stress might be as high as the vertical or as low as 1/3 of the vertical, creating a differential stress that could have consequences on borehole stability. Figure 4-21 shows estimates of stresses down to about 5 km at two deep boreholes in Sweden and Germany indicating high differential horizontal stress with maximum as horizontal stress as high as 200 MPa at 5 km depth (Lund and Zoback, 1999; Brudy et al. 1997). Considering stress concentration around a well, maximum compressive stresses could then easily exceed the compressive strength and borehole breakout may occur. In fact, the stress estimates made at depth in these deep boreholes are partly based on observed borehole breakout and drilling induced tensile fracture.

Figures 4-20 and 4-21 gives us estimates as to what range of initial stresses we could apply to the coupled THM models. It is reasonable to assume a vertical stress gradient of 27 MPa per km. A maximum horizontal stress equal to the vertical is also reasonable, although it could be lower or higher. The minimum horizontal stress could be as low as 1/3 of the vertical according to Figure 4-20. However, such a big difference between maximum and minimum stress would in this case lead to unstable conditions if considering fictional limits and a coefficient of friction of 0.6. The field measurements at the deep borehole in Gravberg-1 and KTB shown in Figure 4-21, indicate a minimum compressive horizontal stress about 0.6 to 0.8. Our first approach will be to assume a minimum horizontal stress a factor 0.7 of the vertical, but is subsequently varied in a parameter study.

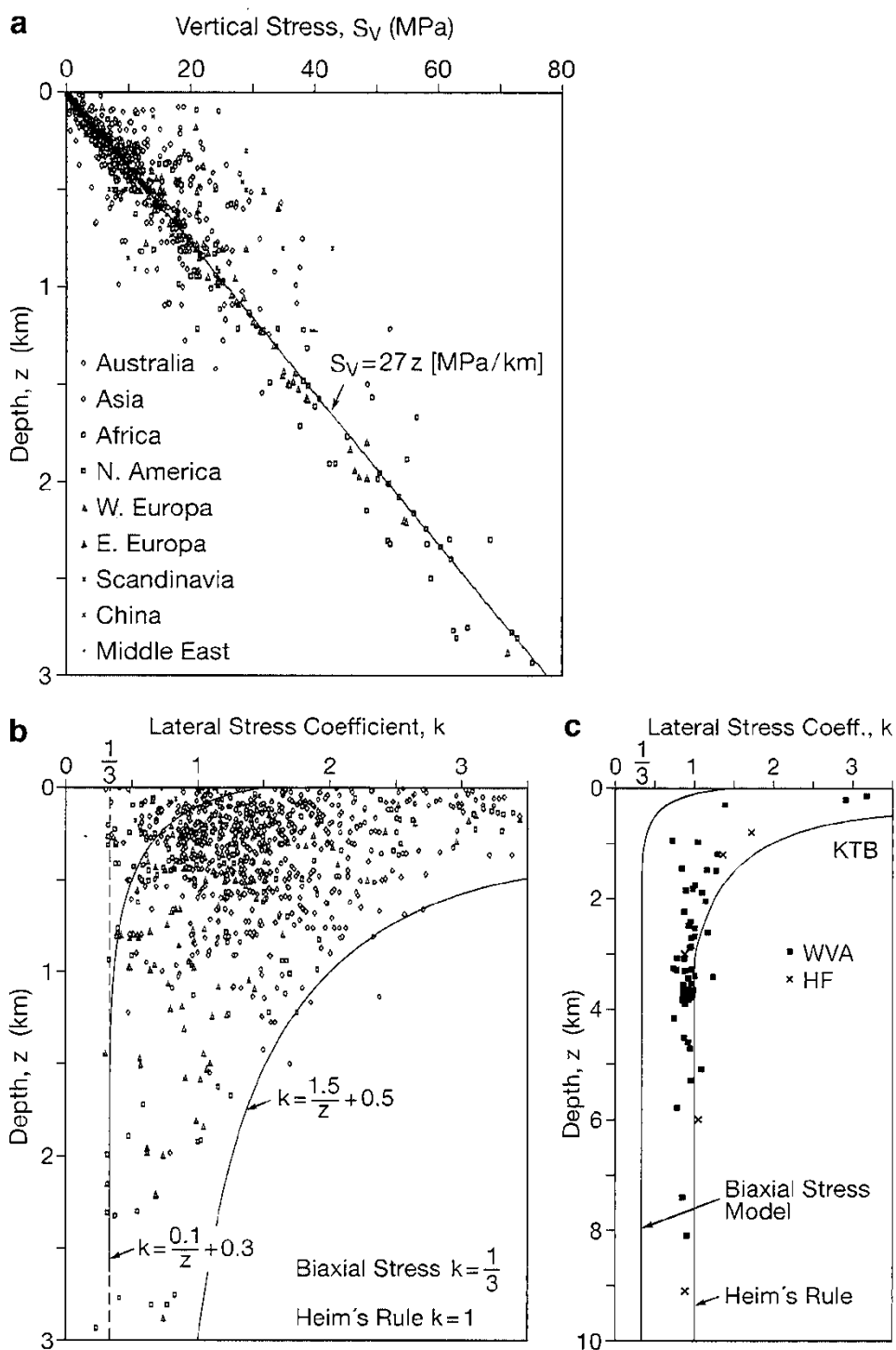
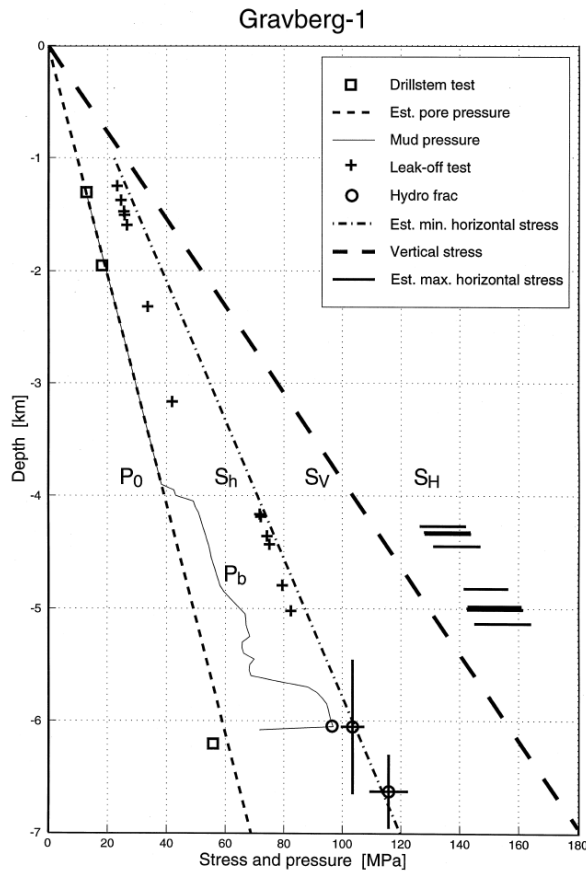
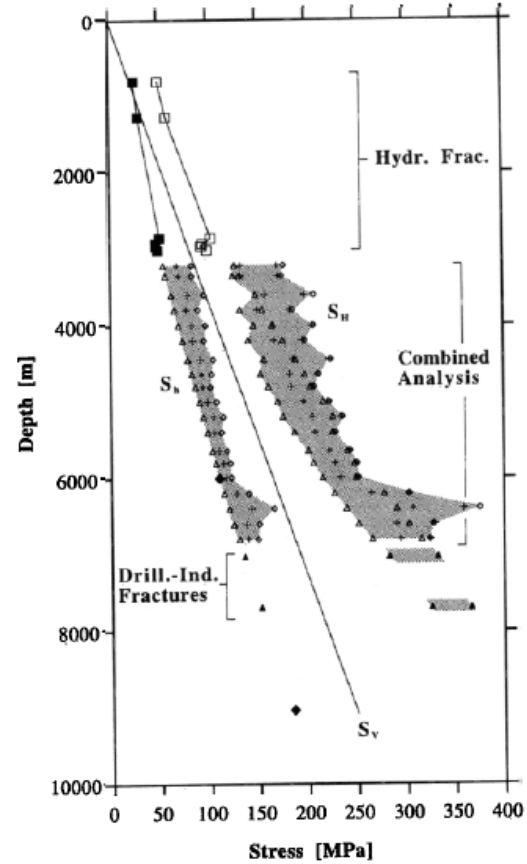


Figure 4-20. Global compilation of (a) vertical stress and (b, c) lateral stress coefficients, k , down to a depth of 3 km in the Earth's crust according to Brown and Hoek (1978) (adapted from Zang and Stephansson, 2010)



(a)



(b)

Figure 4-21. Published stress estimates at (a) Gravberg-1 deep borehole in Sweden (Lund and Zoback, 1999), and at (b) KTB borehole Germany (Brudy et al., 1997).

4.3.3 Stress evolution modeling using TH modeling result

Here we use a rational approach for evaluating the stress evolution due to coupled THM processes occurring in the rock mass surrounding the heat-releasing borehole. The approach is based on the application of simple analytical solutions thermo-elasticity and poro-elasticity and stress superposition.

4.3.3.1 Approach for stress evolution modeling

The approach was developed based on the experience with previous modeling of coupled THM processes around a repository related to emplacement in horizontal tunnels at 500 m depth (Rutqvist et al., 2009a and Rutqvist et al., 2014). Those model simulations were also conducted using a symmetric model of vertical column going all the way up to the ground surface. Examining the results in Rutqvist et al., (2009a) it can be concluded that the horizontal stress evolution is well correlated with the average temperature and pressure changes at a given elevation. Examining the results in Rutqvist et al., (2014), where thermal pressurization was rampant, the modeling shows that the horizontal stress evolution is proportional to the pressure changes induced by the thermal pressurization. The vertical stress, on the other hand, was always unchanged and equal to the initial lithostatic stress, except very close the wall of the horizontal emplacement tunnel.

In the TH simulations presented in Section 4.1, the temperature and pressure increases at different rates in different points and temperature near the borehole have two peaks. For example, in Figure 4-3(right), there is an initial temperature peak after only 10 years within the vertical borehole, whereas at 10 to 100 m from the borehole, the temperature peaks after 20,000 to 30,000 years. The initial temperature peak at 10 years will result in local tangential stress increase at the borehole wall, whereas additional and strong stress changes occur due to large scale thermal stressing at the second peak around 20,000 to 30,000 years. The second source of THM-induced stress changes are poro-elastic stress due to thermal pressurization. The result of the TH simulation in Figure 4-5 shows the pressure due to thermal pressurization increases uniformly at the 4 km depth, from the borehole and to the outer boundary located 100 m from the borehole. The pressure peaks at about 2000 years, which is earlier than the thermal peak.

Because the vertical stress is approximately constant, we can calculate stress changes considering simplified uniaxial conditions. The changes in horizontal stress, $\Delta\sigma_h$, due to poro-elastic stress with a uniform pressure change, ΔP , is frequently used in reservoir engineering according to the following equation (Rutqvist, 2012):

$$\Delta\sigma_h = \alpha \frac{1-2\nu}{1-\nu} \Delta P \quad (4.2)$$

where α is Biot's constant and ν is Poisson's ratio. Similarly, for a uniform temperature change, ΔT , the horizontal stress change may be estimated as follows:

$$\Delta\sigma_h = \left(\frac{1-2\nu}{1-\nu} \right) K 3\alpha_T \Delta T \quad (4.3)$$

where K is bulk modulus and α_T is coefficient of linear thermal expansion.

Equations (4.2) and (4.3) provide a good estimate of horizontal stress increase at a specific depth caused by uniform pressure and temperature changes occurring at that depth. Assuming an elastic medium, we can calculate the total stress by superimposing these stress changes on the initial stress, which could be anisotropic. Thus, this is a rational way of using the axisymmetric TH modeling results to estimate stress changes even in the case of an anisotropic in situ stress field. Moreover, assuming an elastic medium, we can also translate how such stress changes in rock mass at a certain depth translates into tangential stress concentrations around the borehole. There is a simple expression for maximum tangential stress around the borehole (Rutqvist et al., 2000)

$$\sigma_{\theta\max} = 3S_{H\max} - S_{h\min} - P_{bh} \quad (4.4)$$

P_{bh} is the internal pressure against the borehole wall. Similarly, the minimum tangential stress around the periphery of the borehole can be calculated as

$$\sigma_{\theta\min} = 3S_{h\min} - S_{H\max} - P_{bh} \quad (4.5)$$

Having the temperature and pressure changes calculated in the TH axisymmetric model, we can use Equations (4.2) through (4.5) to estimate stress changes at different depths, and their impact on hoop stresses around the well. Some of the early time hoop stresses caused by the first thermal peak are not considered in this simplification. Such early time additional thermal hoop stress will exist when there is a certain thermal gradient around the borehole. This thermal gradient diminishes with time and during the second peak around 20,000 years the temperature is horizontally uniform at a given depth.

4.3.3.2 Thermal load case and basic material parameters

The TH modeling showed that in the case of 2600 W/canister the temperature and pressure changes are about 4 times higher compared to the 580 W/canister option. In the stress modeling we selected to work with the high temperature case, i.e. 2600 W/canister, as this would be expected a worst case giving rise to much stronger geomechanical responses. The mechanical material parameters needed for the stress analysis are the mechanical elastic properties, thermal expansion coefficient and Biot's constant. Here we adopt properties from the Manitoba URL in Canada that are also used for the analysis of disturbed zone changes. This is competent granite with a Young's modulus of 60 GPa and Poisson's ratio of 0.2, corresponding to a bulk modulus of 30 GPa. Linear thermal expansion coefficient is set to $1 \times 10^{-5} \text{ }^\circ\text{C}^{-1}$, a common value for granite, whereas in a base-case we set Biot's constant to 1.0.

4.3.3.3 Stress evolution for a base-case of $S_{Hmax} = S_v$ and $S_{Hmin} = 0.7S_v$

Figure 4-22 shows the calculated evolution of total and effective stresses at 4 km depth. Initial vertical stress and maximum horizontal stresses are both equal to the lithostatic stress of $S_{Hmax} = S_v = 109 \text{ MPa}$ (due to the weight of the overburden), whereas the initial minimum horizontal stress is $S_{Hmin} = 0.7 \times 109 = 76 \text{ MPa}$. Both horizontal stresses increases by an equal amount starting from about 10 years, stays high from about 1000 years to peak at about 20,000 years (red and blue lines in Figure 4-22a). The effective horizontal stresses also increases with time and peaks at 20,000 years (red and blue lines in Figure 4-22b). The total vertical stress stays constant at lithostatic stress as a result of the free moving ground surface (green line in Figure 4-22a), whereas the vertical effective stress temporarily decreases with a minimum at about 2000 years (green line in Figure 4-22b). These changes in a stress field imply that the minimum principal stress will shift from initially being horizontal to becoming vertical after about 300 years. Figures 4-23 and 4-24 present the stress field evolution at 3 and 1.5 km, respectively General stress evolutions at 3 and 1.5 km depth are similar to that at 4 km depth (Figure 4-22), but the stress magnitudes are smaller.

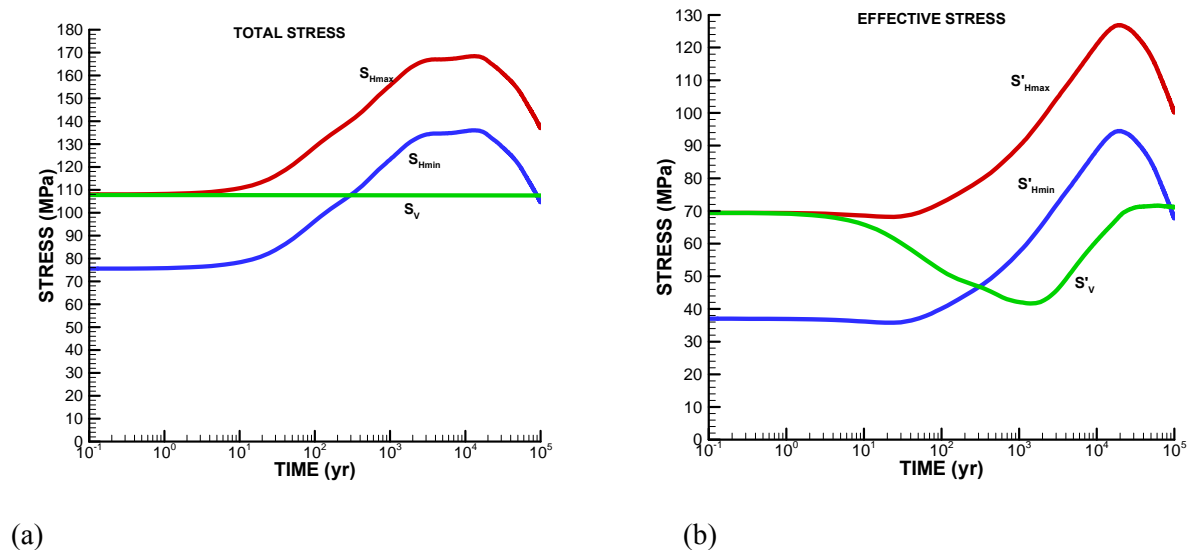


Figure 4-22. Evolution of (a) total stress and (b) effective stress at 4 km depth.

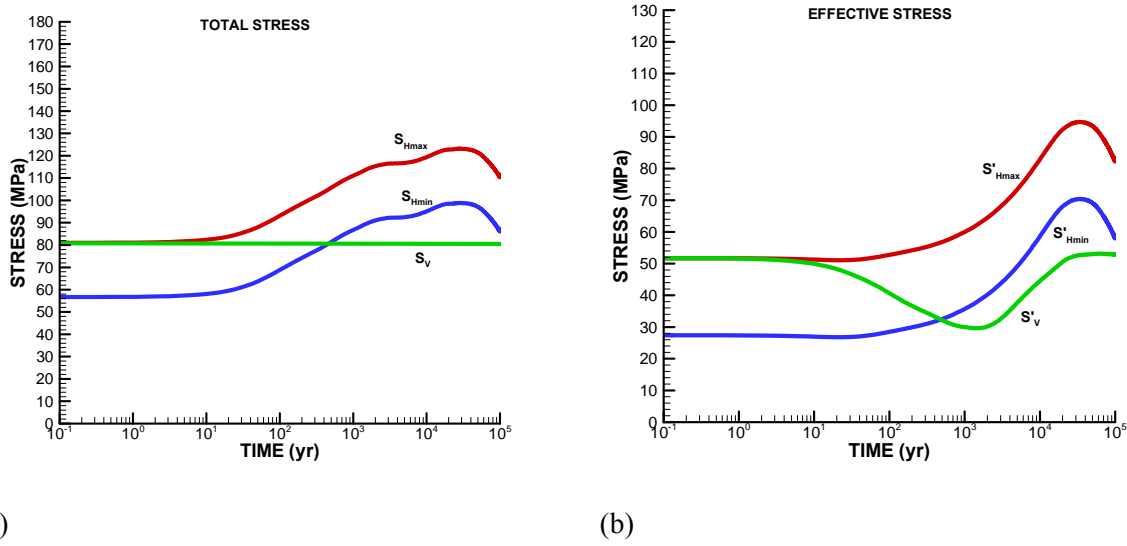


Figure 4-23. Evolution of (a) total stress and (b) effective stress at 3 km depth.

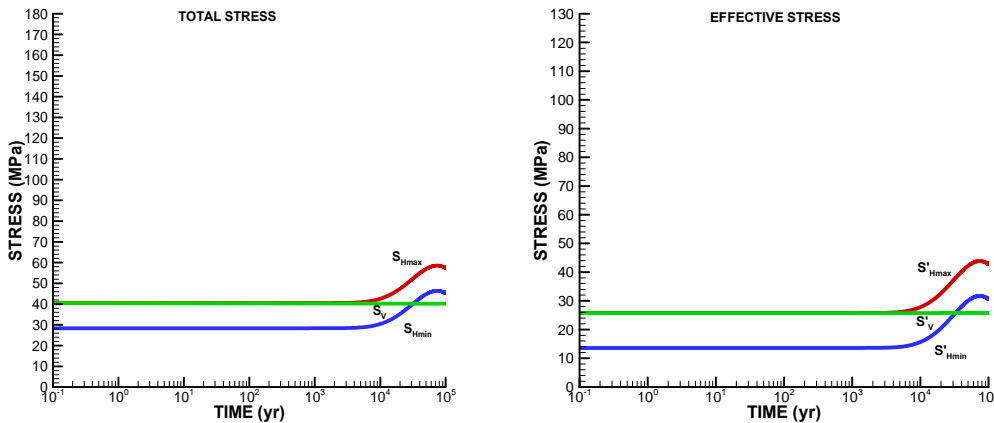


Figure 4-24. Evolution of (a) total stress and (b) effective stress at 1.5 km depth.

In Figure 4-25, the stress paths (σ'_{Hmax} vs σ'_{hmin}), (σ'_{Hmax} vs σ'_v) and (σ'_v vs σ'_{hmin}) are shown for a depth of 4 km. Included in the figure is also the frictional strength limit of the rock mass when assuming a coefficient of friction of 0.6 and zero cohesion. This frictional strength limit could represent the condition when optimally oriented faults or fractures could be reactivated in shear. Generally, Figure 4-25a shows that the rock mass becomes more stable with time in terms of the stress path for horizontal stresses (σ'_{Hmax} vs σ'_{hmin}). This means that faults would not likely be reactivated in strike-slip mode. Figure 4.25b shows that the rock mass becomes less stable in terms of the stress path for maximum horizontal versus vertical stress (σ'_{Hmax} vs σ'_v) over the first few 1000 years when the stress moves towards the frictional strength limit. Figure 4-25c also shows a stable stress path in terms of σ'_v vs σ'_{hmin} . Thus, in this particular case, for the assumed initial stress field ($S_{Hmax} = S_v$, and $S_{hmin} = 0.7S_v$), the frictional strength limit is never reached and therefore faults and fractures would not be reactivated.

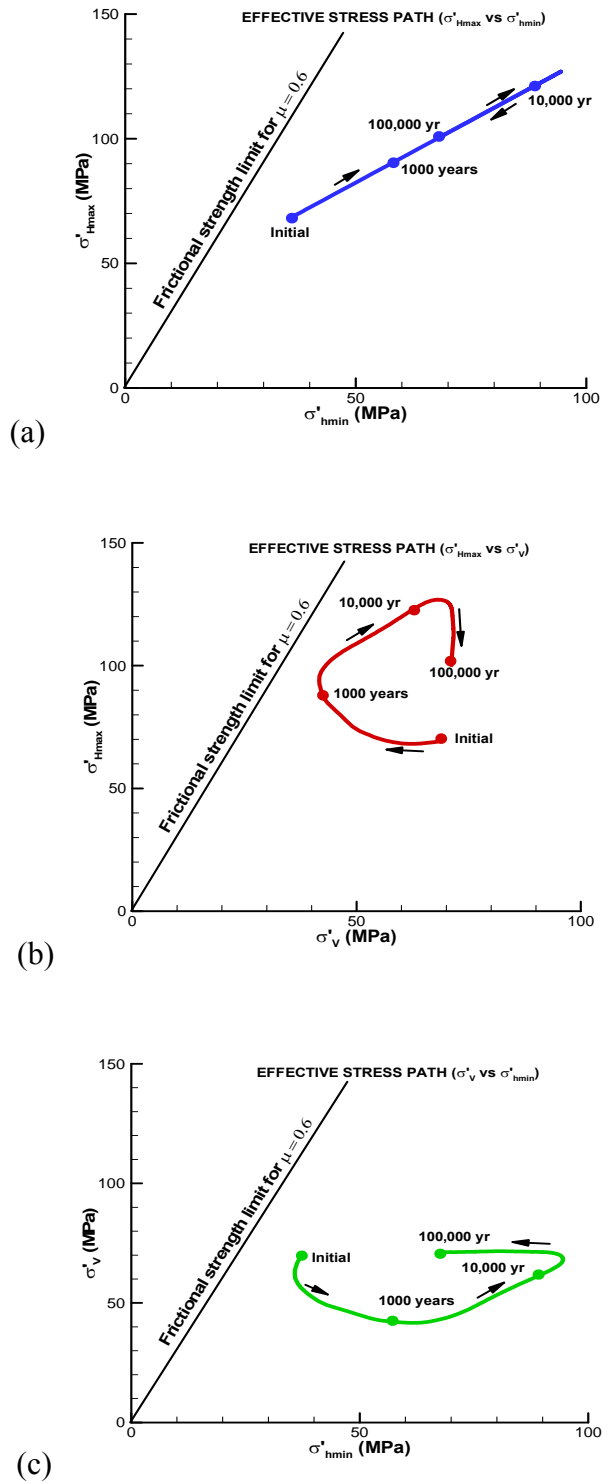


Figure 4-25. Effective stress paths in terms of (a) σ'_{Hmax} vs σ'_{hmin} , (b) σ'_{Hmax} vs σ'_v , and (c) σ'_v vs σ'_{hmin} at 4 km depth.

Figure 4-26 presents the evolution of tangential stress concentration around the borehole at 4 km depth calculated with Equations (4.4) and (4.5). The stress concentration calculated in this case is related to changes in horizontal far field stresses shown in Figure 4-22. As mentioned, we are not including potential impact of early time near-borehole thermal gradient that could cause some additional stress changes during the first ten to 100 years. Figure 4-26a shows the total tangential stress evolution; the red line represents the point where the maximum horizontal stress results in the highest tangential stress concentration around the well, whereas the blue line represents to lowest tangential stress concentration. The green line is the fluid pressure, which also will provide a confining total stress on the borehole wall, which will be the radial compressive stress at the borehole wall. The potential for failure will depend on the effective stress which is shown in Figure 4-26b. In this case, the fluid pressure in rock adjacent to the borehole is equivalent to the pressure within the borehole. Therefore, the radial effective stress will be essentially zero and we can consider uniaxial compressive strength. The uniaxial compressive strength for granite may be in the range of 100 to 250 MPa. The initial tangential effective stress is already as high as 170 MPa, which very likely could lead to compressive failure or so-called spalling failure leading to borehole breakout. The tangential effective stress then increases to as much as 300 MPa, which would surely lead to additional damage that may even extend around the entire borehole perimeter. This would occur thousands of years after emplacement as the maximum stress occurs after 20,000 years.

At 3 km depth (Figure 4-27), the compressive tangential stresses are also substantial and increase to peak at over 200 MPa after 20,000 years. At 1500 m depth (Figure 4-28), the stresses are not as high initially (max 60 MPa) and the stress changes induced by temperature and pressure changes are much lower. On the other hand, if we are in the sedimentary rock section, the compressive strength could also be much lower and borehole break out could therefore occur for tangential stresses on the order of 60 MPa. One difference at the relatively shallow depth of 1500 m is that there are no significant pressure changes and temperature changes are much smaller. Thus, at 1500 m most of the disturbed zone changes and borehole breakout may occur during the construction, whereas relatively small changes could occur during the post-closure period.

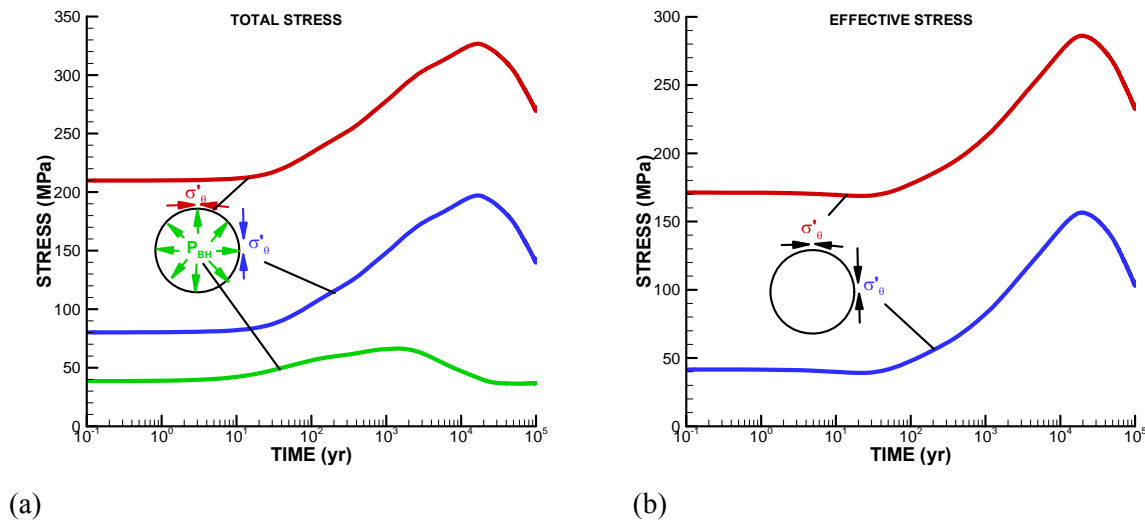


Figure 4-26. Evolution of maximum and minimum (a) total and (b) effective tangential stresses around the borehole at 4 km depth.

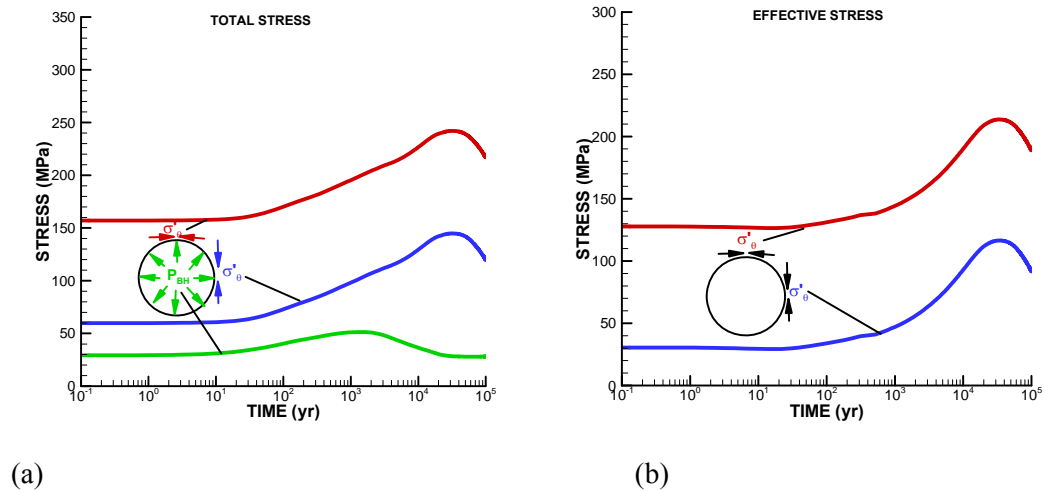


Figure 4-27. Evolution of maximum and minimum (a) total and (b) effective tangential stresses around the borehole at 3 km depth.

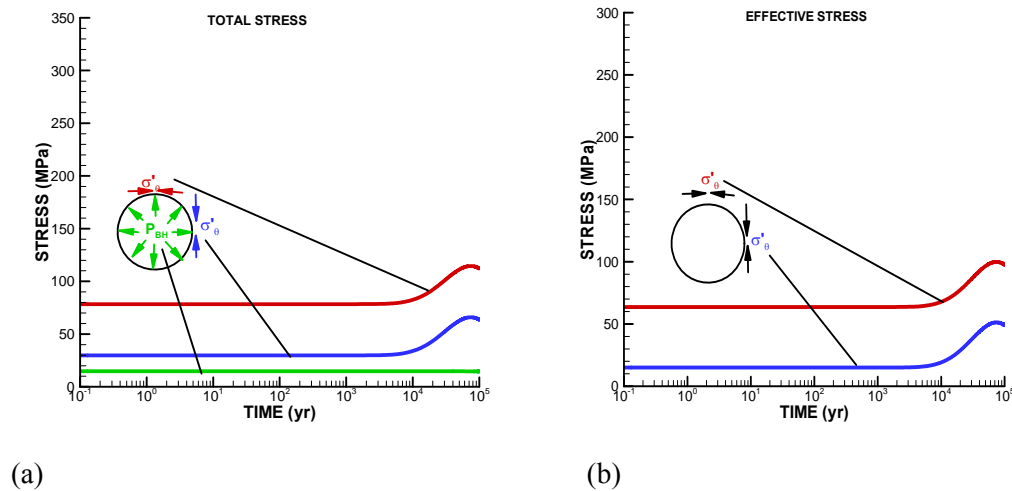


Figure 4-28. Evolution of maximum and minimum (a) total and (b) effective tangential stresses around the borehole at 1.5 km depth.

4.3.3.4. Case 1 of critically-stressed crust with $SH_{max} = Sv$ and $Sh_{min} = 0.58Sv$

One common hypothesis is that the brittle earth's crust is critically stressed for shear instability, including the deep crystalline basin, which has often been associated with induced seismicity during deep underground fluid injection. If assuming a low $Sh_{min} = 0.58 \times Sv$, while keeping $SH_{max} = Sv$, the rock would initially be on the verge of shear slip in optimally oriented faults and fractures. Figure 4-29 shows that the initial stress field for this case is indeed on the fictional strength limit for reactivation in strike-slip (Figure 4-29a) or as normal faulting (Figure 4-29c). However, the stress path during post-closure related to those stress-pair parameters (Figure 4-29a and c) moves away from this critical stress condition, mainly because σ'_{hmin} increases. Thus, also in this case, for the assumed initial stress field on the verge of shear failure ($S_{Hmax} = Sv$, and $S_{hmin} = 0.58Sv$), the frictional strength limit is never exceeded and therefore faults and fractures would not be reactivated.

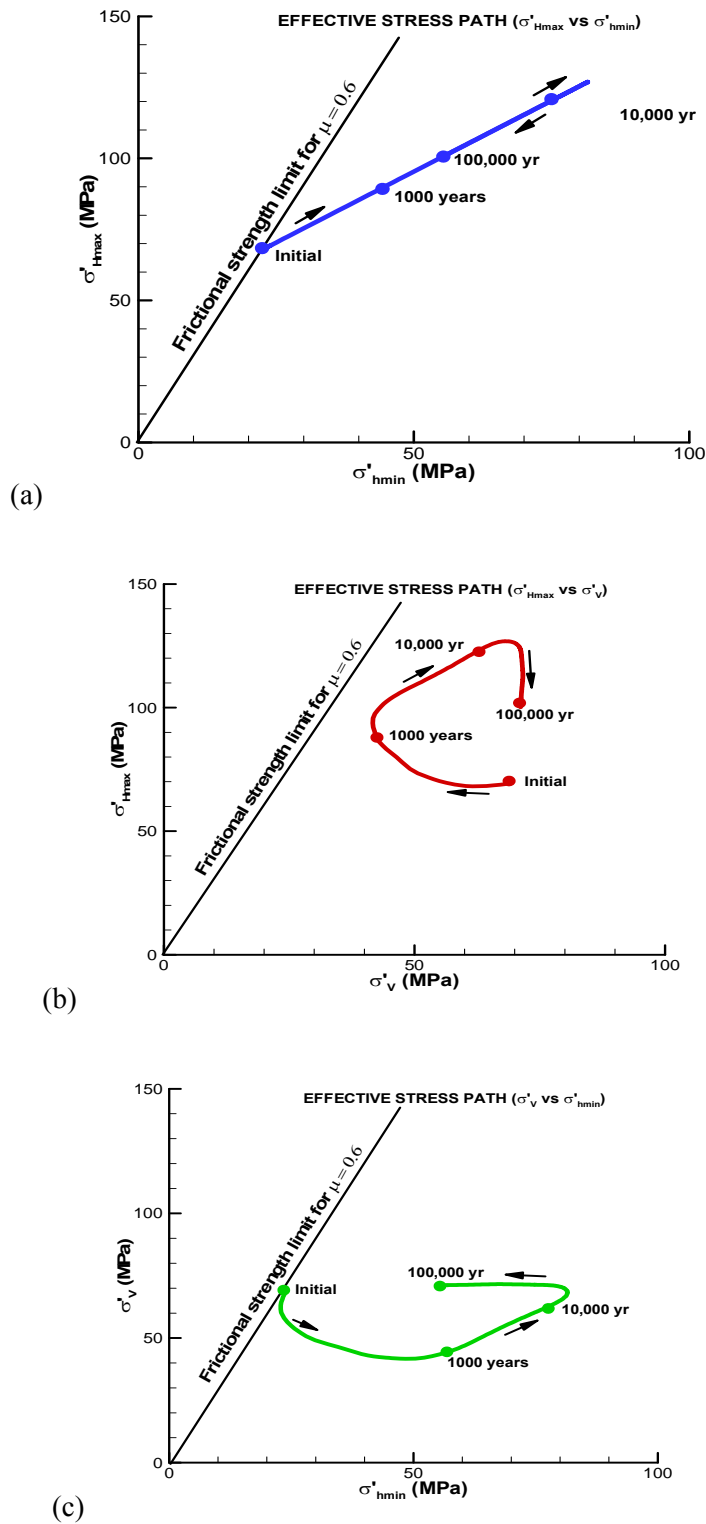


Figure 4-29. Effective stress paths in terms of (a) σ'_{Hmax} vs σ'_{hmin} , (b) σ'_{Hmax} vs σ'_v , and (c) σ'_v vs σ'_{hmin} at 4 km depth for the case of a critically stressed crust.

For the conditions of $S_{hmin} = 0.58 \times S_v$, while keeping $S_{Hmax} = S_v$, the difference between horizontal principal stress are larger ($S_{Hmax} = 0.58 \times S_{hmin}$), and this creates larger stress concentrations around the borehole according to Equation (4.4). For example, at 4 km depth the stresses would in theory increase to almost 300 MPa at the location of the highest tangential stress around the borehole (red line in Figure 4.30a). At the location of the lowest tangential stress, the effective tangential stress would initially be close to zero, which means that tensile failure is prevented by the tensile strength of the rock (Figure 4.30, blue lines). Generally, as expected if the initial horizontal stress is more anisotropic, the breakout pattern around the borehole would also be expected to be more anisotropic.

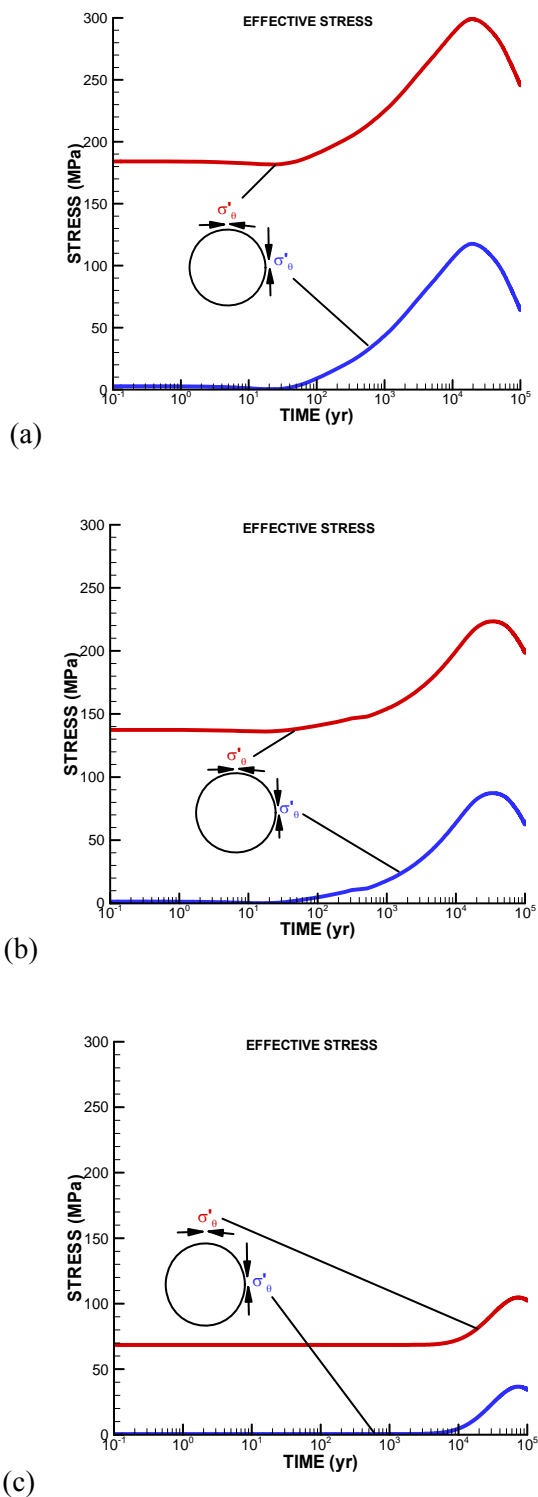


Figure 4-30. Evolution of maximum and minimum effective tangential stresses around the borehole at (a) 4 km, (b) 3 km, and (c) 1.5 km depth.

4.3.3.5. Case 2 of critically-stressed crust with $S_{Hmax} = 1.3S_v$ and $S_{hmin} = 0.68S_v$

From Figure 4-21, we can observe that horizontal stresses in excess of vertical have been estimated from the deep borehole investigations at Gravberg and KTB. Based on observations in Figure 4-21, we try one case with $S_{Hmax} = 1.3 \times S_v$. For such a case, critical stressed condition is achieved if $S_{hmin} = 0.66 \times S_v$, which is also consistent with the stress estimate at Gravberg and KTB. The results in Figure 4-31 for this case show that the stress field is initially critically stressed related to σ'_{Hmax} vs σ'_{hmin} , i.e. critically stressed for imminent strike-slip fault movements. However, again, because both σ'_{Hmax} and σ'_{HMIN} increases during post-closure, the stress field moves away from strike-slip fault slip conditions. Similarly, related to σ'_v vs σ'_{hmin} (Figure 4-31c), the stress field is initially close to being critically stressed for shear. Later, as σ'_{hmin} increases with time, the stress field moves away from failure. This implies that the rock mass becomes more stable in terms of potential for inducing normal fault slip on steeply dipping faults and fractures. However, for σ'_{Hmax} vs σ'_v (Figure 4-31c), the shear stress could exceed the frictional strength limit for an optimally oriented fault or fracture after about 1000 years. This would activation on shallowly dipping faults or fractures, i.e. signifying a reverse fault activation. Thus, in this case, for the assumed initial stress field on the verge of shear failure and with relatively high horizontal stress ($S_{Hmax} = 1.3S_v$, and $S_{hmin} = 0.68S_v$), there is some possibility for exceeding the frictional strength and reactivating faults and fractures, and this would be most likely after a few thousand years.

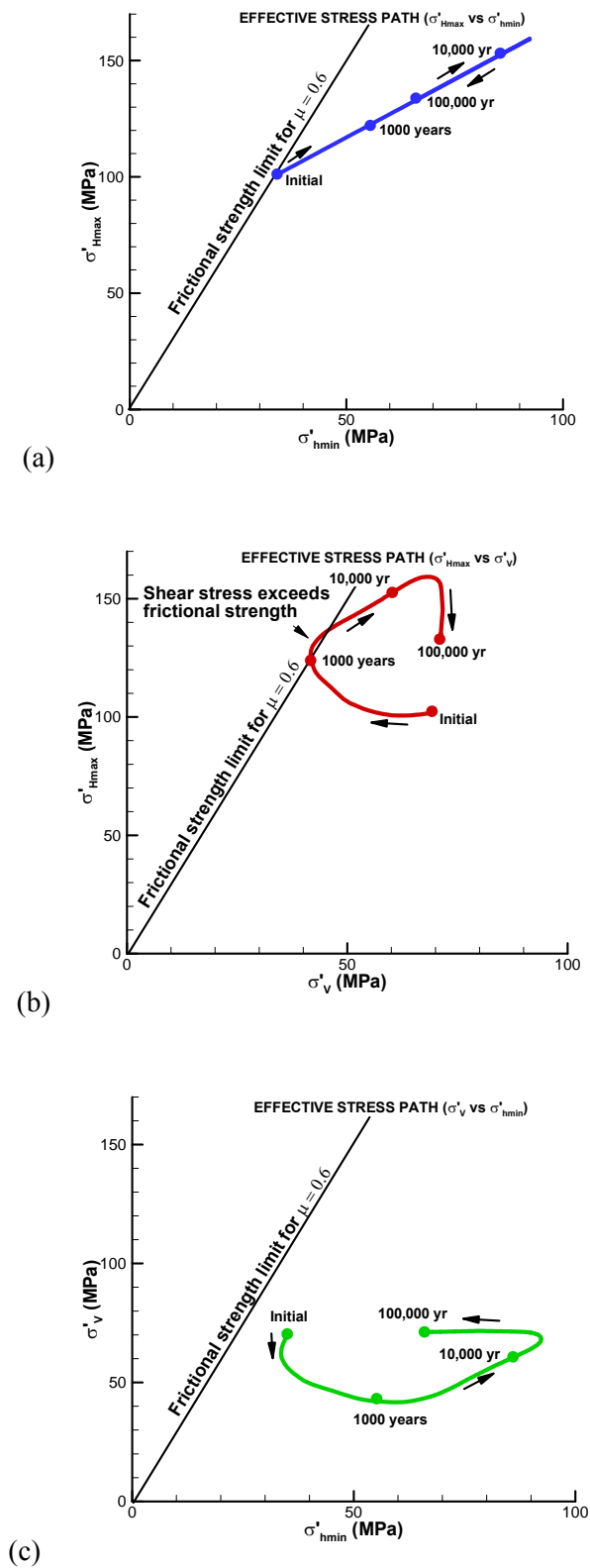


Figure 4-31. Effective stress paths in terms of (a) σ'_{Hmax} vs σ'_{hmin} , (b) σ'_{Hmax} vs σ'_v , and (c) σ'_v vs σ'_{hmin} at 4 km depth for a critically stressed crust.

For the conditions of $S_{Hmax} = 1.3S_v$ while $S_{Hmin} = 0.68S_v$, very high tangential stress concentration are created around the borehole. In the case of 4 km depth, the maximum tangential stress around well is initially 270 MPa and increases to close to 400 MPa at 20,000 years (Figure 4-32a). These are obviously unrealistic numbers as the rock would not be able to sustain such high compressive stresses, but instead substantial borehole breakout would likely occur already during drilling and waste emplacement, before the heating for the rock. The tangential stresses are also very high at 3 km depth (Figure 4-32b). Even at 1.5 km, the maximum tangential stress exceeds 100 MPa, which if in the sedimentary rock could lead to extensive damage around the borehole. This is under the conditions that the high anisotropy in the stress field would also be prevalent in the upper sedimentary zone.

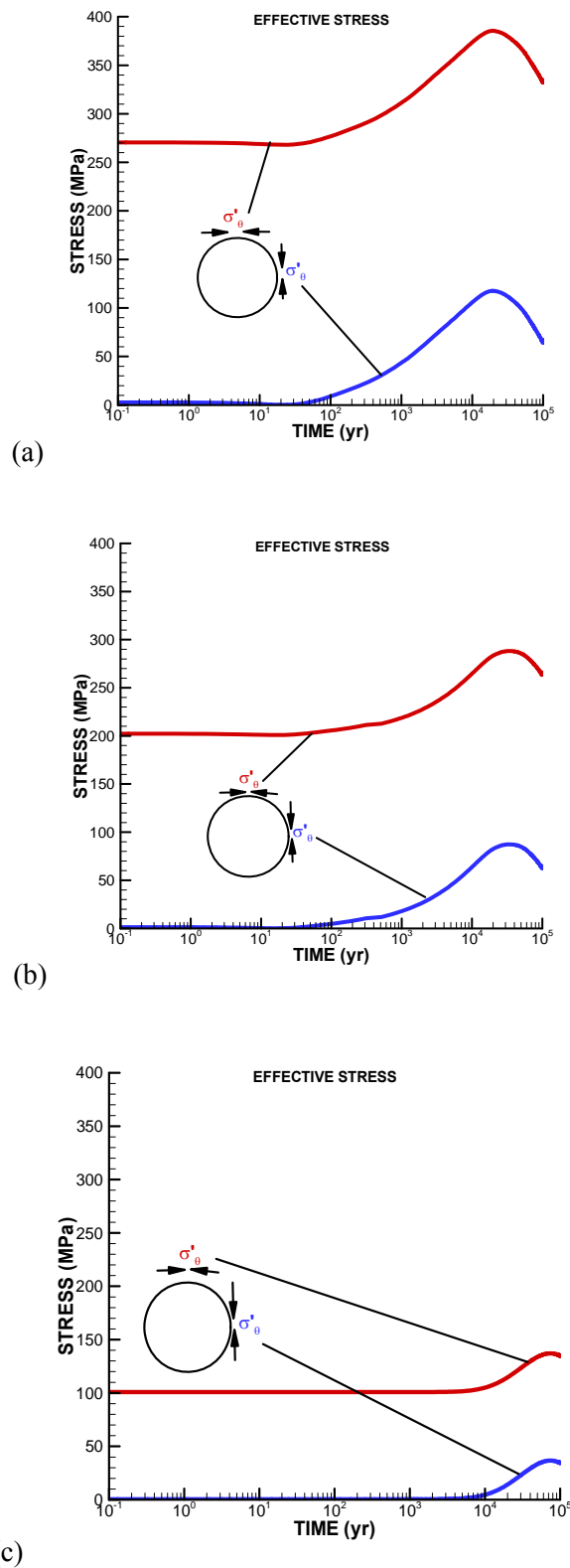


Figure 4-32. Evolution of maximum and minimum effective tangential stresses around the borehole at (a) 4 km, (b) 3 km, and (c) 1.5 km depth.

4.3.3.6. Summary and key findings from stress evolution modeling

The stress evolution modeling conducted in this section is very useful for identifying some of the critical parameters for geomechanics of the system, including the potential for fault activation, induced seismicity, and evolution of the disturbed zone. The importance of the initial stress field cannot be overemphasized, as this will control the potential for induced fault activation and seismicity as well as the degree of damage that will occur around the borehole. The analysis shows that fault activation could only occur on shallowly dipping fault and fractures and this would be a result of an increase in maximum horizontal effective stress while the vertical effective stress is reduced due to fluid pressurization. In particular, the reduction in vertical effective stress due to fluid pressurization is main processes that could lead to a general destabilization of the rock mass. The general increase in minimum horizontal stress due to thermal and poro-elastic stress will have a stabilizing effect on the rock mass with regard to the possibility of fault activation in steeply dipping faults and fractures in strike-slip or normal fault mode. The stress concentration and around the wells and the potential evolution of the disturbed zone and borehole breakouts will be a key issue. What the modeling clearly shows that the biggest stress concentrations would likely occur as much as 20,000 years after emplacement. The compressive stresses at the borehole wall may increase by as much a double during the post-closure period and this could obviously create additional damage around the borehole. In this case, the design of the backfill of the seal zone from 1.5 to 3 km depth will be a delicate issue. In these simulations, we did not consider additional support load by the backfill, such as swelling and mechanical thermal expansion. Here as shown in Figure 4-33 we demonstrate in one simulation the effect poro-elastic and thermal expansion of a concrete plug within the sealing section (at 3 km depth). Using reasonable concrete properties ($E = 35 \text{ MPa}$, $\nu = 0.3$, and $\alpha_T = 1 \times 10^{-5} \text{ }^\circ\text{C}^{-1}$), the peak stress is decreased, but still high. If there is a possibility to design the plug material to have a higher thermal expansion, e.g., a factor of three higher we see from Figure 4-33 dashed lines that the peak compressive stresses could be substantially reduced, but then may be close to tensile stress in some other parts around the borehole periphery. In summary, it will be a delicate design issue to control the disturbed zone and coupled processes modeling is a tool in support of this design.

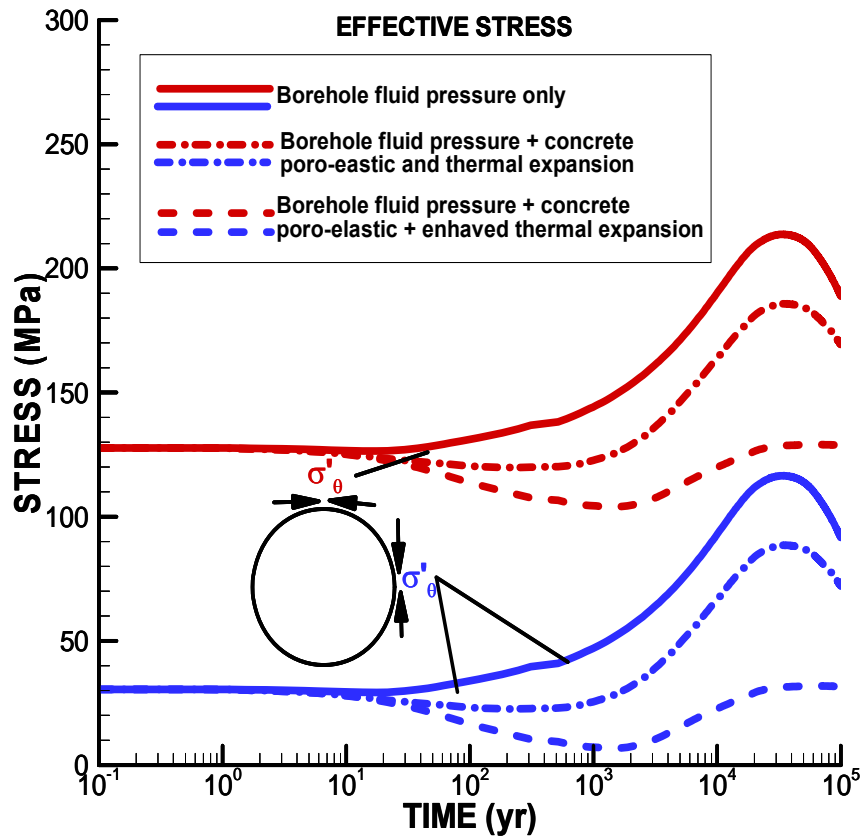


Figure 4-33. Evolution of maximum and minimum effective tangential stresses around the borehole at 3 km depth for the base-case stress field and with consideration of concrete plug poroelastic and thermal expansion with pressure and temperature changes. Enhanced thermal expansion is for a case of a plug having a factor of three higher thermal expansion coefficient.

4.3.4 Simple stress-permeability model and its calibration for disturbed zone modeling

Here we study field data at the Manitoba URL Canada for modeling and calibration of near field rock responses using a simple stress-permeability model. In particular, we are focusing on calibrating a model for potential permeability changes near underground openings. The goal is to develop approaches that can be directly implemented and used in TOUGH-FLAC modeling of disturbed zone. Similar approach was previously used in Rutqvist et al. (2009b) for implementation and testing in a finite element code called ROCMAS. In this section, we use the same approach but implemented and tested for the TOUGH-FLAC simulator. The most important data used here is permeability changes observed at the TSX experiment at the Manitoba URL (Chandler et al. 2002). However, we will also use observations from a well-known mine-by experiment also conducted at the Manitoba URL. Figure 4-34 shows and schematics of the tunnels and the stress state for these two cases. The mine-by experiment induced spalling and macroscopic failure on the top and bottom of the tunnel. The permeability in this zone increased by 6 to 7 orders of magnitude (Rutqvist et al., 2009b). At the TSX, increased macroscopic fracturing was also observed at the top and bottom of the drift, although no substantial slabbing (or fallout) of the rock occurred. At TSX, the

permeability in this zone was evaluated to about $2.5 \cdot 10^{-8}$ m/s (Chandler et al. 2002), which is 5 to 6 orders of magnitude higher than the background intact rock permeability.

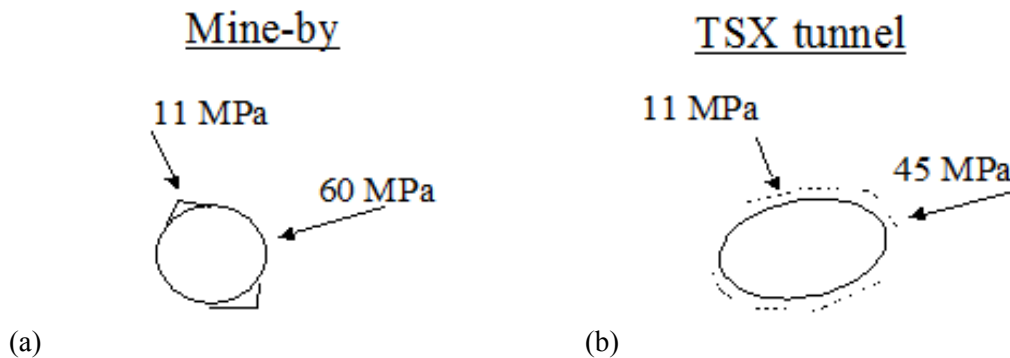


Figure 4.34. Schematic of the failure pattern and stress field associated with two underground openings at the Manitoba URL Canada (a) mine-by experiment and (b) TSX tunnel.

4.3.4.1 Study of macroscopic failure pattern around mine-by experiment

Earlier studies of the mine-by experiment at Manitoba URL has shown that one cannot predict the shape of the macroscopically fractured (spalling) zone using conventional Mohr-Coulomb or Hoek-Brown criteria. Instead, Derek Martin and co-workers (Martin et al., 1999) have developed a spalling criterion as illustrated in Figure 4-35. Figure 4-36 presents our prediction of the shape of the failure zone at the Mine-by experiment using the Mohr-Coulomb criterion. In the first case, we assume conventional Mohr-Coulomb strength parameters, including both cohesion and friction angle. In the second case, we assumed a zero friction angle and a cohesion of 60 MPa to emulate Martin's spalling criterion. That is, spalling would occur when the maximum compressive stress exceeds 120 MPa. The figure shows that the Mohr-Coulomb criterion cannot be used to predict the shape of the spalled zone whereas the simplified spalling criterion predicts the shape reasonably well. Figure 4-37 shows the distribution of maximum and minimum principal stresses. The figure indicates that the extent and shape of the spalled zone can be reasonably well estimated as the zone where the maximum principal stress exceeds 120 MPa.

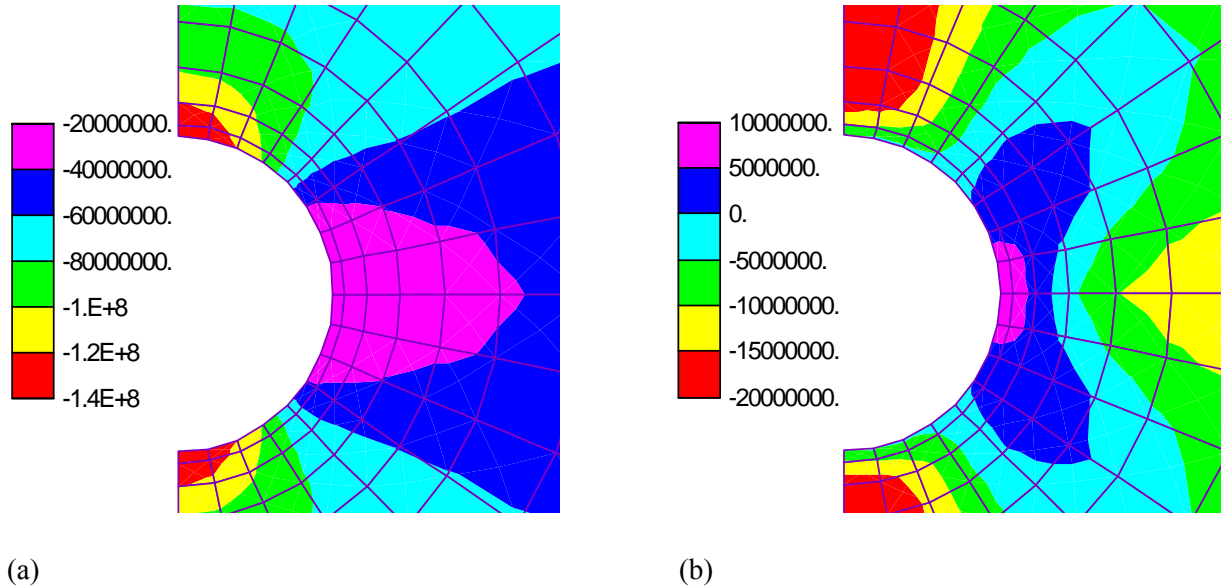


Figure 4-37. Calculated contours of principal stresses (in Pa) at the Mine-by tunnel: (a) Maximum compressive principal stress and (b) minimum compressive principal stress.

4.3.4.2 Study of permeability changes around the TSX tunnel

Figure 4-38 shows permeability as a function of radius for the TSX tunnel, which indicates higher permeability changes at the top of the drift than at the side of the drift. We conducted a stress modeling of the TSX excavation considering the oval shape. In order to find a possible way to correlate the observed permeability changes with stress, we plotted various stresses along profiles extending from the top and springline of the tunnel. We found that the stress profiles extending from the top and springline are completely different. At top of the drift, increased permeability may be correlated with increased deviatoric stress. At the springline of the drift, on the other hand, the increased permeability cannot be explained by change in deviatoric stress but could possibly be explained by reduced mean stress. Another piece of information to consider are the measurements of permeability as a function of deviatoric stress on a core sample, which was used by Souley et al. (2001) for modeling of permeability changes around the TSX. The overall best match model for simulating permeability changes in the rock on both the top and side of the TSX tunnel is obtained using the combined mean stress and deviatoric stress relationship according to

$$k = [k_r + \Delta k_{\max} \exp(\beta_3 \sigma_m)] \cdot \exp(\gamma \Delta \sigma_d) \quad (4.6)$$

Figure 4-39 compares the modeled and measured permeability changes for $\beta_2 = 4 \times 10^{-7}$, $k_r = 1 \times 10^{-21} \text{ m}^2$, $\Delta k_{\max} = 8 \times 10^{-17}$, $\gamma = 3 \times 10^{-7}$, and the critical deviatoric stress for onset of shear induced permeability is set to 55 MPa. The agreement is very good. Figure 4-40 presents the resulting relationship between permeability and deviatoric stress. In this relation, the onset of shear dilation at 55 MPa deviatoric stress is at a much lower deviatoric stress value than usually observed at small-scale laboratory experiments. Figure 4-40 presents contours of permeability change around the drift. Figure 4.41a presents the stress induced permeability changes using Equation (4.6). In order to obtain a good match with field observations we added additional damage induced permeability caused by drill and blasting for a zone extending about 0.3 meters all around the drift (Figure 4-41b). This represents an inner damage zone that has been observed at several tunnels at the Manitoba URL.

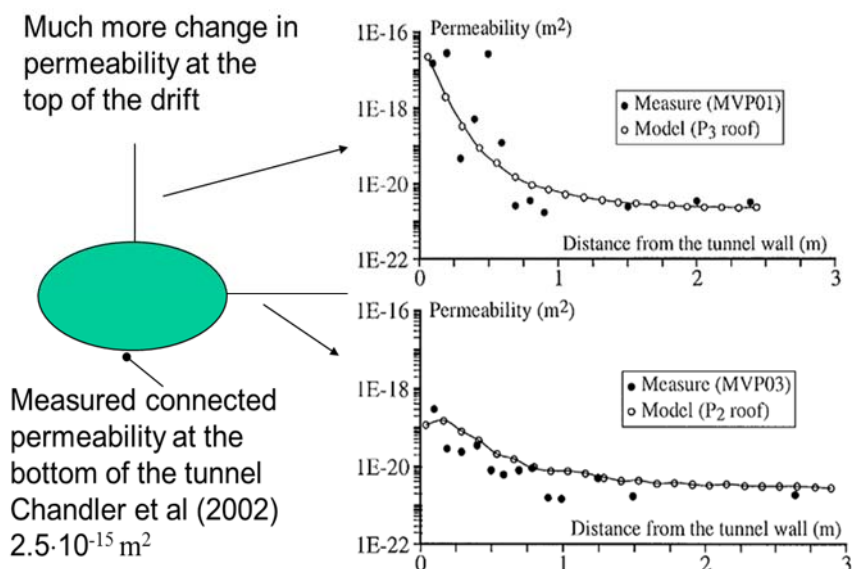


Figure 4-38. Measured and modeled permeability for a borehole extending vertically from the top of the drift and for a borehole extending horizontally from the springline of the tunnel. Graphs of measured and modeled permeability from Souley et al., (2001).

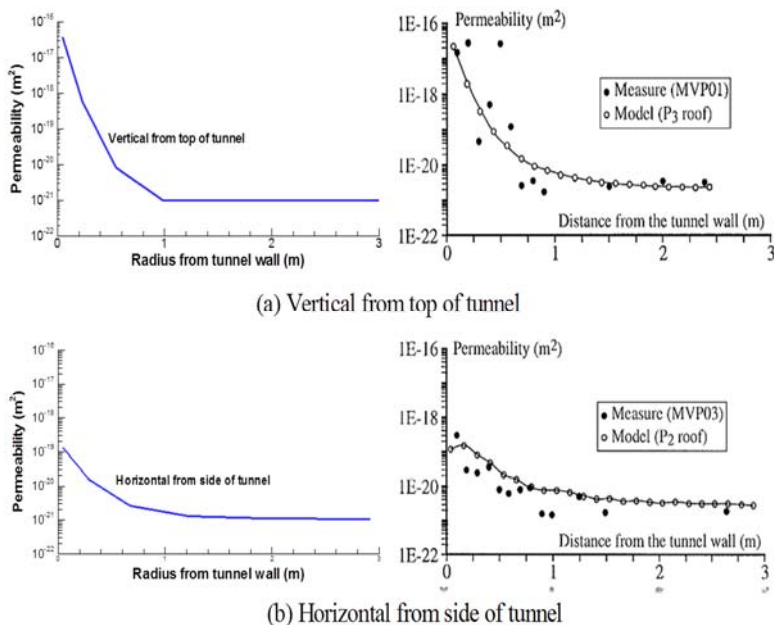


Figure 4-39. Comparison of best-fit simulated and measured results of permeability changes during excavation of the TSX tunnel. Figures of the measured values to the left are taken from Souley et al. (2001).

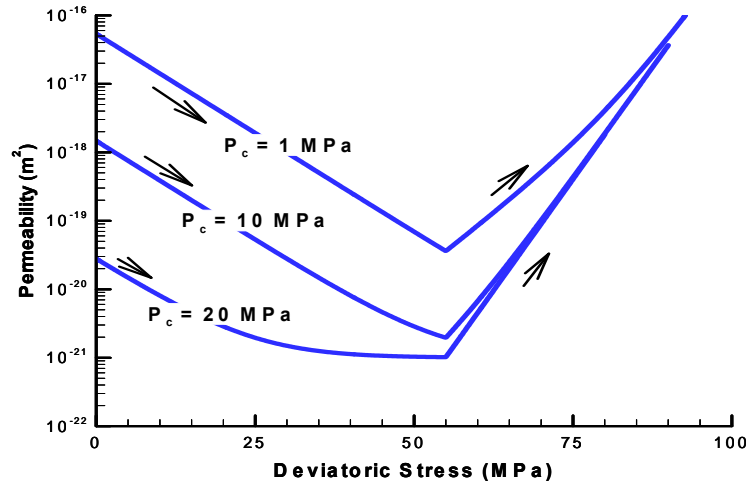


Figure 4-40. Resulting final permeability versus deviatoric stress relation.

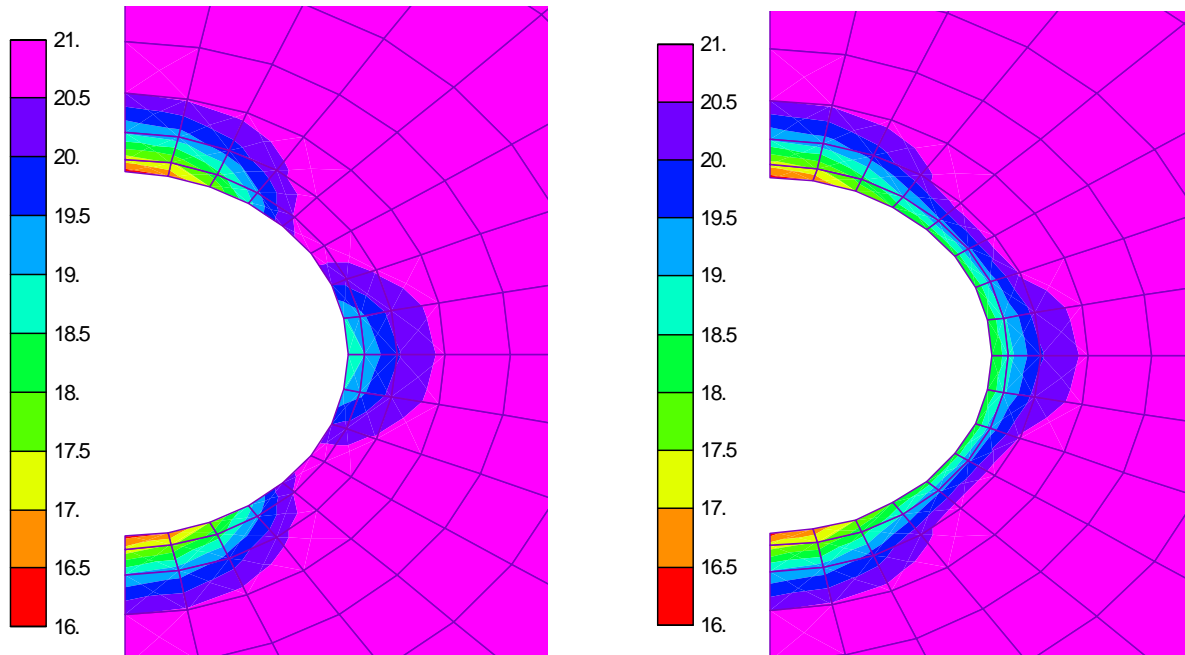


Figure 4-41. Calculated contours of permeability changes during excavation of the TSX tunnel. (a) Stress induced changes. (b) Stress induced + drill and blast effects.

4.3.5 Implementation and testing of a continuum damage model for disturbed zone

This section presents work related to implementation and testing of a continuum damage model intended for the modeling of the disturbed zone around tunnels and boreholes. Continuum damage models have in

the past been applied to wide range of geoenineering applications, including nuclear waste disposals (Tsang et al., 2005) and geothermal systems (Brandl, 2006). The non-uniform distribution of micro-cracking makes it difficult to upscale flaw evolution. Continuum Damage Mechanics (CDM) avoids to model cracks at the micro-scale, as opposed to micro-mechanics. Damage effects are analyzed at the scale of a Representative Elementary Volume Element (REV). In this section, we first present the outline of a continuum damage model developed in research (Xu and Arson, 2014; Xu and Prévost, 2017), then the model is implemented into FLAC3D, and utilized for modeling and calibration of near field rock responses against field experiments at URL.

4.3.5.1 Outline of continuum damage model

Constitutive equations of the skeleton

The proposed anisotropic damage model named Deviatoric Stress Induced Damage (DSID) model is hyper-elastic, i.e. the stress-strain relationship derives from the expression of a thermodynamic potential. The free energy utilized in this model is Gibbs free energy, whose general form is introduced into Continuum Damage Mechanics with the concept of effective stress to account for the reduction of undamaged areas (Chaboche, 1992). Hayakawa and Murakami (1997) have formulated a different expression, which is linearly dependent on damage variable Ω , and a modified stress tensor is proposed to represent closure effects of microcracks. Shao et al. (2005) proposed the DSID model based on the energy expression, which is similar as Hayakawa and Murakami's. However, the formulation of the DSID model depends on Cauchy stress tensor, so it avoids discontinuous differential in integration process. The Gibbs free energy, G_s can be calculated as follows:

$$G_s = \frac{1+\nu_0}{2E_0} \text{Tr}(\boldsymbol{\sigma}^2) - \frac{\nu_0}{2E_0} (\text{Tr}\boldsymbol{\sigma})^2 + a_1 \text{Tr}(\boldsymbol{\Omega})(\text{Tr}\boldsymbol{\sigma})^2 + a_2 \text{Tr}(\boldsymbol{\sigma} \cdot \boldsymbol{\sigma} \cdot \boldsymbol{\Omega}) + a_3 \text{Tr}(\boldsymbol{\sigma})\text{Tr}(\boldsymbol{\Omega} \cdot \boldsymbol{\sigma}) + a_4 \text{Tr}(\boldsymbol{\Omega})\text{Tr}(\boldsymbol{\sigma} \cdot \boldsymbol{\sigma}) \quad (4.7)$$

where E_0 and ν_0 are the initial Young's modulus and Poisson's ratio respectively; $\boldsymbol{\sigma}$ is the Cauchy stress; $\boldsymbol{\Omega}$ is the damage tensor, defined as the second-order crack density tensor (Kachanov, 1958), and a_i are material parameters for the free energy. The damage driving force is obtained by deriving G_s by the damage tensor:

$$\mathbf{Y} = \frac{\partial G_s}{\partial \boldsymbol{\Omega}} = a_1 (\text{Tr}\boldsymbol{\sigma})^2 \boldsymbol{\delta} + a_2 \boldsymbol{\sigma} \cdot \boldsymbol{\sigma} + a_3 \text{Tr}(\boldsymbol{\sigma})\boldsymbol{\sigma} + a_4 \text{Tr}(\boldsymbol{\sigma} \cdot \boldsymbol{\sigma})\boldsymbol{\delta} \quad (4.8)$$

The total elastic strain $\boldsymbol{\epsilon}^E$ is obtained by deriving G_s by the Cauchy stress $\boldsymbol{\sigma}$:

$$\boldsymbol{\epsilon}^E = \frac{\partial G_s}{\partial \boldsymbol{\sigma}} = \frac{1+\nu_0}{E_0} \boldsymbol{\sigma} - \frac{\nu_0}{E_0} (\text{Tr}\boldsymbol{\sigma})\boldsymbol{\delta} + 2a_1 [\text{Tr}(\boldsymbol{\Omega})(\text{Tr}\boldsymbol{\sigma})]\boldsymbol{\delta} + a_2 (\boldsymbol{\sigma} \cdot \boldsymbol{\Omega} + \boldsymbol{\Omega} \cdot \boldsymbol{\sigma}) + a_3 [\text{Tr}(\boldsymbol{\sigma} \cdot \boldsymbol{\Omega})\boldsymbol{\delta} + (\text{Tr}\boldsymbol{\sigma})\boldsymbol{\Omega}] + 2a_4 (\text{Tr}\boldsymbol{\Omega})\boldsymbol{\sigma} \quad (4.9)$$

and it contains two parts:

$$\boldsymbol{\epsilon}^E = \boldsymbol{\epsilon}^{el} + \boldsymbol{\epsilon}^{ed} \quad (4.10)$$

in which $\boldsymbol{\epsilon}^{el}$ is the purely elastic strain, which would be recovered by unloading, and $\boldsymbol{\epsilon}^{ed}$ is the additional elastic strain induced by the degradation of stiffness. Therefore, total strain $\boldsymbol{\epsilon}$ can be decomposed as

$$\boldsymbol{\epsilon} = \boldsymbol{\epsilon}^E + \boldsymbol{\epsilon}^{id} = \boldsymbol{\epsilon}^{el} + \boldsymbol{\epsilon}^{ed} + \boldsymbol{\epsilon}^{id} \quad (4.11)$$

$\boldsymbol{\epsilon}^{id}$ is the irreversible strain, induced by residual crack openings existing in a sample after a release of loading stress (additional compression is needed to close cracks and to get back to a state of zero deformation) (Abu Al-Rub and Voyiadjis, 2003).

Damage function

The expression of the damage function is written in the following form:

$$f_d = \sqrt{J^*} - \alpha I^* - k \quad (4.12)$$

J^* and I^* are defined as

$$J^* = \frac{1}{2} (\mathbb{P}_1 : \mathbf{Y} - \frac{1}{3} I^* \boldsymbol{\delta}) : (\mathbb{P}_1 : \mathbf{Y} - \frac{1}{3} I^* \boldsymbol{\delta}), \quad I^* = (\mathbb{P}_1 : \mathbf{Y}) : \boldsymbol{\delta} \quad (4.13)$$

where \mathbb{P}_1 is a fourth-order projection tensor defined as

$$\mathbb{P}_1(\boldsymbol{\sigma}) = \sum_{p=1}^3 [H(\sigma^{(p)}) - H(-\sigma^{(p)})] \mathbf{n}^{(p)} \otimes \mathbf{n}^{(p)} \otimes \mathbf{n}^{(p)} \otimes \mathbf{n}^{(p)} \quad (4.14)$$

in which $H(\cdot)$ is the Heaviside distribution function, $\sigma^{(p)}$ is the p^{th} eigenvalue of the stress tensor, $\mathbf{n}^{(p)}$ is the vector aligned with the p^{th} principal direction of stress, and α is a material parameter accounting for the aperture of the cone in the $\mathbb{P}_1 : \mathbf{Y}$ space. The threshold k in Eq.4.12 is defined as a linear function of damage:

$$k = C_0 + C_1 \text{Tr}(\boldsymbol{\Omega}) \quad (4.15)$$

where C_0 is the initial threshold of damage, and C_1 controls the damage hardening.

Damage potential

In order to enforce the constraint on the eigenvalues of damage tensor to be non-negative, it is proposed to define the damage potential as a homogeneous function of degree one in \mathbf{Y} :

$$g_d = \sqrt{\frac{1}{2} (\mathbb{P}_2 : \mathbf{Y}) : (\mathbb{P}_2 : \mathbf{Y})} - C_2 \quad (4.16)$$

The projection tensor, \mathbb{P}_2 , is introduced to represent both "crossing" and "splitting" effects (Xu and Arson, 2014; Xu, 2014):

$$\mathbb{P}_2 = \sum_{p=1}^3 H \left[\sigma^{(p)} - \min_{q=1}^3 (\sigma^{(q)}) \right] \mathbf{n}^{(p)} \otimes \mathbf{n}^{(p)} \otimes \mathbf{n}^{(p)} \otimes \mathbf{n}^{(p)} \quad (4.17)$$

Flow rule

Damage evolution law is obtained by calculating

$$d\boldsymbol{\Omega} = \lambda \frac{\partial g}{\partial \mathbf{Y}} \quad (4.18)$$

where λ is the Lagrange Multiplier accounting for the magnitude of the damage increment. Analytical solutions for elementary mechanical tests shows that the irreversible strain $\boldsymbol{\epsilon}^{id}$ is better predicted when derived from a non-associated flow rule:

$$d\boldsymbol{\epsilon}^{id} = \lambda \frac{\partial f_d}{\partial \boldsymbol{\sigma}} = \lambda \frac{\partial f_d}{\partial \mathbf{Y}} \frac{\partial \mathbf{Y}}{\partial \boldsymbol{\sigma}} \quad (4.19)$$

4.3.5.2 Implementation

The damage model is implemented with the Cutting-Plane Algorithm solving for Lagrange Multiplier. Through this method, we can have a stable method to get results for the simulation. All these implementations are based on the strain-controlled strategy, which is typically utilized in the programming of constitutive modeling. A trial calculation is tested with a new strain increment based on elastic assumption. If the yield condition is reached, the cutting-plane algorithm is utilized to drive the stress state

back to the yield surface; if the yield condition is not reached, state variables are updated using the elastic solution.

Cutting-Plane Algorithm

The Cutting-Plane Algorithm, first proposed in reference (Simo and Ortiz, 1985), is one type of return mapping algorithm and follows in a straightforward manner from the theory of operator splitting applied to nonlinear constitutive relations. Following the procedure of the algorithm summarized in the work (Simo and Hughes, 1998), we can derive all the equations for DSID model.

The damage function at next step can be linearized at the current iteration step:

$$f_{n+1}^{(i+1)} \approx f_{n+1}^{(i)} + \partial_{\sigma} f_{n+1}^{(i)} : [\boldsymbol{\sigma}_{n+1}^{(i+1)} - \boldsymbol{\sigma}_{n+1}^{(i)}] + \partial_{\Omega} f_{n+1}^{(i)} : [\boldsymbol{\Omega}_{n+1}^{(i+1)} - \boldsymbol{\Omega}_{n+1}^{(i)}] = 0 \quad (4.20)$$

From the above equation, two increment terms are needed to update. The stress can be discretizing as

$$\boldsymbol{\sigma}_{n+1}^{(i+1)} - \boldsymbol{\sigma}_{n+1}^{(i)} = -\lambda_{n+1}^{(i)} \mathbb{S}_{n+1}^{-1} : [\partial_{\sigma} f_{n+1}^{(i)} + \boldsymbol{\sigma}_{n+1}^{(i)} : \partial_{\Omega} \mathbb{S}_{n+1}^{(i)} : \partial_{\mathbf{Y}} g_{n+1}^{(i)}] \quad (4.21)$$

The flow rule (Eq.4.18) indicates that the damage increment can be discretized as

$$\boldsymbol{\Omega}_{n+1}^{(i+1)} - \boldsymbol{\Omega}_{n+1}^{(i)} = \lambda_{n+1}^{(i)} \partial_{\mathbf{Y}} g_{n+1}^{(i)} \quad (4.22)$$

Taking equations 4.21 and 4.22 into equation 4.20, we obtain an equation for computing Lagrange Multiplier:

$$\lambda_{n+1}^{(i)} = \frac{f_{n+1}^{(i)}}{\partial_{\sigma} f_{n+1}^{(i)} : \mathbb{S}_{n+1}^{-1} : [\partial_{\sigma} f_{n+1}^{(i)} + \boldsymbol{\sigma}_{n+1}^{(i)} : \partial_{\Omega} \mathbb{S}_{n+1}^{(i)} : \partial_{\mathbf{Y}} g_{n+1}^{(i)}] - \partial_{\Omega} f_{n+1}^{(i)} : \partial_{\mathbf{Y}} g_{n+1}^{(i)}} \quad (4.23)$$

The discretization reveals that this algorithm is based on a forward integration of the rate equations. The damage function will be updated with new Lagrange Multiplier and checked for convergence.

4.3.5.3 Modeling and calibration of near field rock responses against field experiments at URL

The damage model has been implemented into TOUGH-FLAC using the User Defined constitutive Model (UDM) option in FLAC3D, including C++ coding and dynamic link libraries. The new model can be utilized in the simulator TOUGH-FLAC (Rutqvist, 2011) to study anisotropic damage evolution in host rocks. In this section, we study field data at the aforementioned Manitoba URL Canada for modeling and calibration of near field rock responses. In particular, we are focusing on calibrating the implemented damage model for the excavation disturbed zone (EDZ) and potential permeability changes near underground openings. The goal is to develop a method to deduce damage induced permeability variations that can well capture the observed phenomena at the URL field experiments (Chandler et al. 2002). Moreover, we also simulate the Mine-by experiment, which is conducted earlier at the URL.

To study EDZ at both TSX and Mine-by experiment we use our damage model described in Section 4.3.5.1 by modeling the excavation process in situ. The parameters of DSID model are summarized in Table 4-5. Figures 4-42a and b display the model setup and stress states for TSX tunnel and Mine-by experiments at URL, respectively. An elliptical cross section (3.5 m high and 4.375 m wide) is configured to represent the excavated TSX tunnel in field. In this experiment, the maximum horizontal stress $\sigma_{11} = 45$ MPa, while minimum vertical stress $\sigma_{33} = 11$ MPa. The Mine-by experiment is modeled with a circular 3.5-m-diameter tunnel. The maximum horizontal stress ($\sigma_{11} = 60$ MPa) and the minimum vertical stress ($\sigma_{33} = 11$ MPa) are applied on the far field boundaries.

Table 4-5. Parameters in DSID model for TSX and Mine-by experiments.

Elastic parameters		Free Energy				Damage function		
E_0	ν_0	a_1	a_2	a_3	a_4	C_0	C_1	$\alpha(-)$
MPa	-	MPa ⁻¹	MPa ⁻¹	MPa ⁻¹	MPa ⁻¹	MPa	MPa	-
6.8×10^4	0.21	1.26×10^{-7}	3.94×10^{-5}	-1.26×10^{-6}	1.45×10^{-5}	0.001	2.2	0.231

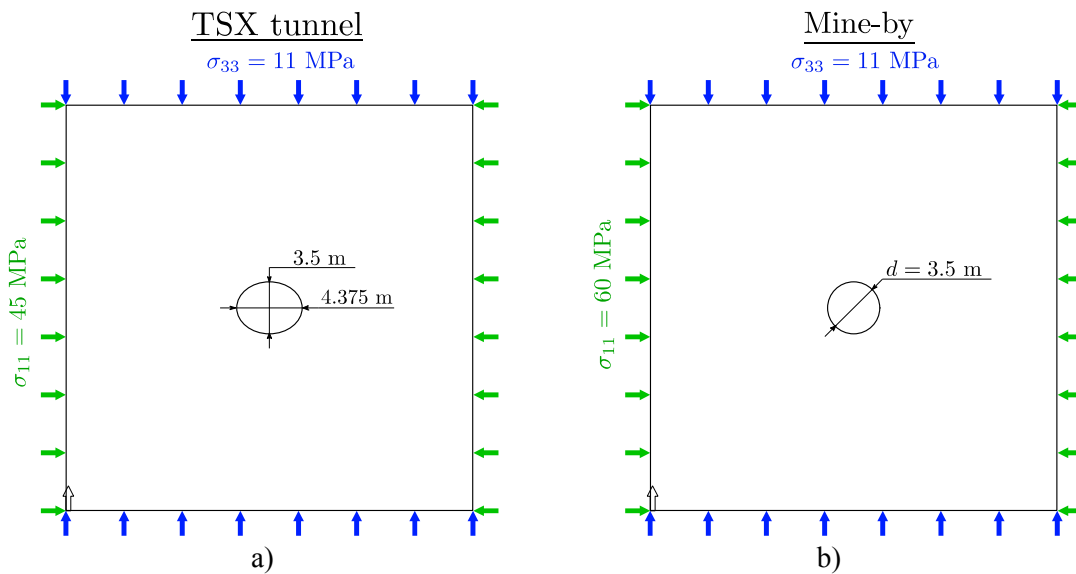


Figure 4-42. The model setup for simulations. a) TSX tunnel at URL. b) Mine-by experiment.

Damage zone around the tunnel

The simulation starts with initial equilibrium under the compression by far field stresses for TSX case. At the beginning, the tunnel is pressurized internally by the same amount of initial stresses. Then, the stresses on the surface of tunnel are released during the excavation process. A deviatoric stress, $\sigma_{11} - \sigma_{33}$, is displayed in Figure 4-43, where small tensile difference stress ($\Delta\sigma = 5$ MPa) is located around the right and left side of the drift, while high compressive difference stress ($\Delta\sigma = -100$ MPa) is presented on top and bottom of the tunnel wall. Due to the high deviatoric stress induced at these positions around the elliptical tunnel, damage is generated and propagates into the wall. The damage distribution is investigated at two locations, the roof and the right side of the drift both extending 3 m radial distance into the tunnel wall. Figure 4-44a plots the damage profiles vertically from the top of the drift, and shows that the damage variables Ω_{22} and Ω_{33} are about 0.006 at the tunnel wall. Since the maximum stress is σ_{11} , which compresses the rock in 1-direction, the stress status drives cracks opening in 2- and 3- directions, but no damage in 1-direction is found within the 3 m distance. Moreover, the damage within 1.5 m radial distance increases significantly compared with the inside positions (radial distance is greater than 1.5 m) of rocks. Figure 4-44b illustrates the damage profiles horizontally from the right springline of the tunnel, and shows that the damage is only generated within the 0.5 m radial distance. In addition to that, the magnitude of damage at right side of the tunnel wall is less than the damage at the roof.

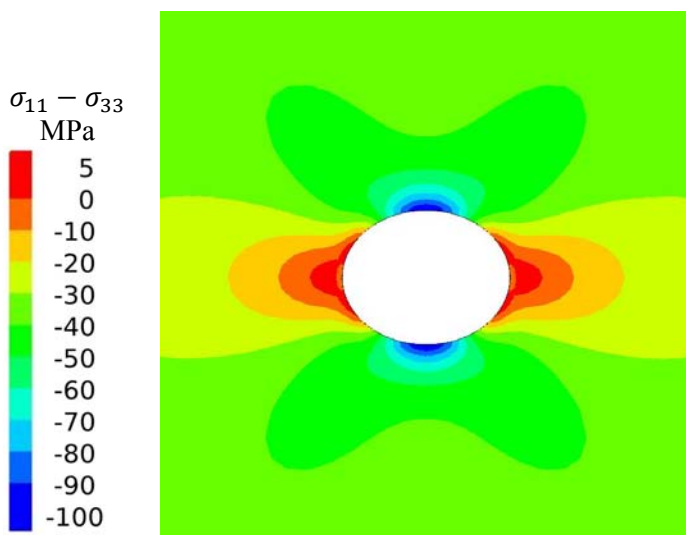
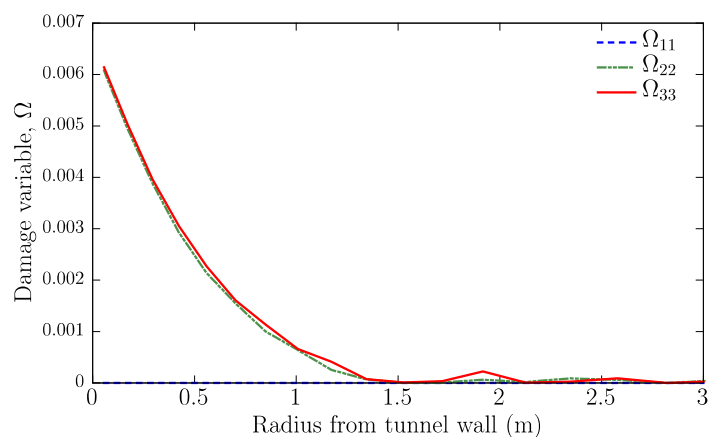
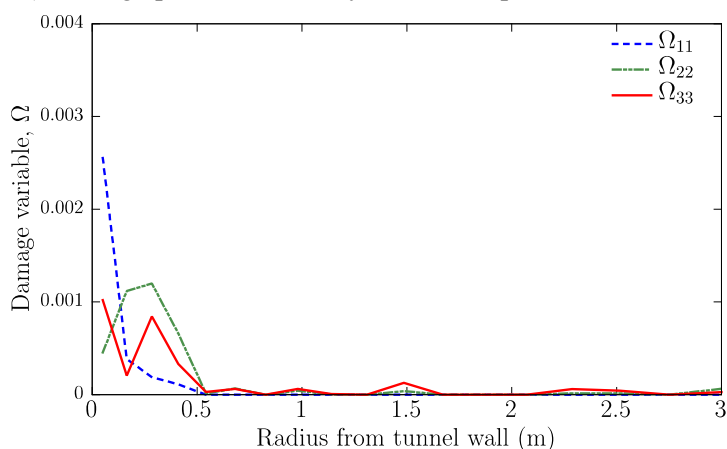


Figure 4-43. The distribution of deviatoric stress $\sigma_{11} - \sigma_{33}$ around the TSX tunnel.



a) Damage profiles vertically from the top of the TSX tunnel.



b) Damage profiles horizontally from the right surface of TSX tunnel.

Figure 4-44. The distribution of damage profiles versus the radial distance from TSX tunnel wall.

To study the size of the damage zone, we calculate the mean damage, plotted in Figure 4-45. Based on the expected stress state and the damage pattern observed at the URL *in situ* experiments, a spalling zone is expected to develop (Martin et al., 1999; Martino and Chandler, 2004; Schoenball et al., 2014). As the Figure 4-45 describes, damage is induced around the tunnel wall, and it propagates more at the top and bottom of tunnel wall. Moreover, we may predict a damage zone very close to the drift caused by excavation with this damage mechanical model. In addition, there are four circular damage zones located at 45 degrees away from the vertical direction, which are triggered and connected to the damage zones around the surface of the tunnel.

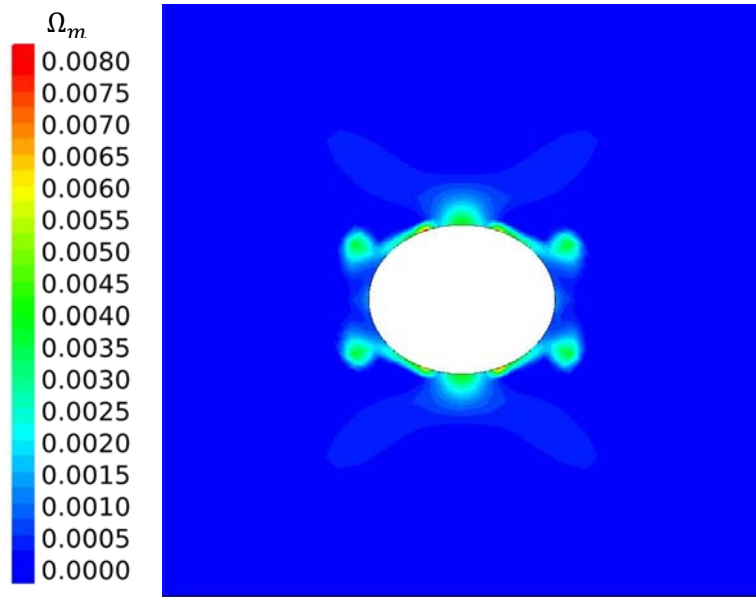


Figure 4-45. The distribution of mean damage variable in the simulation domain at TSX experiment.

Figure 4-46 presents the distribution of the deviatoric stress, $\sigma_{11} - \sigma_{33}$, at the Mine-by experiment. A similar result with the TSX case is found here, where small tensile difference stress ($\Delta\sigma = 2.6$ MPa) is located around the right and left side of the drift, while high compressive difference stress ($\Delta\sigma = -100$ MPa) is presented on top and bottom of the tunnel wall. The high compressive deviatoric stress induces that damage is generated and propagates into the wall at the top and bottom of the circular tunnel. Figure 4-47a plots the damage profiles vertically from the top of the drift, and shows that the damage variables Ω_{22} and Ω_{33} are about 0.018 at the tunnel wall, while no damage occurs in 1-direction. The damage within 1.5 m radial distance increases significantly compared with the inside positions (radial distance is greater than 1.5 m) of rocks as well as the TSX case. Figure 4-47b illustrates the damage profiles horizontally from the right springline of the tunnel, and shows that the damage is only generated within the 0.3 m radial distance at Mine-by experiment.

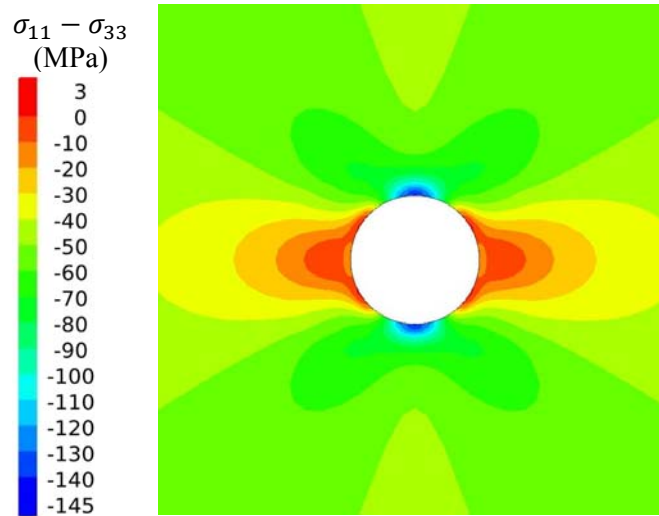
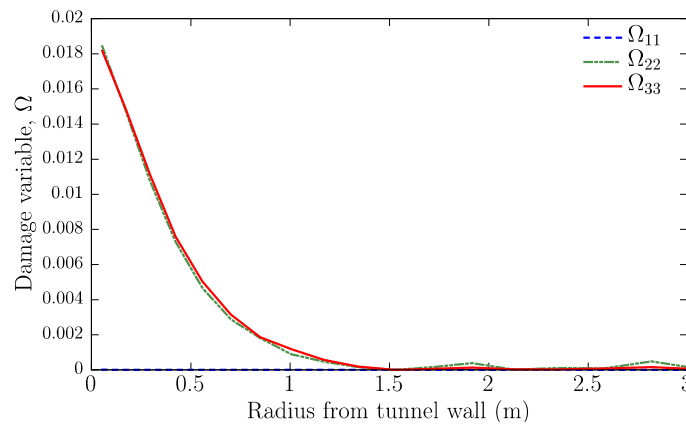
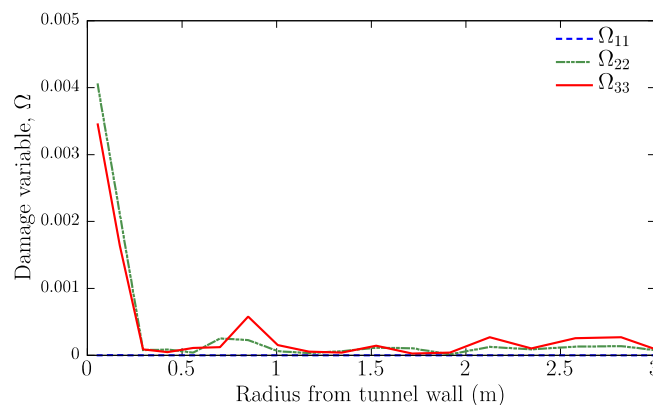


Figure 4-46. The distribution of deviatoric stress $\sigma_{11} - \sigma_{33}$ around the tunnel at Mine-by experiment.



a) Damage profiles vertically from the top of the drift at Mine-by experiment.



b) Damage profiles horizontally from the right surface of the drift at Mine-by experiment.

Figure 4-47. The distribution of damage profiles versus the radial distance from the tunnel wall at Mine-by experiment.

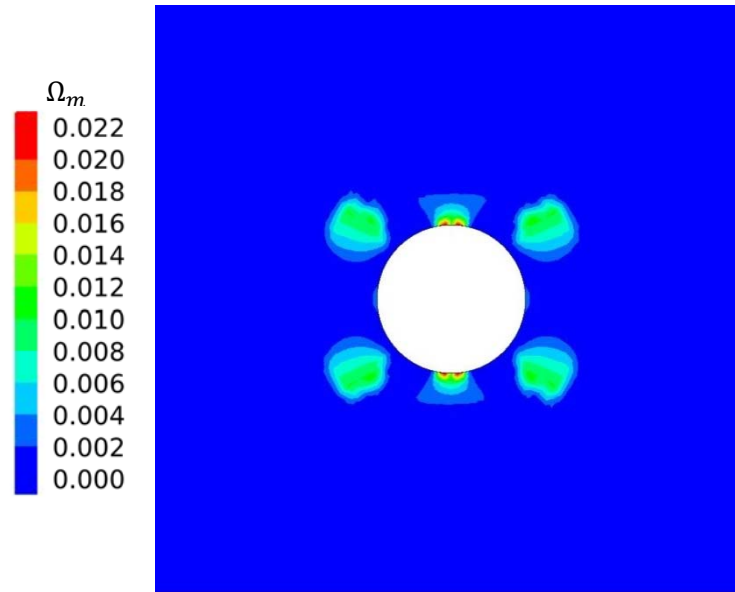


Figure 4-48. The distribution of mean damage variable in the simulation domain at Mine-by experiment.

Figure 4-48 presents the mean damage variable at Mine-by experiment. At the top and bottom of the drift, high compressive deviatoric stress induces high damage with large damage zones, which can be considered as the expected spalling zones in field, while small damage zones are located at the right and left side of the tunnel wall due to the low tensile strength. Four circular damage zones are observed in the simulation results; these are located at 45 degrees away from the vertical direction. The reason to this phenomenon is that the damage criteria are reached based on shear failure.

Study of permeability changes around the tunnels

The extent of the EDZ was studied at the TSX using measurements of permeability. The permeability was measured along eight radial boreholes and the based on those measurements (Souley et al., 2001). The changes at the springline are somewhat different from those at the top and bottom. For example, Figure 4-49 shows field data of permeability as a function of radius, which indicates higher permeability changes at the top of the drift than at the side of the drift. The permeability changes are calculated using two different equations on damage versus permeability relationships and a best match of fitting parameters as described below in more detail.

First, we tried to correlate observed permeability changes to damage using the relationship:

$$k = k_0 + \beta_i(3\Omega_m + \beta_2)^3 \quad (4.24)$$

where k_0 is the original permeability, here $k_0 = 1.5 \times 10^{-21} \text{ m}^2$; $\Omega_m = \frac{1}{3}(\Omega_{11} + \Omega_{22} + \Omega_{33})$ is the mean damage variable; β_1 and β_2 are parameters to calibrate by matching to the observed permeability profile. Here, we obtain $\beta_1 = 1.58 \times 10^{-11}$, $\beta_2 = 1 \times 10^{-100}$. The results using this relationship is noted as “Equation 1” in Figures 4-49a and b, which show calculated permeability changes along radial profiles extending from the top of the drift and from the springline of the tunnel. A good agreement between the model simulation and experimental observations is achieved with this equation except that the predicted permeability is higher along the vertical direction from the top of the drift, and the disturbed zone of permeability change is slightly smaller than the observed data along the horizontal direction from the right side of the tunnel wall.

The second equation is derived based on dimensionless analysis. Permeability has dimension L^2 , while damage variable is dimensionless. Usually, permeability is associated with the volume of domain. Thus, we assume the permeability change Δk is proportional to $V_i^{2/3}$ (V_i is the volume of i th element), which has dimension L^2 as well. In this way,

$$\Delta k \propto \beta_3 \Omega_m V_i^{2/3} \tag{4.25}$$

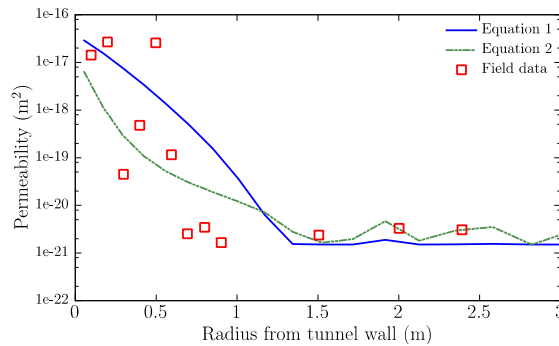
Based on Shao et al. (2005), in addition to previous equation, a crack number and a conduit coefficient related to cracks are needed to account for the permeability change. Since they are both dependent on damage, we add one function $f(\Omega_m)$ into the previous equation.

$$\Delta k = \beta_3 \Omega_m f(\Omega_m) V_i^{2/3} \tag{4.26}$$

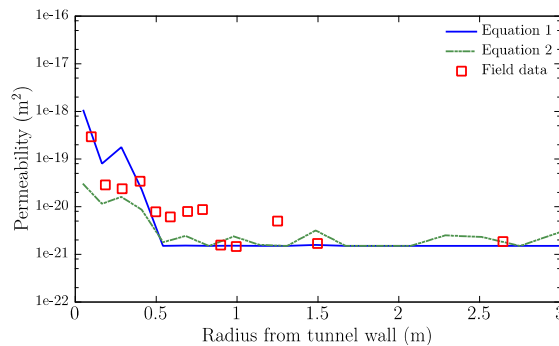
By matching to the observed permeability profile, we can derive the whole equation for current permeability:

$$k = k_o + \beta_3 \Omega_m \exp(\beta_4 \Omega_m^2) V_i^{2/3} \tag{4.27}$$

where $\beta_3 = 1 \times 10^{-15}$, $\beta_4 = 2.846 \times 10^5$ obtained from the calibration. The resulting permeability profiles using Equation (4.27) noted as “Equation 2” are shown in Figures 4-49a and b as well. We found that the permeability profile is in better agreement regarding permeability changes at the top of the tunnel whereas the profiles extending horizontally from the springline is slightly lower than the field observations.



a) Predicted permeability profiles vertically from the top of TSX tunnel.



b) Predicted permeability profiles horizontally from the right surface of TSX tunnel.

Figure 4-49. The distribution of predicted permeability versus the radial distance from the TSX tunnel wall. The field data is from Souley et al.’s work (2001).

We also calculate the permeability change in the entire simulation domain. Figures 4.50 and 4.51 display the permeability around the tunnel of TSX with “Equation 1” and “Equation 2” respectively. The results show that the permeability increases with damage growth, so the zone of permeability change follows the same shape of damage zone. However, the “Equation 2” overestimates the permeability increase at far positions from the tunnel, since Equation (4.27) accounts for the effect of lower damage on permeability change.

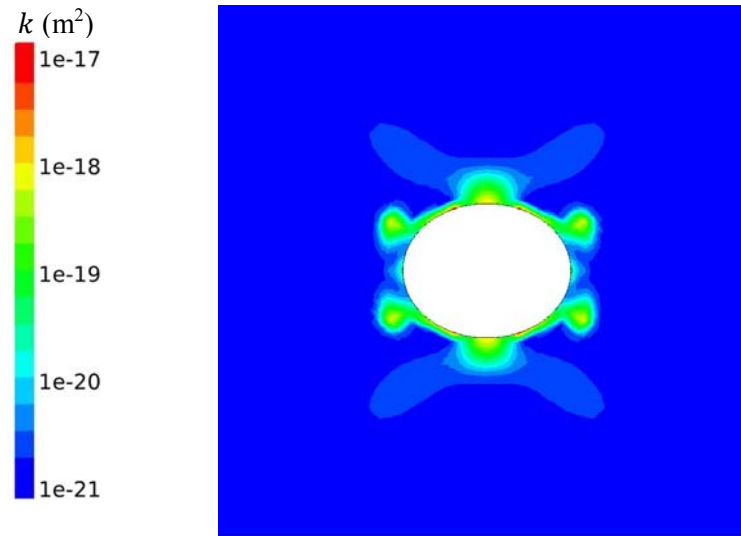


Figure 4-50. The distribution of predicted permeability in the simulation domain at TSX experiment using Equation (4.24).

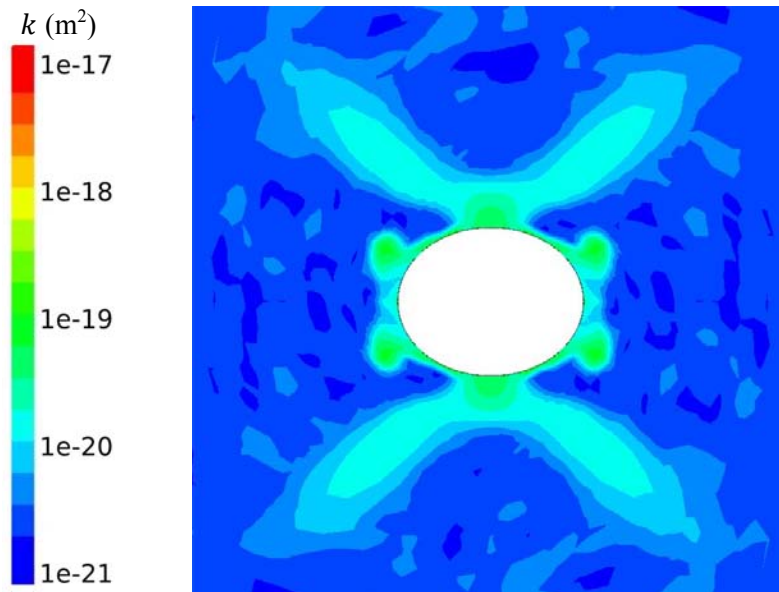
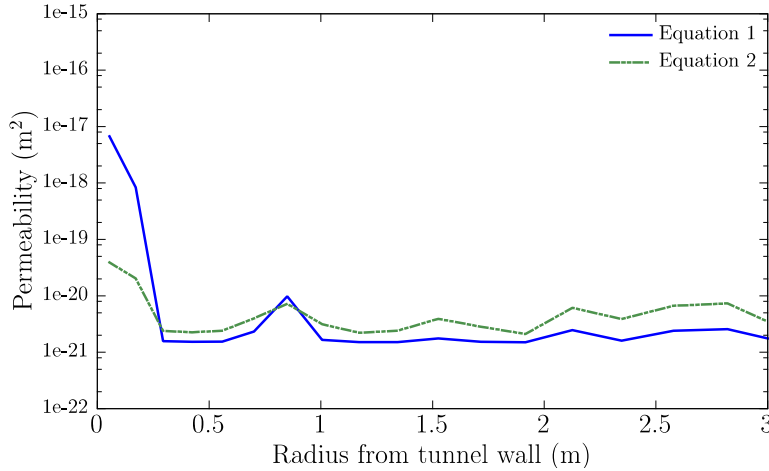


Figure 4-51. The distribution of predicted permeability variable in the simulation domain at TSX experiment using Equation (4.27).

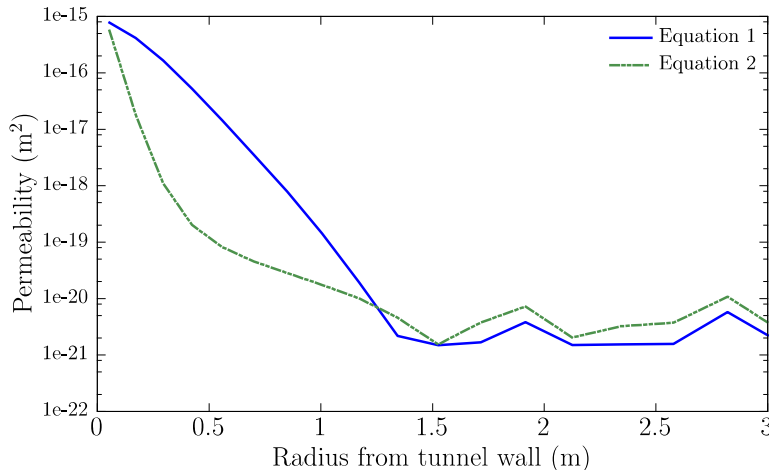
These two approaches are applied on the Mine-by experiment as well, and the results are presented in Figures 4-52a and b. In general, “Equation 1” predicts higher permeability near the surface of the tunnel but lower permeability at far positions than “Equation 2” approach. For example, in Figure 4-52a, the permeability at the tunnel wall increases to $8 \times 10^{-18} \text{ m}^2$ by using “Equation 1” whereas it can only reach

$4 \times 10^{-20} \text{ m}^2$ with “Equation 2”. However, for the position farther than 1.5 m from the surface of the tunnel, the inverse conclusion is drawn.

Figure 4-53 presents contours of permeability change around the drift using “Equation 1” for Mine-by experiment, while Figure 4-54 presents another result using “Equation 2”. The similar conclusion can be drawn that permeability increases with damage growth, and permeability change zone follows the same shape of damage zone. Moreover, the permeability at far positions from the tunnel increases more by using “Equation 2” than the result calculated with “Equation 1”, while “Equation 1” predicts higher permeability near the surface of the tunnel. With these approaches, the damage model is capable to estimate the permeability change that has been observed at several URL tunnels.



a) Predicted permeability profiles horizontally from the right surface of the drift at Mine-by experiment.



b) Predicted permeability profiles vertically from the top of the drift at Mine-by experiment.

Figure 4-52. The distribution of predicted permeability versus the radial distance from the tunnel wall at Mine-by experiment.

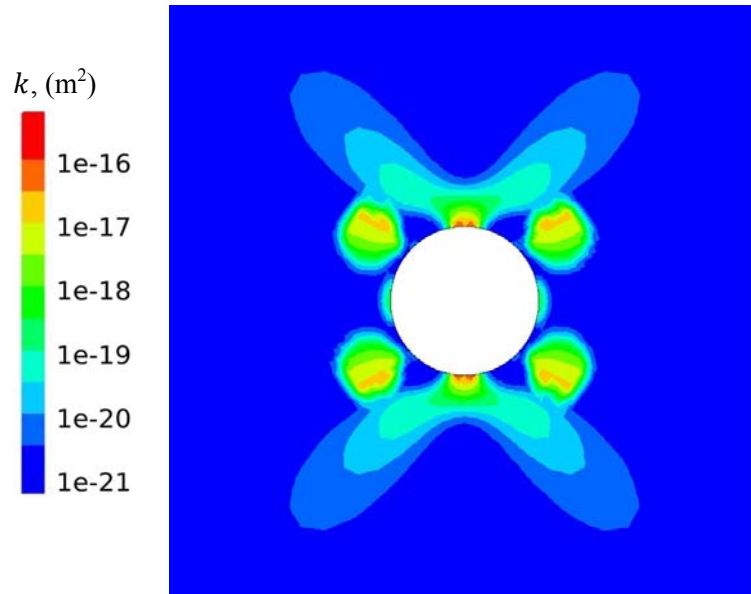


Figure 4-53. The distribution of predicted permeability in the simulation domain at Mine-by experiment using Equation (4.24).

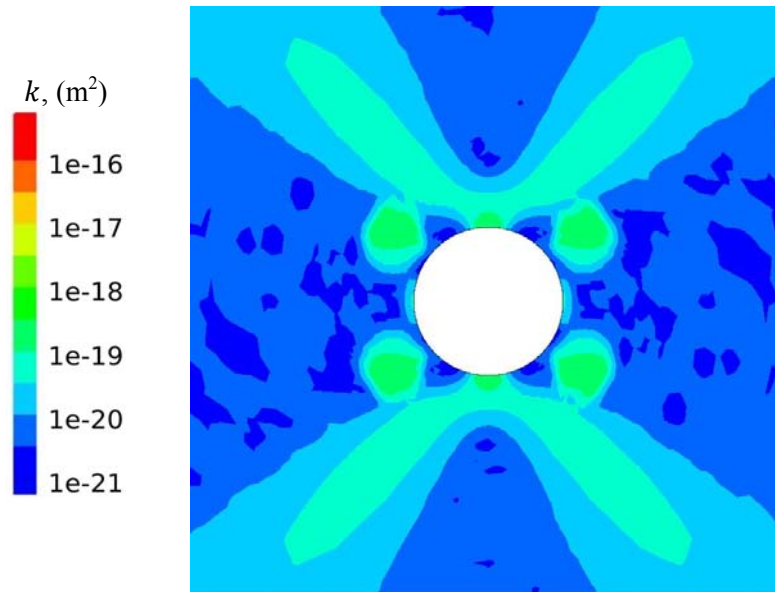


Figure 4-54. The distribution of predicted permeability in the simulation domain at Mine-by experiment using Equation (4.27). Note: the term $\beta_4 \Omega_m^2$ in Equation (4.27) is changed to $\beta_4 \Omega_m^{2.5}$ in this case.

4.3.5.4 Parametric study

Another set of parameters of the continuum damage model summarized in Table 4-6 is utilized to simulate the TSX experiment. The model setup for TSX tunnel is the same as Figure 4-41a illustrates.

Table 4-6. Parameters in DSID model for TSX experiment.

Elastic parameters		Free Energy				Damage function		
E_0	ν_0	a_1	a_2	a_3	a_4	C_0	C_1	$\alpha(-)$
MPa	-	MPa ⁻¹	MPa ⁻¹	MPa ⁻¹	MPa ⁻¹	MPa	MPa	-
6.8×10^4	0.21	1.26×10^{-7}	3.94×10^{-5}	-1.26×10^{-6}	2.51×10^{-6}	0.02	2.2	0.231

The deviatoric stress, $\sigma_{11} - \sigma_{33}$, is displayed in Figure 4-55, which shows results very close to that in Figure 4-42. The small tensile difference stress ($\Delta\sigma = 5$ MPa) is located around the right and left side of the drift, while high compressive difference stress ($\Delta\sigma = -100$ MPa) is presented on top and bottom of the tunnel wall. Figure 4-56a plots the damage profiles vertically from the top of the drift, and shows that the damage variables Ω_{33} and Ω_{22} are about 0.02 at the tunnel wall whereas no damage in 1-direction is generated ($\Omega_{11} = 0$). The difference between the current case and the previous simulation of TSX experiment is that damage is suppressed at the side of the tunnel, so Figure 4-56b illustrates the damage profiles horizontally from the right springline of the tunnel, and shows that all damage variables are equal to zero.

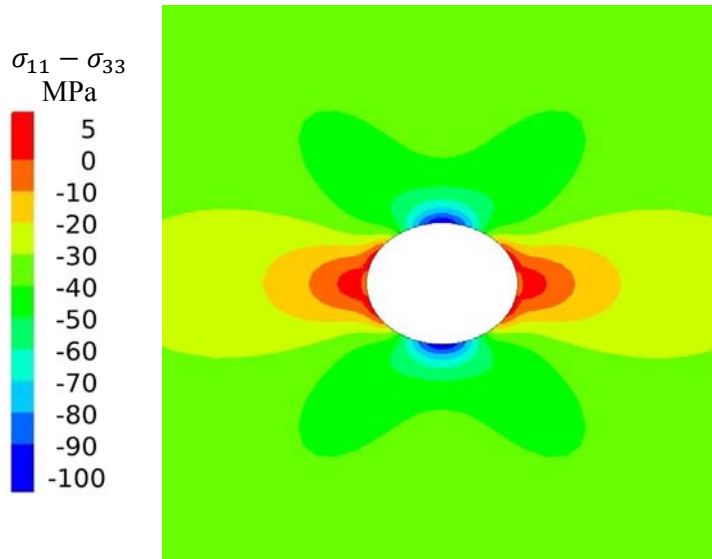
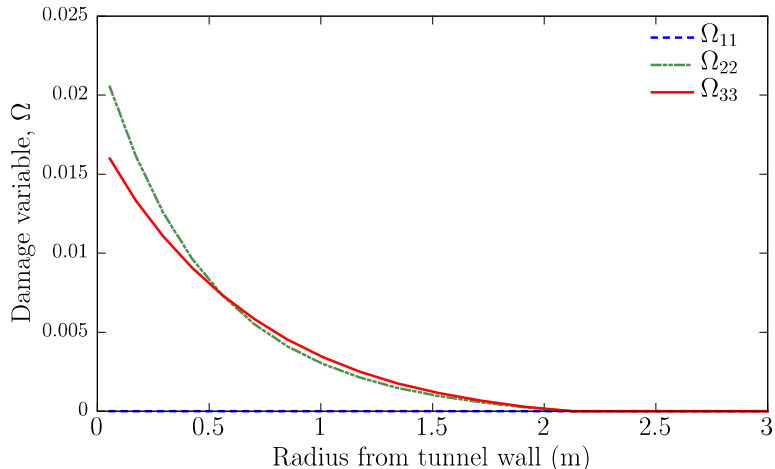
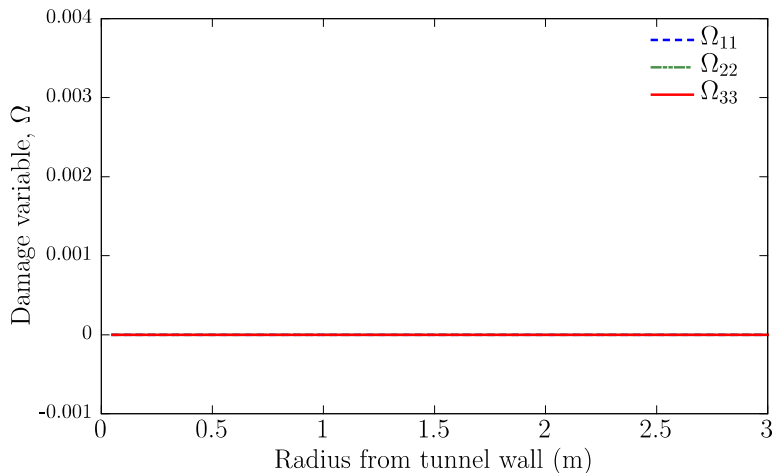


Figure 4-55. The distribution of deviatoric stress $\sigma_{11} - \sigma_{33}$ around the TSX tunnel.



a) Damage profiles vertically from the top of the TSX tunnel.



b) Damage profiles horizontally from the right surface of TSX tunnel.

Figure 4-56. The distribution of damage profiles versus the radial distance from TSX tunnel wall.

The mean damage is plotted in Figure 4-57, which indicates damage is only induced and propagates at the top and bottom of tunnel wall. Moreover, the severe damage is generated near the tunnel surface, which can be associated with the spalling zone observed in the experiment field. Compared with the results in Figure 4-45, there is no damage zone at far positions from the tunnel.

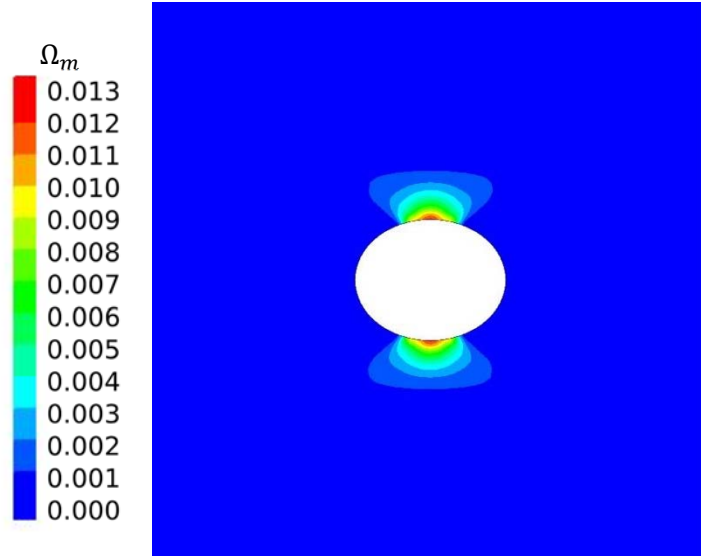
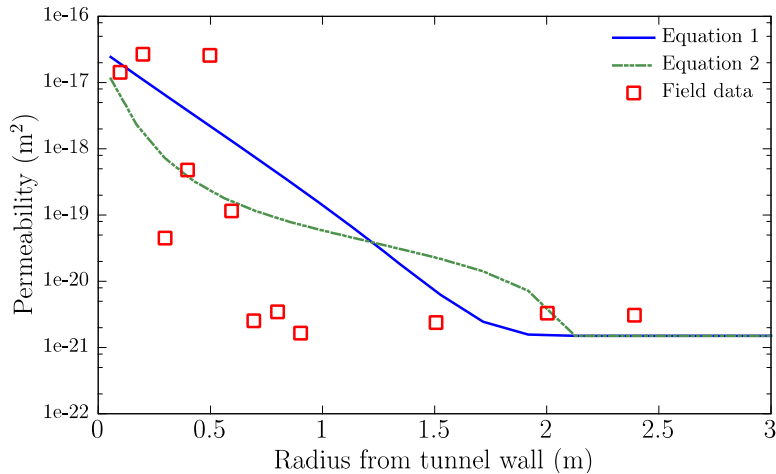


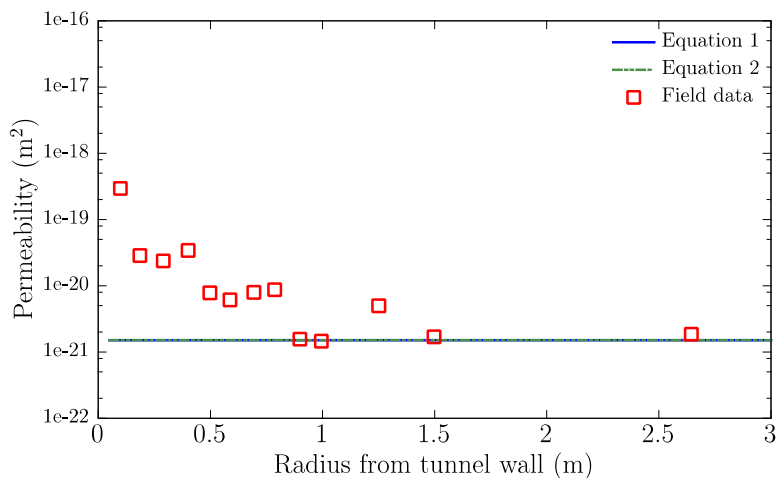
Figure 4-57. The distribution of mean damage variable in the simulation domain at TSX experiment.

To correlate observed permeability changes to damage using the relationship in Equation (4.24), we obtain: $\beta_1 = 5 \times 10^{-13}$, $\beta_2 = 1 \times 10^{-100}$ by matching the experiment data. The results using this relationship is noted as “Equation 1” in Figures 4-57a and b, which show calculated permeability changes along radial profiles extending from the top of the drift and from the springline of the tunnel. The predicted permeability is higher along the vertical direction from the top of the drift, and the disturbed zone of permeability change is slightly larger than the observed data along this direction. Since no damage initialed in horizontal direction from the right side of the tunnel wall, permeability keeps constant at the side of the tunnel.

By matching to the observed permeability profile, we obtain the parameters for Equation (4.27) are $\beta_3 = 1 \times 10^{-15}$, $\beta_4 = 2.846 \times 10^4$. The resulting permeability profiles using Equation (4.27) noted as “Equation 2” are shown in Figures 4-57a and b. We found that the permeability profile is overestimated from 0.5 m to 2 m at the top of the tunnel and the profiles extending horizontally from the spring line remain the same values as the intact status.



a) Predicted permeability profiles vertically from the top of TSX tunnel.



b) Predicted permeability profiles horizontally from the right surface of TSX tunnel.

Figure 4-58. The distribution of predicted permeability versus the radial distance from the TSX tunnel wall. The field data is from Souley et al.’s work (2001).

Figures 4-59 and 4.60 display the permeability around the tunnel of TSX with “Equation 1” and “Equation 2” respectively. The results show that the permeability increases with damage growth, so the zone of permeability change follows the same shape of damage zone. However, the “Equation 2” overestimates the permeability increase at far positions from the tunnel, but underestimates the permeability near the tunnel surface when compared with the results predicted with “Equation 1”. In this way, the permeability increase at the side of the tunnel in situ wall is not captured by this set of simulations. The reason to that is the current model only relates the permeability to damage variables and no damage is found at the side of the tunnel. To improve the model prediction, we can add the tensile strength cutoff in the yield criteria, which can account for the tensile failure near the horizontal side of the tunnel, or we can use a smaller damage threshold to trigger the damage occurs earlier, which is similar as the previous case presents. The simulation results of Mine-by experiment display the similar behavior of the damage propagation and permeability change. For the simplicity, we do not present these here.

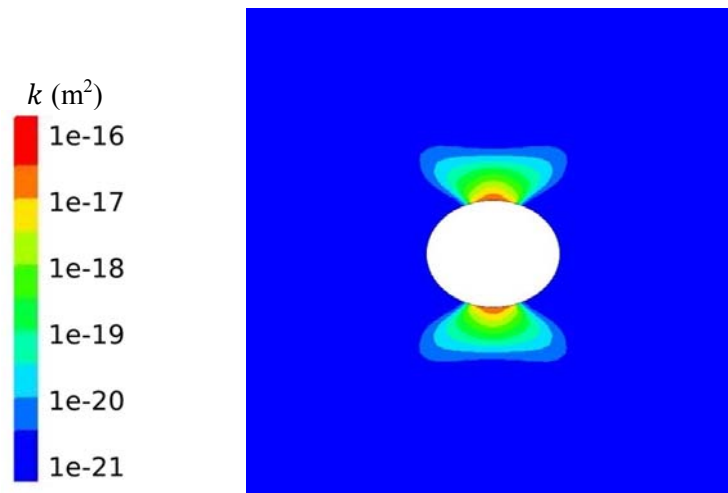


Figure 4-59. The distribution of predicted permeability in the simulation domain at TSX experiment using Equation (4.24).

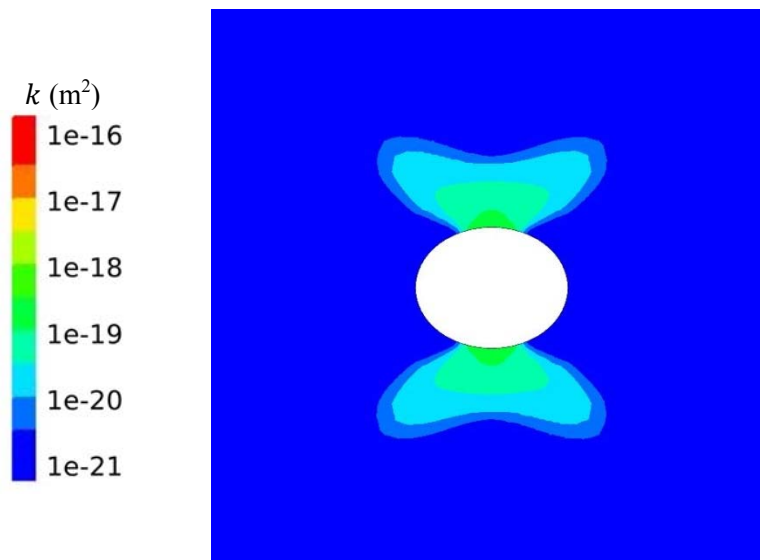


Figure 4-60. The distribution of predicted permeability variable in the simulation domain at TSX experiment using Equation (4.27).

4.3.6 Summary of THM modeling

In FY17, the THM modeling has been focused on modeling the general stress evolution and development and testing of disturbed zone models. The stress evolution modeling was done using a rational approach based on TH axisymmetric modeling results and analytical modeling of poro-elastic and thermal stresses. From this modeling a few important observations are highlighted

- During post-closure, the horizontal stresses are expected to increase with time to result in a peak stress magnitude after about 20,000 years, whereas vertical stress generally will be expected to stay constant equal to the lithostatic stress.
- Even in the case of rock mass that is initially near critically stressed for shear activation, the increasing horizontal stresses will tend to stabilize the rock mass with time. The only exception is

an increase in the potential for activation of shallowly dipping faults and fractures, as the thermal pressurization tends to reduce the effective vertical stress. Only in one case of a high maximum horizontal stress a factor of 1.3 higher than the vertical, our simulations indicated a possibility of fault activation.

- The modeling confirms that the potential for stress-induced damage of the borehole wall (borehole breakout and disturbed zone) is a key issue in deep borehole disposal. The modeling shows that the compressive stresses around the borehole may as much as double in the post-closure period and peak 20,000 after emplacement. Such changes are the biggest at 4000 m depth, but are also significant in the lower parts of seal zone (3000 m depth), whereas the post-closure stress changes are much smaller at the upper part of the seal zone (1500 m depth).
- The post-closure compressive stress at the borehole wall can be reduced considering engineering measures such as designing borehole backfill material in the sealing zone for expansion by poro-elastic, Swelling and thermo-elastic expansion. For example, a plug material with enhanced thermal expansion could provide additional support to borehole wall when needed during the thermal peak.
- A key input to the THM analysis and the potential for induced fault activation, seismicity and borehole breakout is the initial in situ stress field. At any site, it will be important to characterize the three dimensional stress field, and how it changes with depth, in the upper sedimentary zone and into the crystalline basement. Our analysis indicates that relatively low and isotropic horizontal stresses would be favorable for minimizing the potential for induced seismicity and borehole breakouts.

These results are based on our simplified stress modeling, which should be confirmed by more sophisticated coupled THM modeling. However, we expect that the general findings will be the same although we will be able to refine the analysis especially related to near borehole stressing during early time. Such a full 3D THM model is depicted in Figure 4-61. The model will be used for the remainder of FY17, first for a comparison to the stress evolution presented in this report. Other aspect not covered in the current modeling is potential shear stress changes at the edge of the repository, which might also impact the potential for induced seismicity, in FY17 we have also made the effort of developing and testing models for disturbed zone evolution, in particular for the evolution of permeability which is one of the key parameters for potential upflow through the disturbed zone. We have developed and tested two approaches, a simple stress-permeability approach and a more complex damage modeling approach. Using both approaches we could model some of the observations around tunnels in competent granite at the Manitoba URL Canada. The simplified stress-permeability model, could match to field data by calibration of a few parameters that determine how permeability changes with mean effective stress and with deviatoric (shear) stress. The damage model includes a large number of parameters with some mechanistic meaning, but it is difficult to define a unique set of parameters, although a reasonable good match to the field data was achieved. More work is needed to be able to confidently apply such model for prediction of the evolution of the disturbed zone in a deep borehole environment. Meanwhile, the simplified approach and uncertainty analysis might be a plausible option.

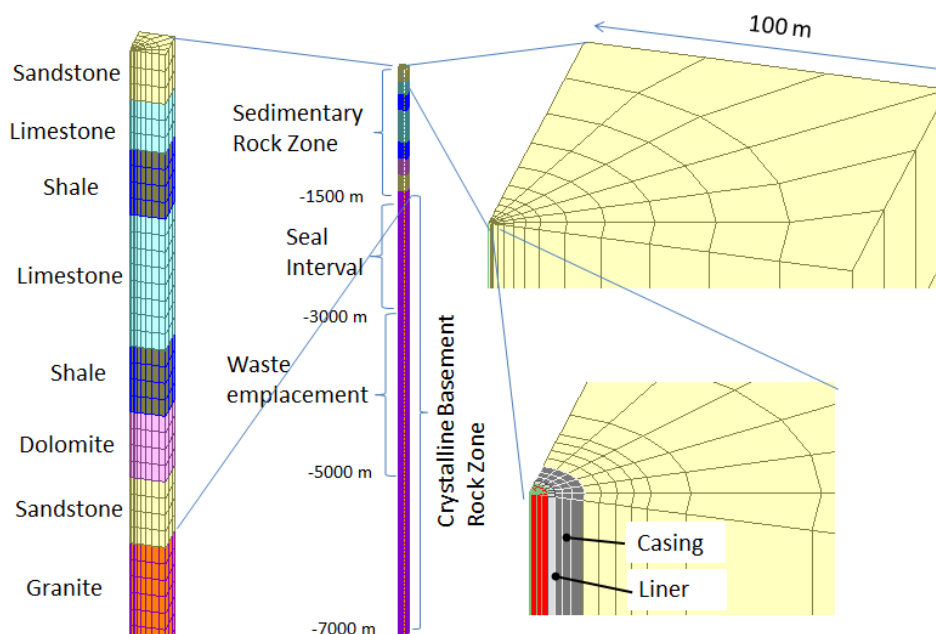


Figure 4-61. 3D TOUGH-FLAC model mesh of the deep borehole disposal for more detailed THM analysis.

4.3.7 Conclusions of seal modeling

In FY17, we have extended our analysis from TH to THC and THM modeling and development of and testing of disturbed zone models. We have summarized the findings from each of the THC and THM modeling in Sections 4.2.4 and 4.3.6, respectively. This work on seal modeling was conducted for deep borehole disposal applications, but is also directly applicable to other storage concept in terms of processes and associated model developments. For example, the disturbed zone models can be directly applied for the modeling of the disturbed zone evolution around emplacement tunnels or vertical emplacement holes in mined repositories.

4.4 References

- Abu Al-Rub, R.K. and Voyiadjis, G.Z. (2003) On the Coupling of Anisotropic Damage And Plasticity Models For Ductile Materials. *International Journal of Solids and Structures* 40, 2611–2643.
- Arnold, B.W. and Hagdu, T. (2013). Thermal-Hydrologic Modeling of a Deep Borehole Disposal System. Proceedings International High-Level Radioactive Waste Management Conference, Albuquerque, NM, Apr 2013.
- Bernot, P. (2005) Dissolved Concentration Limits of Radioactive Elements, ANL-WIS-Md-000010 REV 05.
- Brady, P.V., Arnold, B.W., Freeze, G.A., Swift, P.N., Bauer, S.J., Kanney, J.L., Rechar, R.P., Stein, J.S. (2009). Deep Borehole Disposal of High-Level Radioactive Waste, Report SAND2009-4401, July 2009.
- Brandl, H. (2006) Energy Foundations And Other Thermo-Active Ground Structures. *Géotechnique* 56, 81–122.
- Brown E.T. and Hoek E (1978) Trends In Relationships Between Measured In Situ Stresses And Depth. *International Journal of Rock Mechanics and Mining Sciences*. 15, 211-215.

- Brudy, M., Zoback M.D., Fuchs K, Rummel F., and Baumgärtner J. Estimation of the Complete Stress Tensor to 8 Km Depth In The KTB Scientific D Rill Holes: Implications For Crustal Strength. *Journal of Geophysical Research*, 102, 18,453-18,475, 1997.
- Chaboche, J.-L. (1992) Damage Induced Anisotropy: on the Difficulties Associated With The Active/Passive Unilateral Condition. *International Journal of Damage Mechanics* 1, 148–171.
- Chandler, N.A, Cournut, A., Dixon, D., Fairhurst, C., Hansen, F., Gray, M., Hara, K., Ishijima, Y., Kozak, E., Martino, J., Masumoto, K., McCrank, G., Sugita, Y., Thompson, P., Tillerson, J., and Vignal, B. (2002) The Five-Year Report On The Tunnel Sealing Experiment: An International Project of AECL, JNC, ANDARA and WIPP, AECL Whiteshell Laboratories, Pinawa, Manitoba, AECL-12127.
- De Windt, L., F. Marsal, E. Tinseau and D. Pellegrini 2008. Reactive Transport Modeling Of Geochemical Interactions At A Concrete/Argillite Interface, Tournemire site (France). *Physics and Chemistry of the Earth, Parts A/B/C* 33, Supplement 1(0): S295-S305.
- Dobson P. C. Tsang, T. Kneafsey, S. Borglin, Y. Piceno, G. Andersen, S. Nakagawa, K. Nihei, J. Rutqvist, C. Doughty, M.Reagan. (2016). Deep Borehole Field Test Research Activities at LBNL, FCRD-UFD-2016-000438; LBNL-1006044
- ENRESA (2000). Full-Scale Engineered Barriers Experiment For A Deep Geological Repository In Crystalline Host Rock FEBEX Project, European Commission: 403.
- Frape, S.K. and Fritz, P. 1987. Geochemical trends for groundwaters from the Canadian Shield. In: Fritz, P. & Frape, S.K. (eds) *Saline Water and Gases In Crystalline Rocks*. Geological Association of Canada, Special Papers, 33, 19-38.
- Greenberg, H.R., Wen, J., Buscheck, T.A. (2013). Scoping Thermal Analysis of Alternative Dual-Purpose Canister Disposal Concepts. LLNL-TR-639869, June, 2013.
- Hayakawa, K., and Murakami, S. (1997) Thermodynamical Modeling Of Elastic-Plastic Damage And Experimental Validation Of Damage Potential. *International Journal of Damage Mechanics* 6, 333–363.
- Huenges E., J. Erzinger, J. Ktick, B. Engeser, W. Kessels, (1997). The Permeable Crust: Geohydraulic Properties Down To 9101 Depth, *Journal of Geophysical Research*, Vol. 102, No. B8, Pages 18,255-18,265.
- Kachanov, L. (1958) Rupture Time Under Creep Conditions. *Izvestia Akademii Nauk SSSR, Otdelenie tekhnicheskich nauk* 8, 26–31.
- Lauber, M., B. Baeyens and Bradbury, M. H. (2000) Physico-Chemical Characterisation and Sorption Measurements of Cs, Sr, Ni, Eu, Th, Sn and Se on Opalinus Clay from Mont Terri. PSI Bericht Nr. 00-10 December 2000 ISSN 1019-0643.
- Lund B., and Zoback M.D. Orientation and Magnitude Of In Situ Stress To 6.5 Km Depth in the Baltic Shield. *International Journal of Rock Mechanics and Mining Sciences* 36 (1999) 169-190.
- Martin C.D., Kaiser PK., and McCreath DR. Hoek-Brown Parameters For Predicting The Depth Of Brittle Failure Around Tunnels. *Canadian Geotechnical Journal* 36(1):136-151 (1999).
- Martino JB, and Chandler NA. (2004) Excavation-Induced Damage Studies at the Underground Research Laboratory. *International Journal of Rock Mechanics & Mining Sciences* 41: 1413–1426.
- Pruess, K., Oldenburg, C.M., Moridis, G.J. (1999). TOUGH2 Users Guide, Version 2. LBNL report 43134
- Rutqvist J. (2011) Status of the TOUGH-FLAC Simulator and Recent Applications Related To Coupled Fluid Flow And Crustal Deformations. *Computers & Geosciences*, 37, 739–750.

- Rutqvist J. The Geomechanics Of Co2 Storage In Deep Sedimentary Formations. *International Journal of Geotechnical and Geological Engineering*, 30, 525–551 (2012).
- Rutqvist J., Barr D., Birkholzer J.T., Fujisaki K., Kolditz O., Liu Q.-S., Fujita T., Wang W. and Zhang C.-Y. A Comparative Simulation Study of Coupled THM Processes And Their Effect On Fractured Rock Permeability Around Nuclear Waste Repositories. *Environmental Geology*, 57, 1347–1360 (2009a).
- Rutqvist J., Börgesson L., Chijimatsu M., Hernelind J., Jing L., Kobayashi A. and Nguyen S. Modeling of Damage, Permeability Changes And Pressure Responses During Excavation of the TSX Tunnel in Granitic Rock at URL, Canada. *Environmental Geology*, 57, 1263–1274 (2009b).
- Rutqvist J., Stephansson O. and Tsang C.-F. Uncertainty In Estimate Of Maximum Principal Stress From Hydraulic Fracturing Due To The Presence Of The Induced Fracture. *International Journal of Rock Mechanics & Mining Sciences* 37, 107-120 (2000).
- Rutqvist J., Zheng L., Chen F, Liu H.-H, and Birkholzer J. Modeling of Coupled Thermo-Hydro-Mechanical Processes with Links to Geochemistry Associated with Bentonite-Backfilled Repository Tunnels in Clay Formations. *Rock Mechanics and Rock Engineering*, 47, 167–186 (2014).
- Schoenball M., Sahara D.P., Kohl T. (2014) Time-Dependent Brittle Creep As A Mechanism For Time-Delayed Wellbore Failure. *International Journal of Rock Mechanics & Mining Sciences* 70: 400–406.
- Shao, J., Zhou, H., Chau, K. (2005) Coupling Between Anisotropic Damage And Permeability Variation In Brittle Rocks. *International Journal for Numerical and Analytical Methods in Geomechanics* 29, 1231–1247.
- Simo, J. and Hughes, T. (1998) Computational Inelasticity, Interdisciplinary Applied Mathematics. Springer-Verlag, New York.
- Simo, J. and Ortiz, M. (1985) A Unified Approach To Finite Deformation Elastoplastic Analysis Based On The Use Of Hyperelastic Constitutive Equations. *Computer Methods in Applied Mechanics and Engineering* 49, 221–245.
- Souley, M., Homand, F., Pepa, S. and Hoxha, D. 2001. Damage-induced permeability changes in granite: a case example at the URL in Canada, *International Journal of Rock Mechanics and Mining Sciences*, 38(2): 297-310.
- Tsang, C.-F., Bernier, F., Davies, C. (2005) Geohydromechanical processes in the excavation damaged zone in crystalline rock, rock salt, and indurated and plastic clays-in the context of radioactive waste disposal. *International Journal of Rock Mechanics & Mining Sciences* 42, 109–125.
- Wronkiewicz, D.J.; Bates, J.K.; Wolf, S.F.; and Buck, E.C. Ten-year results from unsaturated drip tests with UO₂ at 90°C: implications for the corrosion of spent nuclear fuel. *Journal of Nuclear Materials*, 238, (1), 78-95 (1996).
- Xu, H. (2014) Theoretical and numerical modeling of anisotropic damage in rock for energy geomechanics, PhD thesis, Georgia Institute of Technology, Atlanta, GA.
- Xu, H. and Arson, C. (2014) Anisotropic damage models for geomaterials: Theoretical and numerical challenges. *International Journal of Computational Methods, Special Issue on Computational Geomechanics* 11.
- Xu, H. and Prévost, J.-H. (2017) Integration of a continuum damage model for shale with the cutting plane algorithm. *International Journal for Analytical and Numerical Methods in Geomechanics*. doi:10.1002/nag.2563
- Xu, T., N. Spycher, E. Sonnenthal, G. Zhang, L. Zheng and K. Pruess 2011. TOUGHREACT Version 2.0: A simulator for subsurface reactive transport under non-isothermal multiphase flow conditions. *Computers & Geosciences* 37(6): 763-774.

Zang, A. and Stephansson, O. (2010), Stress Field of the Earth's Crust, Springer, Dordrecht, 32

Zheng L., L. Li, J. Rutqvist, H. Liu and J. Birkholzer. (2012). Modeling Radionuclide transport in clays. FCRD-UFD-2012-000128.

This page intentionally left blank

5. SEAL EXPERIMENTS

5.1 Introduction

Because the seal section of the borehole used for the waste disposal is expected to be at depths of 3-5 km, the borehole wall will be subjected to significantly high stresses from the overburden and possible tectonic forces. The resulting stress concentrations on the borehole wall can cause spalling and buckling failure of the rock (borehole breakout), and tensile fracturing under extremely high level of stress anisotropy, which compromises the integrity of the waste repository by providing bypassing permeability in the rock around the seals. The primary objectives of the seal experiments are to investigate: (1) the geometry of the damage around a borehole (borehole breakout, tensile fracturing) within crystalline rock under high stress, (2) the hydrological properties of the damage zone, and (3) the hydrological-mechanical-chemical (HMC) changes of the damage zone and the seal materials (cement, bentonite) via diffusion and transport of fluid (water), once the seal is placed within the borehole.

One major challenge of conducting laboratory borehole breakout experiments to investigate the behavior of the rock around a planned field borehole is the large differences in the scales. The planned waste disposal borehole has a diameter as large as half a meter, which is very difficult to reproduce in the laboratory. Reducing the scale (or diameter) of the borehole is also problematic, because fracturing and breakout of rock can be strongly dependent upon the mineral grain size (e.g., Duan and Kwok, 2015) and initial flaw size distribution (e.g., Martin et al., 1994), which may also be related to the mineral grain boundaries for relatively intact rock. For this reason, our experiment initially used extremely fine-grained crystalline rock (novaculite) in order to reproduce mineral grain size to borehole diameter ratios similar to the field borehole. As we describe in the following sections, however, this particular rock was found to be extremely (or excessively) strong, and we could not produce a breakout around a borehole. For this reason, we changed our experimental strategies from modeling the behavior of the entire borehole (cross section) while preserving the grain size to the borehole diameter ratio, to reproducing the local stress state within a field-scale partial borehole, using tight, crystalline rock (granite), which was realistic for the waste repository.

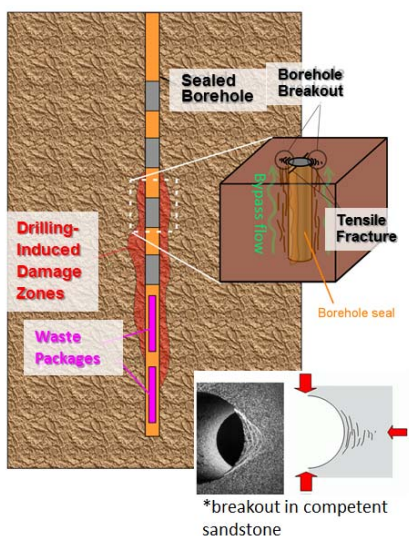
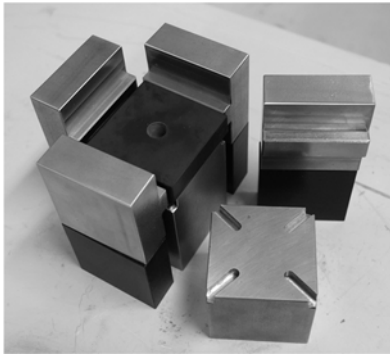


Figure 5-1. Drilling-induced damage around a waste disposal well, which can result in undesirable fluid leakage pathways along the well.

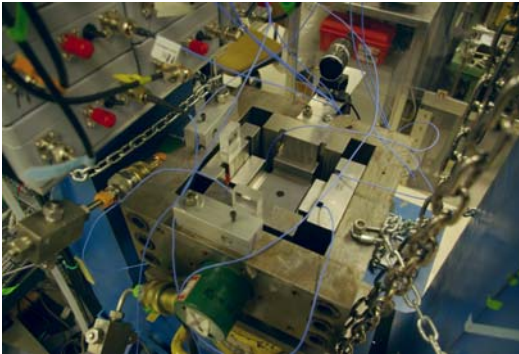
5.2 Breakout Experiments Using Rectangular Sample

5.2.1 Experimental Setup

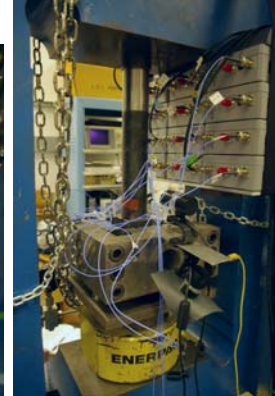
Previously in FY2016, we conducted our laboratory borehole breakout experiments by using flat, rectangular slabs of novaculite ($5.08 \text{ cm} \times 5.08 \text{ cm} \times 1.27 \text{ cm}$) containing an analogue borehole at the center. In these experiments, principal stresses up to $(\sigma_x, \sigma_y, \sigma_z) = (79 \text{ MPa}, 116 \text{ MPa}, 79 \text{ MPa})$ were applied (σ_y =maximum horizontal stress perpendicular to the borehole) using a true-triaxial loading system (Figure 5-2). The system consisted of a small lateral biaxial load frame fitted with two Simplex hydraulic cylinders (R101) and a high-capacity vertical load frame with an Enerpac pancake cylinder (RSM1500). The hydraulic fluid pressure and flow were controlled by three ISCO syringe pumps. The horizontal stresses (79 MPa) in these experiments were the maximum that can be applied using this setup, due to a relatively small loading capacity of the lateral loading system. The experiments did not produce any breakout or any significant fracturing indicated by acoustic emissions, which were monitored via a total of eight high-frequency, miniature acoustic emission (AE) transducers (Score Atlanta Inc., PICO Z sensors, frequency band 200kHz-800kHz). The AE data collection and processing was performed using an AMSY-6 acoustic emission measurement system (Valen Systeme).



(a) Novaculite slab



(b) Lateral biaxial load frame



(c) True triaxial loading test

Figure 5-2. Triaxial loading tests on a rectangular slab of novaculite containing an analogue borehole. Acoustic emissions were monitored concurrently with the loading tests.

In FY2017, we modified the experimental setup so that the maximum horizontal stress was applied vertically (i.e., the sample was rotated by 90 degrees). With this new setup, the maximum applicable principal stresses were $(\sigma_x, \sigma_y, \sigma_z) = (29 \text{ MPa}, 79 \text{ MPa}, 354 \text{ MPa})$ where σ_x is the borehole parallel stress and σ_z is the maximum “horizontal” stress. Three untreated (by heat) novaculite slabs (Young’s and shear moduli 93.4 GPa and 42.3 GPa, respectively, and Poisson ratio of 0.11) were tested, containing a single, through-going, 9.5 mm diameter analogue borehole.



Figure 5-3. Rectangular slab samples (Slab “B”, “C”, and “D”) used for the experiments.

5.2.2 Experimental Results

During the experiments, the principal stresses were first increased proportionally to $(\sigma_x, \sigma_y, \sigma_z) = (29 \text{ MPa}, 79 \text{ MPa}, 79 \text{ MPa})$ at a constant rate. Once these stresses were reached, only σ_z was increased and acoustic emissions from the sample were monitored (Figure 5-4). For the Slab B sample, large increases in the AE activity were observed after the first major fracturing occurred at $\sigma_z \sim 240 \text{ MPa}$. The sample was loaded up to $\sigma_z \sim 278 \text{ MPa}$ (the largest stress concentration on the borehole wall reaching as high as 755 MPa) (Figure 5-4a). Upon unloading, the sample was examined carefully for any surface damage. However, to our surprise, no significant and visible breakout was found. To investigate if we can produce macroscopic fractures at all in this sample, we reloaded Slab B again but this time, without applying the borehole-parallel stress (i.e., $\sigma_x=0$). This resulted in much more active AE emissions as well as a single, macroscopic fracture paralleling the maximum principal stress plane (Figure 5-4b).

The experiments were repeated for Slabs C and D, reaching higher maximum horizontal principal stress ($\sigma_z \sim 335 \text{ MPa}$ and 320 MPa , respectively). For Slab C, fracturing of the sample surface occurred as soon as the σ_z larger than σ_y was applied, as confirmed by the AE history and by the AE location plot (Figure 5-4c - Red circle). The behavior of Slab D was very similar to Slab B, with first large fracturing and frequent AE activity starting at $\sigma_z \sim 250 \text{ MPa}$. For all the cases, no significant damage in the borehole was observed except for minor surface spalling (Figure 5-5).

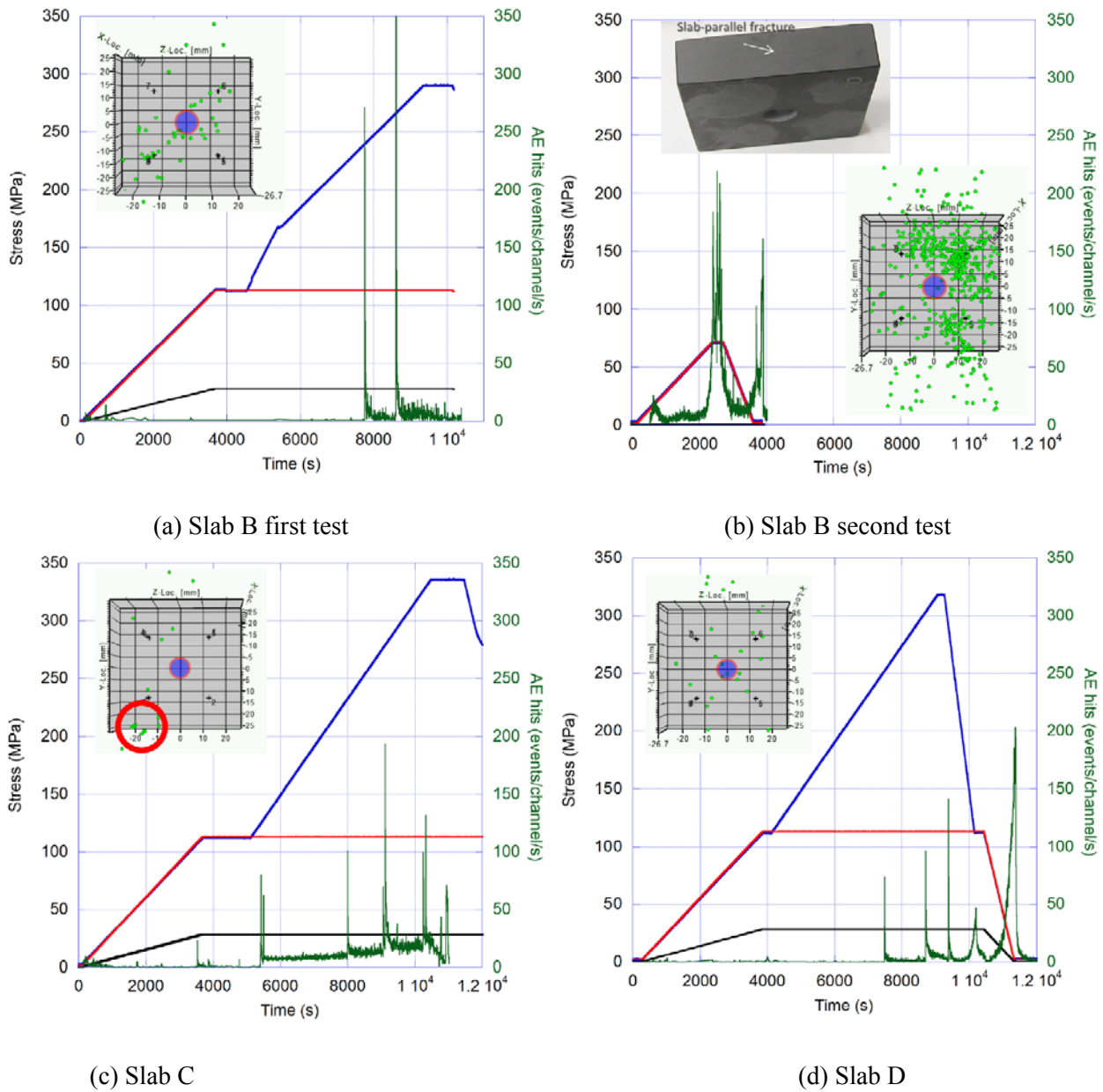


Figure 5-4. Loading and acoustic emission histories during true-triaxial loading tests on novaculite slab samples containing an analogue borehole.

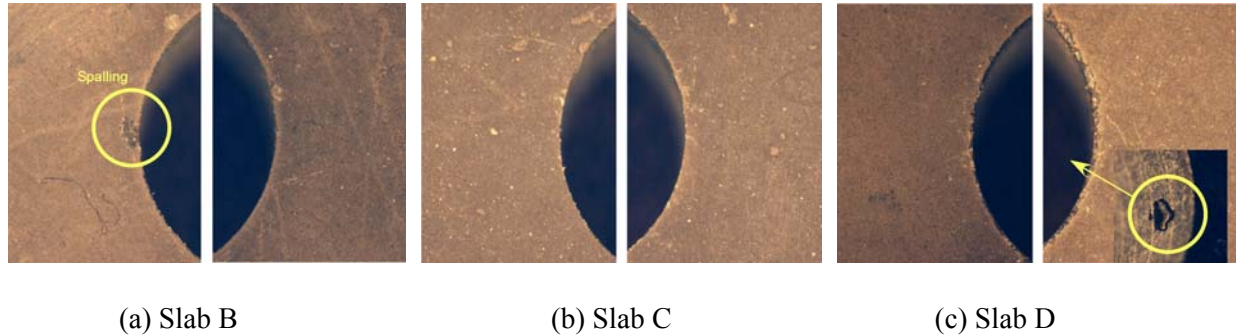


Figure 5-5. Post-experiment examination of the samples at the locations where borehole breakout was expected. The diameter of the borehole is 9.5 mm. No significant damage was observed in spite of increased acoustic emission activity and extremely high stress along the borehole wall.

5.3 Breakout Experiments Using Shaped Cores/Slabs

5.3.1 Experimental Setup

Conducting laboratory borehole breakout experiments using an analogue borehole under (true) triaxial stresses is difficult, because a very large loading capability may be required for the testing system. This is particularly true for strong, crystalline rocks with its uniaxial compression strength exceeding 100 MPa (and higher). With some limitations, however, compressive failure of the borehole wall due to stress concentration—a salient feature of borehole breakout—can be reproduced and studied using rock samples with a shaped (curved) surface (Nakagawa and Ewy, 2008). This idea is particularly attractive for testing very strong granitic rocks, because the method requires only uniaxial compression of the sample, which can be achieved relatively easily in the laboratory.

This “shaped core uniaxial compression test” was done previously only using granular rocks (i.e., sandstones), and the validity of the test had to be confirmed for low-porosity crystalline rocks. Therefore, in the laboratory, we conducted several tests on readily available, already fabricated shaped cores of Stripa Granite (core diameter 5.08 cm, length 5.08 cm) (Figure 5-6). Ultrasonic P-wave velocities of the rock measured in three orthogonal directions were 5,985 m/s, 5,896 m/s, and 5,637 m/s (max difference 5.9%), and the fastest and slowest S-wave velocities were 3,595 m/s and 3,323 m/s (difference 12.7%). Ignoring the anisotropy in the sample, and using the average velocities and the density of the sample (2.62 g/cc), the Young’s modulus and the Poisson ratio are 77.2 GPa and 0.23, respectively.

For the determined (assumed) elastic moduli, we computed the stress concentrations within the shaped cores, using linear-elastic, axisymmetric finite element models (LISA ver.8.0.0. <http://www.lisa-fet.com/>). One-quarter models of the cross section are shown in Figure 5-7, for the axial (vertical) stress. The boundary conditions are such that the bottom surface is fixed vertically, and unit pressure (compression is negative) is applied at the top. In addition, a stainless steel ring (Young’s modulus of 200 GPa and Poisson ratio of 0.3) is fitted closely to the side of the cores, to reduce the tensile stress induced in the cores (indicated by a square region). From these plots, the maximum stress concentrations in the samples are 2.2, 3.6, and 5.7, for the applied, unit axial stress (Note that negative values indicate compression). In the next section, these results are compared against experimentally measured stresses at the onset of borehole.



Figure 5-6. Shaped core samples of Stripa Granite. From the left, sample #1 through #6.

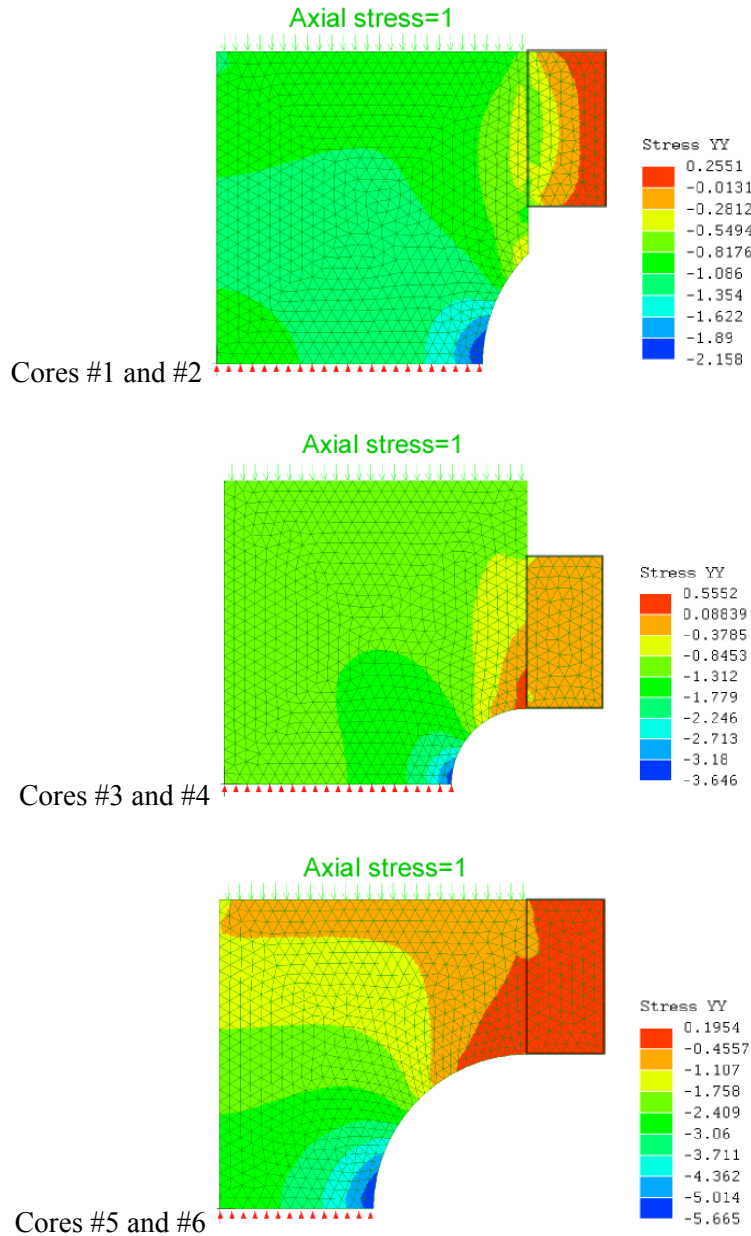


Figure 5-7. Axial stresses computed for the shaped cores in Figure 5-6. Unit axial stress is applied at the top of the sample. Blue regions adjacent to the curved surfaces of the models indicate where the maximum compressive (shown in negative values) stress concentration occurs.

The core samples were attached with tightly fitting stainless steel rings, and then compressed uniaxially in a loading frame. To minimize potential loss of debris from breakout formation, a heat-shrink jacket was applied loosely to the curved surface. During the loading test, the axial displacement was increased at a near-constant rate by introducing the hydraulic oil into the axial hydraulic cylinder at a constant rate. The resulting changes in the axial stress and displacement were monitored. Concurrently, acoustic emissions from the sample were also monitored using a pair of AE sensors embedded in the top and bottom loading platens (Figure 5-8).



Figure 5-8. Laboratory setup for the shaped-core uniaxial compression experiments using Stripa Granite cores.

5.3.2 Experimental Results

Obtained axial stress vs deformation curves and the time history of the axial stresses for three core samples with different geometries are shown in Figure 5-9. For Core #1, the same core was compressed twice (Core 1b), in order to create a significant degree of damage on the curved surface. The arrows in the figures indicate when a marked increase in the AE activity started in the AE histories presented in Figure 5-10. The stress corresponding to these arrows are ~125 MPa, 100 MPa, and 50 MPa, respectively, for Cores 1, 3 and 5 (For core#1, the first test (Core 1a) only). Although not a perfect match, the ratios between the inverses of these stresses (2.16: 2.7: 5.4) (note that these will give the stress concentration ratios) roughly correspond to the numerical-model-predicted stress concentrations (2.16: 3.6: 5.7) in 5.3.1, except for Core 3 which quantitatively showed a larger difference.

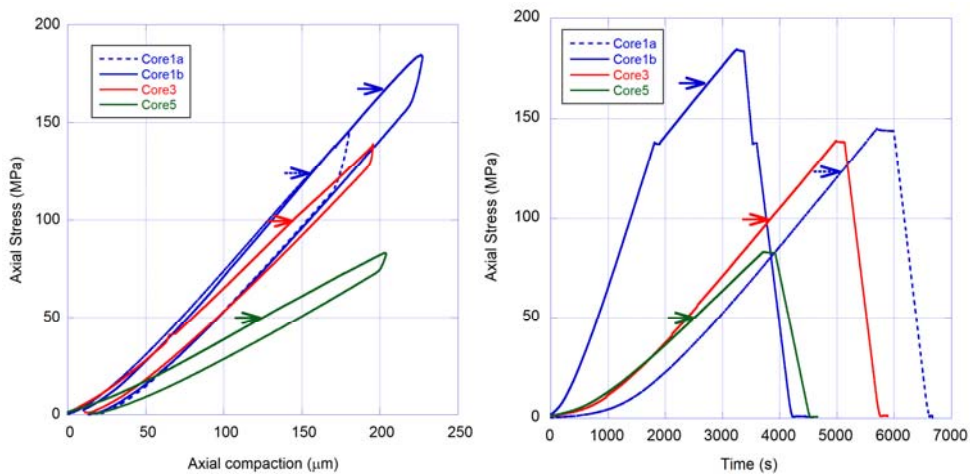


Figure 5-9. Measured axial stress vs deformation curves (left) and axial stress time history (right) for three of the shaped Stripa Granite cores.

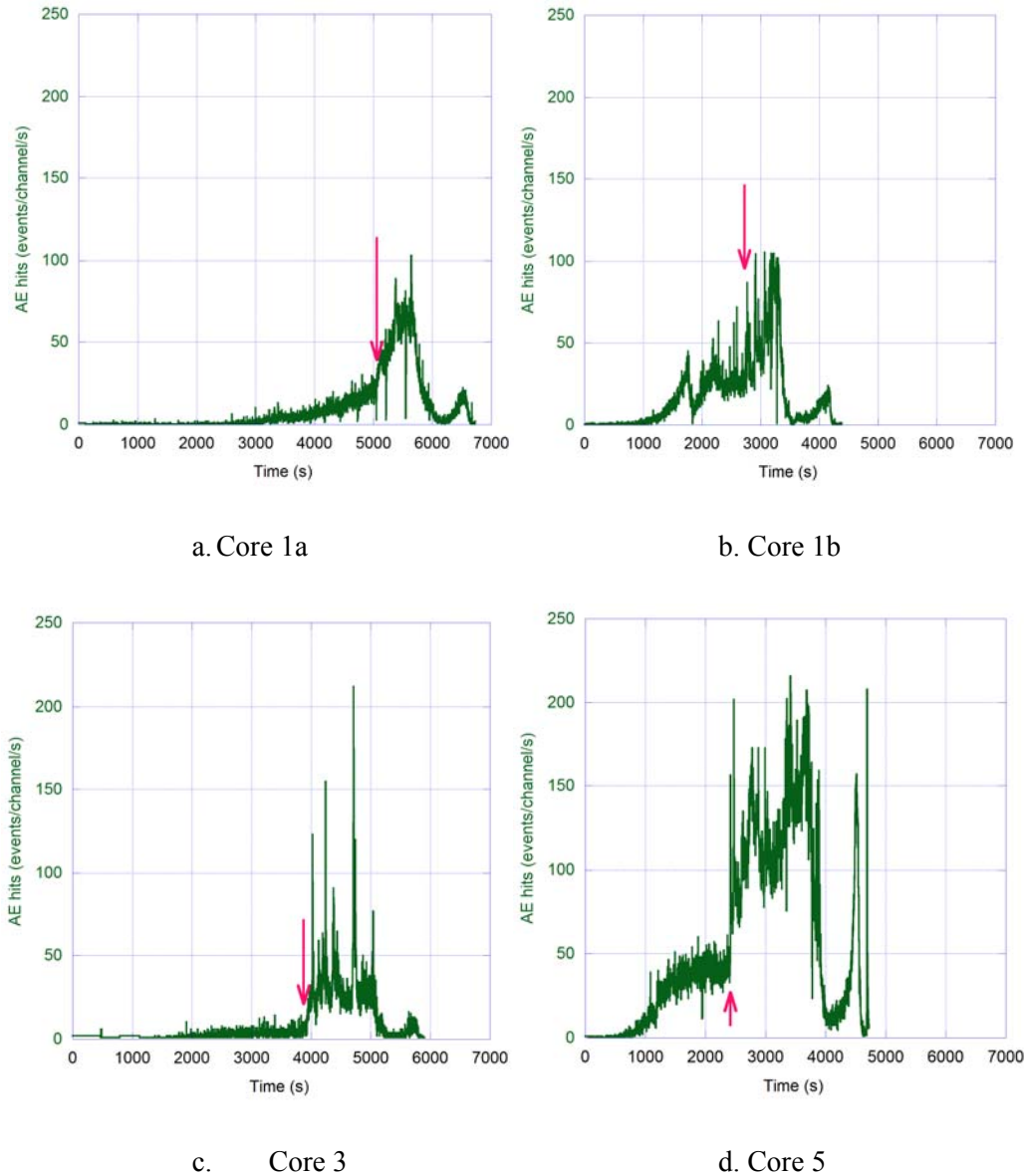
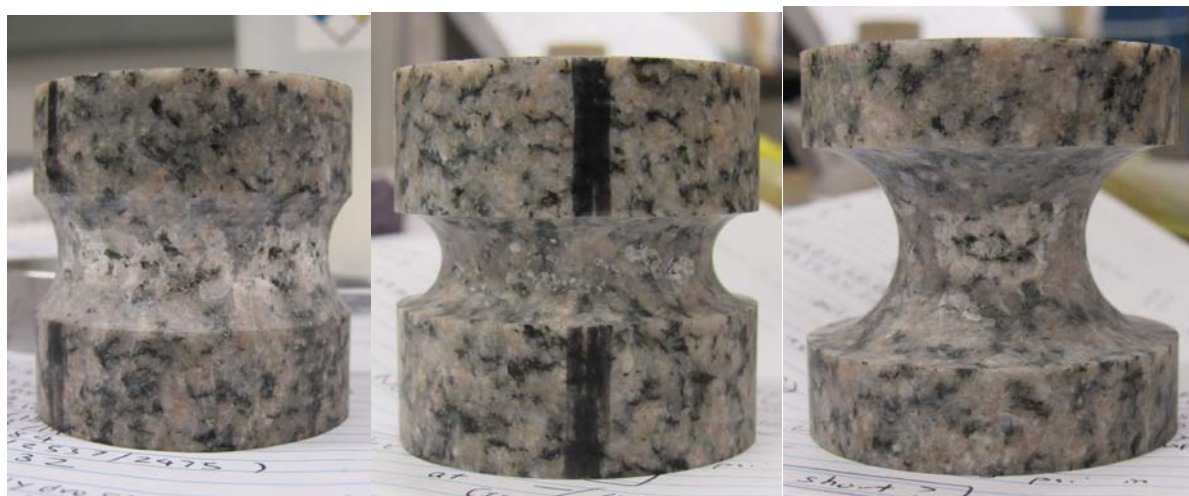


Figure 5-10. Measured acoustic emissions during the loading tests. The red arrows indicate an onset of increased AE activity.

Observation of the core surfaces after the experiments confirmed the occurrence of “borehole breakout” (Figure 5-11). Among the three cores, Core 3 exhibited the least degree of damage, with only small spots of the rock spalling off the curved surface. In contrast, the twice-loaded Core 1 exhibited extensive damage. The overall AE activity was most prominent with Core 5 (which has the smallest minimum core cross section), which may indicate more frequent internal microfracturing than other cores. X-ray CT images of the core cross sections at the narrowest part (where the breakout occurred) are shown in Figure 5-12. Core 1 exhibits some loss of the material on the surface and prominent surface-subparallel fractures. Core 5 shows some material loss near the top of the image, but no clear fractures are visible in either Core 3 or Core 5.

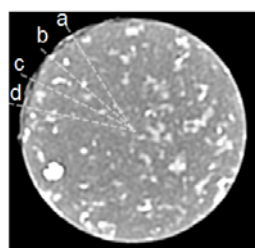


(a) Core 1

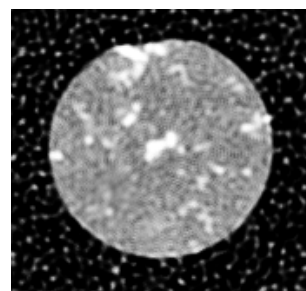
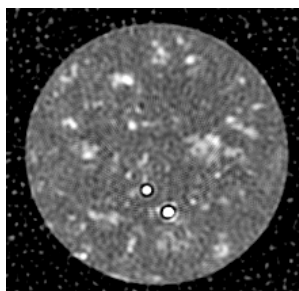
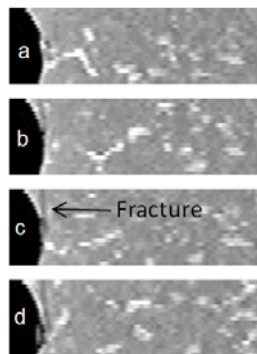
(b) Core 3

(c) Core 5

Figure 5-11. Photographs of the cores after the compression experiments. Borehole-breakout like damage can be seen along the curved surface of the cores.



X-ray CT images of fractures in "breakout"



(a) Core 1

(b) Core 3

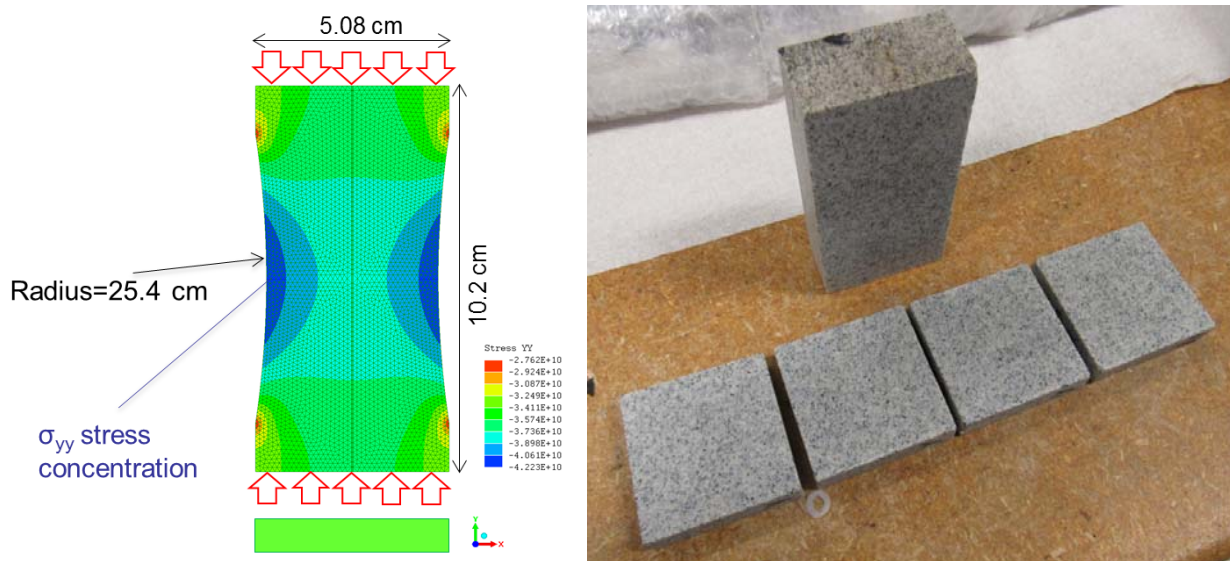
(c) Core 5

Figure 5-12. X-ray CT images of the Stripa cores after the compression experiments. For Core 1, breakout and fractures near the curved surface of the core can be seen clearly.

5.3.3 Shaped Slab Experiment

The shaped-core experiments in 5.3.1 demonstrate the possibility of using modified sample geometry to study borehole breakout in crystalline rock, without using a real-size borehole or high-loading-capacity triaxial loading systems. However, the round circumference of the core samples may distort the development of a breakout, particularly once the fractures start to grow. This is because fracturing-induced expansion of the sample surface with a convex curvature receives less restriction of the deformation from the surrounding rock, compared to a real, straight borehole. Additionally, the equivalent borehole diameters (or curvatures) in 5.3.1 are still much smaller than a field borehole.

For these reasons, we consider another sample geometry involving curved surfaces on the sides of a rectangular slab (Figure 5-13a). A stress analysis is performed using a 2D linear-elastic, plain-strain finite-element model (LISA ver.8.0.0. <http://www.lisa-fet.com/>). This particular geometry has a length of 10.2 cm, width of 5.08 cm, and a thickness of 2.54 cm. The long sides of the slab have a concave cut with a radius of 25.4 cm. The material's Young's modulus and the Poisson ratio are 72 GPa and 0.25, respectively, considering a fine-grained Westerly Granite slab shown in Figure 5-13b, which is currently being prepared for the test. For this model, 200 MPa of axial compression is applied at the top, resulting in distributions of vertical stress σ_{yy} and horizontal stress σ_{xx} in Figure 5-14. The stresses along the bottom line of the model (from the surface of the sample, away from the "borehole") are shown in Figure 5-15 and are compared to the stresses for an equivalent borehole (diameter 50.8 cm) within an infinite medium. For the latter, far field stresses of $(\sigma_{xx}^{\infty}, \sigma_{yy}^{\infty}) = (100 \text{ MPa}, 200 \text{ MPa})$ are applied.



(a) "Shaped slab" sample geometry

(b) Westerly Granite slab currently being prepared

Figure 5-13. Preparation of shaped-slab sample for a large-diameter borehole breakout experiment.

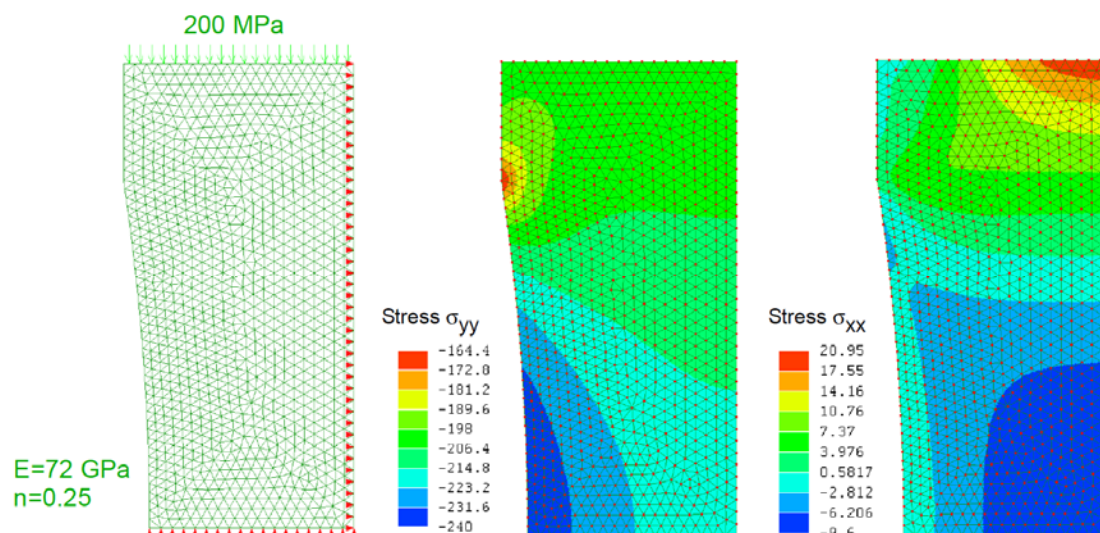


Figure 5-14. Distributions of stresses induced in a shaped slab sample resulting from an application of compression stress at the top.

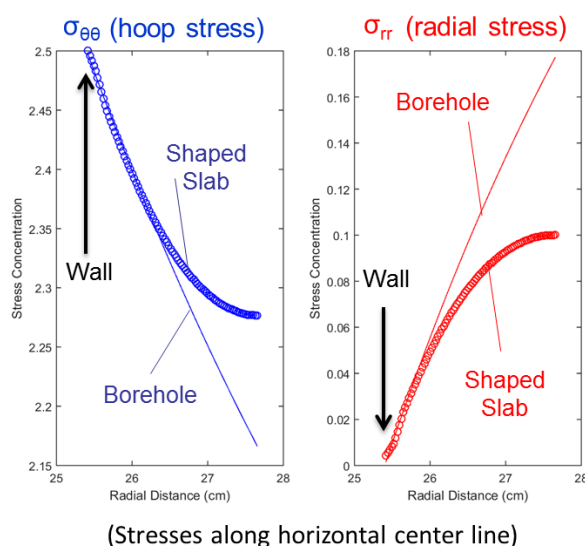


Figure 5-15. Comparisons between stresses along the minimum horizontal stress line (along the bottom of the model shown in Figure 5-14) of the shaped slab sample and a borehole within an infinite medium with a far-field compressional maximum stresses ratio of $(\sigma_{xx}^{\infty}, \sigma_{yy}^{\infty}) = (100 \text{ MPa}, 200 \text{ MPa})$. Note that, along the centerline, $\sigma_{xx} = \sigma_{rr}$ and $\sigma_{yy} = \sigma_{\theta\theta}$.

These results indicate that the stress state near the expected breakout location of the shaped slab sample can be very similar to a large-diameter borehole with the same surface curvature. Admittedly, as a breakout grows and the failure occurs away from the curved surface, the two stress states deviate away from each other. However, this test method can provide a useful tool for investigating the impact of relatively shallow borehole breakouts on the mechanical and hydrological behavior of drilling-induced damage.

5.4 Conclusion

In this task, we tried to produce a borehole breakout in tight, crystalline rock in the laboratory to study its impact on undesired enhancement of borehole-parallel fluid flow permeability. Because of unexpectedly high strength and toughness of ultra-fine-grain quartzite used to address the mineral grain size issue, the initial attempt was not successful. However, an alternate technique using a shaped core did successfully produce a borehole breakout (or breakout-like failure). Numerical modeling indicates that a similar experiment using a shaped slab sample can produce near-surface borehole breakout that can be interpreted as a breakout occurring in a large-diameter borehole, which is a possible waste repository option in deep crystalline rock.

At this point, it is still difficult to conclude if a borehole breakout in tight, crystalline rock can have a significant impact on the seal integrity. The laboratory experiments so far have indicated that a breakout clearly visible on the borehole surface is not necessarily accompanied by permeability-enhancing fractures behind it, as far as X-ray CT images can tell. This may imply that small breakouts do not cause problems as long as they are treated properly (via cement and clay fillings, for example). Extensive breakouts with fractures extending deep into the host rock are difficult to study in the laboratory, but they may be more easily detectable in the field (via direct inspection and geophysical methods), and has to be dealt with case-by-case basis (for example, excluding the breakout sections from waste storage).

For the remainder of the FY2017, we plan to complete the breakout experiment using a shaped slab, and measure the permeability changes in the rock around the (analogue) borehole caused by breakout-induced fractures.

5.5 References

- Duan, K. and C.Y. Kwok. 2015. Evolution of stress-induced borehole breakout in inherently anisotropic rock: Insights from discrete element modeling, *J. Geophys. Res., Solid Earth*, 121, 2361-2381, DOI:10.1002/2015JB012676.
- Martin, C.D., J.B. Martino, and E.J. Dzik. 1994. Comparison of borehole breakouts from laboratory and field tests, SPE 28050, SPE/ISRM Rock Mechanics in Petroleum Engineering Conference, Delft, The Netherlands, August 29-31, 183-190.
- Nakagawa S. and R. Ewy. 2008. Shaped-Core Uniaxial Compression Test for Studying Borehole Breakout in Rocks, In Proceedings of 42nd US Rock Mechanics Symposium, ARMA-08-158, 29 June-2 July, San Francisco, CA.

This page intentionally left blank

6. DESIGN OF SITE CHARACTERIZATION AND MONITORING EFFORTS

6.1 Introduction

During this reporting period, research on the design of site characterization and monitoring methods and tools focused on the development of a full-waveform single well seismic approach for imaging and characterizing large-scale faults and fractured zones in basement crystalline rock. The concept under investigation uses seismic sources and receivers located in a single borehole, and focuses on utilizing information contained in seismic data produced by a range of source types, including pressure (scalar) sources, oriented body force and particle velocity (vector) sources and moment (tensor) sources. The approach supports multi-component receivers, e.g., three component accelerometers or geophones. The overall objective of this effort is to develop a sensitive and robust approach for identifying the presence and characterizing the properties of fractures and faults out to distances of approximately 10–50 m from the borehole that could potentially serve as high-permeability pathways for radionuclide transport to the shallow subsurface (Kuhlman et al., 2015).

The utility of seismic methods for imaging and characterizing permeable fractures and faults stems from the sensitivity of compressional and shear waves to mechanical weaknesses in rock. Fractures and faults with sufficient connected porosity and permeability to support fluid flow and radionuclide transport represent structural weaknesses in a rock mass, and have higher elastic compliances relative to the unfractured host rock. These features, despite their limited thickness, can give rise to a number of potentially diagnostic elastic wave phenomena, including reflections, conversions (e.g., from P-wave to S-wave and vice-versa), diffractions, scattering and interface waves. All of these wave phenomena increase in magnitude with the frequency of the incident wave (i.e., as the seismic wavelength decreases). Effective utilization of these wave phenomena in seismic imaging of fractures and faults requires a full-waveform modeling approach, such as elastic full-waveform inversion.

In the following, we describe work towards the development of an elastic full-waveform inversion capability for imaging faults and fractures that uses multi-component seismic waves generated and recorded in a single borehole. The basic theory and features of the elastic full-waveform imaging code are described, and an example using this code for a single vertical fault zone is provided. The final section gives conclusions and recommendations for further work. This effort leverages basic research on geophysical imaging of subsurface processes conducted under the U.S. DOE-BES Program (Contract DE-AC02-05CH11231, Chemical Sciences, Geosciences & Biosciences Division).

6.2 Single well seismic imaging with a full-waveform approach

The focus of this effort has been on the development of a numerical capability for performing elastic full-waveform imaging of fractures in 3D using directional sources and receivers. The elastic full-waveform approach accounts for both the vector nature of the source and receivers, as well as the full elastic wavefield that is produced when incident P- and S-waves interact with fractures and faults. The use of an elastic full waveform modeling code allows converted reflected, refracted and diffracted waves generated at the fractures to be utilized in the imaging process.

For the full waveform-modeling engine, we have developed a 3D viscoelastic finite difference code that is tuned to satisfy efficiency and accuracy requirements for seismic modeling and imaging. Fractures are modeled as thin anisotropic features with reduced normal and shear compliances (Coates and Schoenberg, 1995; Schoenberg and Sayers, 1995). Poroelastic effects related to fluid mobility within and outside the fracture are not presently included.

To image fractures with elastic full waveform inversion, a two-step approach is used. The first step uses one iteration of full-waveform inversion as an elastic reverse time migration (RTM) to form a spatial image of the fractures that is used to estimate fracture orientation (azimuth and dip). The second step performs

full-waveform inversion to recover the fracture properties. An important part of this effort is to build an understanding of the parts of the fracture that can be imaged from a single borehole using scalar, vector and tensor sources and an array of multi-component receivers.

6.2.1 Full-waveform inversion with multi-component sources and receivers

The implementation of full-waveform inversion for this project utilizes a nonlinear conjugate gradient (NLCG) solver. For the model properties to be determined, we use the elastic constants. Given a starting model for the elastic properties of the intact rock surrounding the borehole, the NLCG algorithm iteratively updates these model properties using a gradient descent optimization scheme that seeks to image fractures by minimizing the misfit between the observed seismic data and the modeled seismic data. The current implementation is for isotropic elastic models, but the plan is to upgrade this to tilted-transverse isotropy (TTI) to account for texture and fabric in the host rock and for directional compliance in the fractured zones. For the seismic data we allow for scalar (pressure), vector (body forces and particle velocities) and tensor (moment and dipole) sources, and up to 4-component (4C = pressure + 3 particle velocities) receivers. The NLCG gradients and step-length, which are required to advance the minimization of the observed-modeled data misfit, are computed using the adjoint state method (Tarantola, 1984; Virieux, & Operto, 2009), and with a parabolic line search, respectively.

6.2.2 Numerical implementation

The modeling code that forms the engine for full-waveform inversion uses a time-domain staggered grid finite difference viscoelastic scheme with eighth order accuracy in space and second or fourth order accuracy in time. Accuracy is improved using an approach that selects the optimum finite difference coefficients, which minimize the numerical dispersion error in each finite difference cell according to the seismic velocity of that cell. Using this scheme, the required phase accuracy for typical propagation distances can be achieved with approximately three cells per minimum wavelength. Efficiency is significantly improved by employing OpenMP threading with cache blocking in the compute-intensive 3D finite difference loops. With this numerical scheme, 3D viscoelastic forward modeling on models comprised of 100's of millions of finite difference cells can be achieved in minutes on a single modern 32-processor compute node (e.g., Intel Xeon E5-2698_v3 "Haswell" node). The modeling code was benchmarked for accuracy against free-space and half-space analytic solutions.

The full-waveform inversion code base, which includes the forward modeling code, is written in Julia, a new, high-performance, just-in-time (JIT) compiled language specifically developed for parallel technical computing (<https://julialang.org/>) and with limited C language functions. Parallelization is achieved by using Julia's native parallel distribution capabilities for cluster computing. For the NLCG gradient construction, Julia's native parallel distribution is used to construct the gradient contributions from each source location on a separate cluster node and then to subsequently reduce (i.e., sum) these gradients. Because each NLCG iteration requires three forward modeling runs to compute the gradient and step length, it is imperative that the forward modeling code be computationally efficient.

6.3 Full-waveform single well seismic imaging of a vertical fracture with scalar and multi-component data

Single well seismic imaging has been explored sporadically since the late 1980's primarily by researchers at Schlumberger, Baker Hughes, and Lawrence Berkeley National Laboratory (Hornby, 1989; Majer et al., 1997; Chang et al., 1998; Yamamoto et al. 1999; Tang, 2004; Tang et al., 2007; Tang and Patterson, 2009; Haldorsen et al., 2005, 2006; Hirabayashi et al., 2010), and more recently by Shell/Schlumberger (Grae et al., 2012), Harbin Institute of Technology (Zhang and Hu, 2014) and the Chinese Academy of Sciences (Gong et al., 2015). The drivers for these efforts are to image features beyond the limited view of standard borehole logging tools. The earliest work utilized tools with a single pressure source and small arrays of pressure (hydrophone) receivers (< 10). Subsequent work has attempted to more accurately resolve fractures azimuthally by including azimuthal arrays of pressure receivers (up to 8 per azimuth) and by

utilizing oriented dipole sources and receivers. In our work, we have allowed for the possibility of fully general source and receiver types, such as those previously considered, as well as more complex sources that can be represented by general moment tensors. In the context of this prior body of work, the effort here can be viewed as an extension of Gong et al.'s (2015) approach for single well imaging, based on dipole sources and receivers and reverse time migration (i.e., imaging reflector locations), to fully general sources and receivers and elastic full-waveform inversion (i.e., imaging reflector locations and properties).

The following two subsections show the first set of single well elastic full-waveform inversions results produced by the recently developed code described in the previous section. At this point, only the first iterations of the full-waveform inversion have been performed to test the performance of the code and to gain insights to the characteristics of the new inversion scheme. For these preliminary tests, a simple model was used consisting of a single vertical fracture zone. The source/receiver borehole was not explicitly included in the model (i.e., its properties were taken to be the same as the host rock), although the capability exists in the modeling code for including it. The unfractured host rock has the following seismic properties:

P-wave velocity: $V_P = 5000$ m/s,
S-wave velocity: $V_S = 3030$ m/s,
P-wave elastic modulus: $c_{33} = 66.25 \times 10^9$ Pa,
S-wave elastic modulus: $c_{55} = 24.33 \times 10^9$ Pa,
Poisson's ratio: $\nu = 0.21$,
Density: $\rho = 2650$ kg/m³,
P-wave quality factor: $Q_P = 200$,
S-wave quality factor: $Q_S = 200$.

The fractured rock zone is a vertical slab 0.5 m in thickness located 10 m from the borehole with the following seismic properties representative of saturated, permeable, damaged rock:

P-wave velocity: $V_P = 1250$ m/s,
S-wave velocity: $V_S = 884$ m/s,
P-wave elastic modulus: $c_{33} = 4.141 \times 10^9$ Pa,
S-wave elastic modulus: $c_{55} = 2.071 \times 10^9$ Pa,
Poisson's ratio: $\nu = 0$,
Density: $\rho = 2650$ kg/m³,
P-wave quality factor: $Q_P = 100$,
S-wave quality factor: $Q_S = 100$.

A fixed set of 50 receivers spaced 0.2 m apart to form a 10 m long receiver array was located along a vertical line simulating the borehole. Seismic traces on 50 pressure hydrophones (case 1) and 50 3-component particle velocity geophones (case 2) were recorded for 3 ms at a sampling rate of 0.05 ms. A point pressure source with a Ricker wavelet source time function and a center frequency of 5000 Hz was fired at 3 locations along the vertical line simulating the borehole, each source location separated by 3 m. The two seismic data sets generated (case 1 and case 2) were used as the simulated field data for the elastic full-waveform inversion that is described in the following two subsections. The forward modeling simulations and full-waveform inversions were carried out on the National Energy Research Supercomputing Center's (NERSC) Intel Xeon E5-2698_v3 "Haswell" nodes.

6.3.1 Case 1: Fracture imaging with pressure source and pressure receivers

Elastic full-waveform imaging for the three pressure sources and the array of 50 pressure receivers after the first inversion iteration is shown in Figure 1. The receiver array is located between $z = -5$ m and $z = -15$ m, and the three sources at $z = -7$ m, -10 m and -13 m. The 3D image shows the P-wave elastic modulus (c_{33}) for the first NLCG iteration (similar to an RTM). For pressure sources and pressure receivers, the fracture

image should appear as a cylinder centered around the borehole (Note that in Fig. 1b, this cylinder has been truncated by the perfectly matched layer (PML) absorbing boundaries, which are 2 m thick slabs on each of the 6 faces of the 3D model). With additional NLCG iterations, the magnitude and focus of this image is expected to converge towards the true solution, but the general azimuthal artifacts present in this image will remain. This is because, as noted in prior studies on single well imaging (e.g., Chang et al. 1998), the pressure source and pressure receivers used in the full-waveform imaging lack azimuthal sensitivity, due to the omni-directional character of the scalar pressure wavefield. Additionally, after the first iteration of full-waveform inversion, significant near-source artifacts are present.

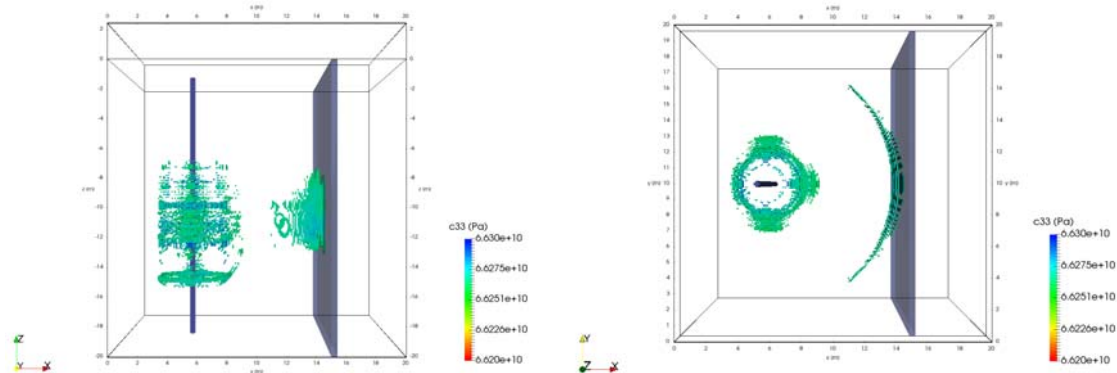


Figure 6-1. Case 1 - Single well elastic full-waveform fracture imaging with 3 pressure sources and 50 pressure receivers. Images of P-wave elastic modulus c_{33} in the x-z plane (a), and x-y plane (b) show reduction in the modulus from the background. Because pressure receivers have omni-directional sensitivity, the imaged fracture appears as a vertical cylinder with a radius equal to the well-fracture plane spacing that has been truncated by the absorbing boundaries of the numerical model. Near-source imaging artifacts are also clearly present.

6.3.2 Case 2: Fracture imaging with pressure source and particle velocity receivers

Case 2 is similar to Case 1, except that 3-component particle velocity receivers (geophones) are used in the full-waveform inversion instead of pressure receivers. The image of the P-wave elastic modulus shown in Fig. 2 has improved azimuthal focusing on the fracture than in Case 1. Additionally, less imaging artifacts are present, and the decrease in the elastic modulus after the first NLCG iteration is larger than for Case 1. This result shows the potential of elastic full-waveform inversion with a scalar source and directional receivers for imaging a fracture from a single borehole. It is anticipated that including directional sources should further improve the focusing of the fracture image.

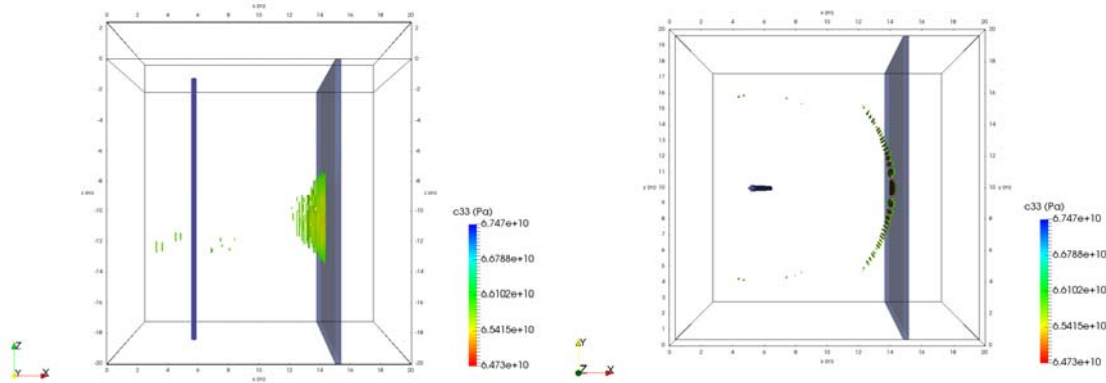


Figure 6-2. Case 2 - Single well elastic full-waveform fracture imaging with 3 pressure sources and 50 particle velocity receivers. Image of P-wave elastic modulus c_{33} in: (a) x-z plane, and (b) x-y plane. Directional particle velocity receivers provide azimuthal better focusing of fracture image and less imaging artifacts than pressure receivers.

6.4 Conclusions and Next Steps

This progress report has described an approach for imaging discrete fractures and fault zones from a single borehole using elastic full-waveform inversion and directional receivers. As described in Sec. 6.2.1, generality has been included in the implementation of the sources and receivers in the full-waveform code. This generality should allow the potential of elastic full-waveform inversion to be fully explored in the context of locating and characterizing fractures and fault zones in the rock mass surrounding a deep borehole from a single borehole. The next steps for this work are to perform a more systematic study of single well fracture imaging that includes realistic geological complexity, dipping fracture/fault zones and the borehole.

6.5 References

- Coates, R.T. and M. Schoenberg (1995). Finite-difference modeling of faults and fractures, *Geophys.*, 60:1514-1526.
- Chang, C., M. Kane, R. Coates, D. Hoyle, S. Watanabe, K. Dodds, C. Esmersoy & J. Foreman (1998). Localized maps of the subsurface, *Schlumberger Oilfield Review*, 10:56-66.
- Gong, H., H. Chen, X. He & X. Wang (2015). Eliminating the azimuth ambiguity in single-well imaging using 3C sonic data, *Geophys.*, 80:A13-A17.
- Grae, A.D., G.A. Ugueto, J.A. Roberts, H. Yamamoto, T. Oliver & G. Martinez (2012). Borehole acoustic reflection survey (BARS) from modern, dipole acoustic logs for high-resolution seismic-based fracture illumination and imaging, *SPWLA 53rd Annual Logging Symp.*
- Haldorsen, J.B.U., W. Borland, H.A.B. Al Rougha, A. Sultan & R. Meehan (2005). Azimuthal sonic imaging, *SEG Tech. Prog. Expand. Abstr.*, I017.
- Haldorsen, J., A. Voskamp, R. Thorsen, B. Vissapragada, S. Williams & M. Fejerskov (2006). Borehole acoustic reflection survey for high resolution imaging, *SEG Tech. Prog. Expand. Abstr.*, 314-318.
- Hirabayashi, N., K. Torii, H. Yamamoto, J.B.U. Haldorsen & A. Voskamp (2010). Fracture detection using borehole acoustic reflection survey data, *SEG Tech. Prog. Expand. Abstr.*, 523-527.
- Hornby, B. E. (1989). Imaging of near-borehole structure using full-waveform sonic data, *Geophys.*, 54: 747-757.

- Kuhlman, K.L., B.W. Arnold, P.V. Brady, D.C. Sassani, G.A. Freeze & E.L. Hardin (2015). Site characterization for a deep borehole field test, IHLRWM, Charleston, 624-631.
- Majer, E.L., J.E. Peterson, T.M. Daley, B. Kaelin, L. Myer, J. Queen, P. D'Onfro & W. Rizer (1997). Fracture detection using crosswell and singlewell surveys, *Geophys.*, 62:495-504.
- Schoenberg, M. and C.M. Sayers (1995). Seismic anisotropy of fractured rock, *Geophys.*, 60:204-211.
- Tang, X. M. (2004). Imaging near-borehole structure using directional acoustic-wave measurement, *Geophys.*, 69:1378–1386.
- Tang, X. M., Y. Zheng and D. Patterson (2007). Processing array acoustic logging data to image near-borehole geologic structures, *Geophys.*, 72:E87–E97.
- Tang, X. M. and D. Patterson (2009). Single-well S-wave imaging using multicomponent dipole acoustic-log data, *Geophys.*, 74:WCA211–WCA223.
- Tarantola, A. (1984). Inversion of seismic reflection data in the acoustic approximation, *Geophys.*, 49:1259–1266.
- Virieux, J. and S. Operto (2009). An overview of full-waveform inversion in exploration geophysics, *Geophys.*, 74:WCC127-WCC152.
- Yamamoto, H., J.B.U. Haldorsen, H. Mikada and S. Watanabe (1999). Fracture imaging from sonic reflection and mode conversion, SEG Tech. Prog. Expand. Abstr., 148-151.
- Zhang, Y. D. and H. S. Hu (2014). A technique to eliminate the azimuth ambiguity in single-well imaging, *Geophys.*, 79:D409–D416.